Julius-Maximilians-Universität
Würzburg
Graduate School of Science and Technology
Sektion Molecular & Material Science

Dissertation zur Erlangung des Doktorgrads
Doctor rerum naturalium (Dr. rer. nat.)
der Graduate School of Science and Technology, Julius-Maximilians-Universität Würzburg

Photodynamics of a fluorescent tetrazolium salt and shaping of femtosecond Laguerre-Gaussian laser modes in time and space

Photodynamik eines fluoreszierenden Tetrazoliumsalzes und Formung von Femtosekunden Laguerre-Gauss Lasermoden in Raum und Zeit

vorgelegt von
Tom Bolze
aus
Wismar

Würzburg, 2017

Eingereicht am: .....

Stempel Graduate School

Mitglieder des Promotionskomitees

Vorsitz: Prof. Dr. Volker Engel

1. Gutachter und Prüfer: Prof. Dr. Patrick Nürnberger (Ruhr-Universität Bochum)

2. Gutachter und Prüfer: Prof. Dr. Tobias Brixner

3. Prüfer: Prof. Dr. Tobias Hertel

Tag des Promotionskolloquiums: 09.03.2018

"A goal without a plan is just a wish"
- Antoine de Saint Exupéry

Zusammenfassung

Die vorliegende Arbeit wird eine Übersicht über die durchgeführten Studien, die die Fluoreszenzdynamiken von Phenyl-Beno-[c]-Tetrazolo-Cinnolinum Chlorid (PTC) in alkoholischen Lösungsmitteln verschiedener Viskosität mit Hilfe von zeitaufgelöster Fluoreszenzspektroskopie untersuchen, liefern. Des weiteren werden die Eigenschaften von Laserpulsen mit Laguerre-Gauss (LG) strahlprofilen in Hinblick auf ihre räumlichen und zeitlichen Charakteristika beleuchtet und ein Ansatz entwickelt, die räumliche Intensitätsverteilung zu messen und auf der Zeitskala der Pulse zu kontrollieren.
Tetrazoliumsalze sind aufgrund ihrer niedrigen Oxidations- und Reduktionspotentiale und ihrere spektroskopischen Eigenschaften weit verbreitet in biologischen Assays. Allerdings wird in diesen Anwendungen der Vorteil, den Messungen der Lichtesmission gegenüber der Lichtabsorption haben, vernachlässigt. Um das zu ergründen wurde PTC, als eines der wenigen bekannten Tetrazoliumsalze welches fluoresziert, im Hinblick auf seine lichtemittierenden Eigenschaften untersucht. Statische Spektroskopie wies nach, wie PTC aus einer Photoreaktion aus 2,3,5-Triphenyl-Tetrazoliumchlorid (TTC) erzeugt werden konnte und wie sich die Fluoreszenzquantenausbeute in alkoholischen Lösungsmitteln mit unterschiedlicher Viskosität verhält. In den geichen Lösungsmitteln wurden zeitkorreliertes Einzelphotonen Zählen (TCSPC) durchgeführt und der Fluoreszenzzerfall untersucht. Die globale Analyse der Ergebnisse hat gezeigt, das die Dynamiken sich in den verschiedenen Lösungsmitteln unterscheiden, die Konstante, welche die Hauptemission beschreibt, sich in den unterschiedlichen Lösungsmitteln zwar verändert, aber wenn die Fluoreszenzquantenausbeute auch berücksichtigt wird, zu Raten der Lichtemission führte, die unabhängig vom Lösungsmittel sind. Die nichststrahlende Rate allerdings hängt stark vom Lösungsmittel ab und ist auch verantwortlich für die unterschiedlichen Dynamiken in den verschiedenen Lösungen. Weitere Studien, die mit der höheren zeitlichen Auflösung der Fluoreszenzaufkonversionsmethode durchgeführt wurden, ergaben, dass die Hauptfluoreszenz unabhängig von der Anregungsenergie ist, aber die Relaxationsprozesse, welche vor der Lichtaussendung stattfinden, mit höherer Anregungsenergie länger dauern. Die Ergebnisse mündeten in ein denkbares Photoreaktionsschema, das durch einen strahlenden Zustand gekennzeichnet ist und einen konkurrierenden nichtstrahlenden Zerfallspfad besitzt, welcher einen kurzlebigen Zwischenzustand besitzen könnte.
Laguerre-Gauss Laserstrahlen und ihre Eigensachften haben in den letzten zwei Jahrzehnten viel wissenschaftliche Aufmerksamkeit erhalten. Auch im Hinblick auf neue Methoden, die die technologische Machbarkeitsgrenze verschieben, um neue Phänomene zu erforschen, ist es notwendig, das Verständnis über diese Strahlklasse zu erweitern und die Konsistenz der Resultate mit dem theoretischen Wissen abzugleichen und in Einklang zu bringen. Die Konversion einer Hermite-Gauss (HG) Mode in eine LG Mode, mit Hilfe einer spiralen Phasenplatte (SPP), wurde im Hinblick auf ihre räumlich-zeitlichen Charakteristika untersucht. Es wurde herausgefunden, dass Femtosekunden HG und LG Pulse einer bestimmten zeitlichen Dauer das gleiche Spektrum besitzen und durch die gleichen etablierten Methoden charakterisiert werden können. Es stellte sich heraus, dass die Modenkonversion nur die gewünschte LG Mode mit ihrem charakeristischen orbitalen Drehimpuls (OAM), der bei Frequenzverdopplung erhalten bleibt, erzeugt. Außerdem wurde demonstriert, dass ein zeitlich geformter Femtosekunden HG Puls nicht das Resultat der Modenkonversion beeinflusst, da zeitlich völlig verschieden strukturierte Pulse die gleiche LG Mode erzeugen. Des weiteren wurde die Summenfrequenz von fs LG Strahlen und die

Dynamik der Interferenz eines HG und eines LG Pulses beleuchtet. Es wurde gefunden, dass wenn beide entgegengesetzt gechirpt sind, die räumliche Intensitätsverteilung auf der Zeitskala der Pulse um die Strahlachse rotiert. Theoretisch wurde ein Vorgehen entwickelt, das eine Messung dieser Dynamik, durch die Aufkonversion der Interferenz mit einem dritten Gate-Puls, ermöglicht. Die Ergebnisse dieser Methode wurden auf theoretischer Ebende diskutiert und ein Versuch einer experimentellen Realisierung wurde unternommen. Allerdings konnten die gemessenen Resultate, aufgrund experimenteller Limitierungen insbesondere der interferometrischen Stabilität, die theoretischen Erwartungen nur bedingt demonstrieren.

Abstract

This thesis will outline studies performed on the fluorescence dynamics of phenyl-benzo-[c]-tetrazolo-cinnolium chloride (PTC) in alcoholic solutions with varying viscosity using time-resolved fluoro-spectroscopic methods. Furthermore, the properties of femtosecond Laguerre-Gaussian (LG) laser pulses will be investigated with respect to their temporal and spatial features and an approach will be developed to measure and control the spatial intensity distribution on the time scale of the pulse.
Tetrazolium salts are widely used in biological assays for their low oxidation and reduction thresholds and spectroscopic properties. However, a neglected feature in these applications is the advantage that detection of emitted light has over the determination of the absorbance. To corroborate this, PTC as one of the few known fluorescent tetrazolium salts was investigated with regard to its luminescent features. Steady-state spectroscopy revealed how PTC can be formed by a photoreaction from 2,3,5-triphenyl-tetrazolium chloride (TTC) and how the fluorescence quantum yield behaved in alcoholic solvents with different viscosity. In the same array of solvents time correlated single photon counting (TCSPC) measurements were performed and the fluorescence decay was investigated. Global analysis of the results revealed different dynamics in the different solvents, but although the main emission constant did change with the solvent, taking the fluorescence quantum yield into consideration resulted in an independence of the radiative rate from the solvent. The non-radiative rate, however, was highly solvent dependent and responsible for the observed solvent-related changes in the fluorescence dynamics. Further studies with the increased time resolution of femtosecond fluorescence upconversion revealed an independence of the main emission constant from the excitation energy, however the dynamics of the cooling processes prior to emission were prolonged for higher excitation energy. This led to a conceivable photoreaction scheme with one emissive state with a competing non-radiative relaxation channel, that may involve an intermediate state.
LG laser beams and their properties have seen a lot of scientific attention over the past two decades. Also in the context of new techniques pushing the limit of technology further to explore new phenomena, it is essential to understand the features of this beam class and check the consistency of the findings with theoretical knowledge. The mode conversion of a Hermite-Gaussian (HG) mode into a LG mode with the help of a spiral phase plate (SPP) was investigated with respect to its space-time characteristics. It was found that femtosecond LG and HG pulses of a given temporal duration share the same spectrum and can be characterized using the same well-established methods. The mode conversion proved to only produce the desired LG mode with its characteristic orbital angular momentum (OAM), that is conserved after frequency doubling the pulse. Furthermore, it was demonstrated that temporal shaping of the HG pulse does not alter the result of its mode-conversion, as three completely different temporal pulse shapes produced the same LG mode. Further attention was given to the sum frequency generation of fs LG beams and dynamics of the interference of a HG and a LG pulse. It was found that if both are chirped with inverse signs the spatial intensity distribution does rotate around the beam axis on the time scale of the pulse. A strategy was found that would enable a measurement of these dynamics by upconversion of the interference with a third gate pulse. The results of which are discussed theoretically and an approach of an experimental realization had been made. The simulated findings had only been reproduced to a limited extend due to experimental limitations, especially the interferometric stability of the setup.

T. Bolze: Photodynamics of a fluorescent tetrazolium salt and shaping of femtosecond Laguerre-Gaussian laser modes in time and space, 2017

LIST OF PUBLICATIONS

Reference [1]:

T. Bolze, J.-L. Wree, F. Kanal, D. Schleier, and P. Nuernberger,
Ultrafast Dynamics of a Fluorescent Tetrazolium Compound in Solution,
ChemPhysChem, **19**, 138–147, 2018

The following manuscript is in preparation:

T. Bolze and P. Nuernberger,
Temporally shaped Laguerre-Gaussian femtosecond laser beams,
Appl. Opt., accepted for publication, 2018

Further publications not related to this thesis:

C. Lux, M. Wollenhaupt, T. Bolze, Dr. Q. Liang, J. Köhler, C. Sarpe, and T. Baumert,
Circular Dichroism in the Photoelectron Angular Distributions of Camphor and Fenchone from Multiphoton Ionization with Femtosecond Laser Pulses,
Angew. Chem. Int. Ed., **51**, 5001–5005, 2012

C. Lux, M. Wollenhaupt, T. Bolze, Dr. Q. Liang, J. Köhler, C. Sarpe, and T. Baumert,
Zirkulardichroismus in den Photoelektronen-Winkelverteilungen von Campher und Fenchon aus der Multiphotonenionisation mit Femtosekunden-Laserpulsen,
Angew. Chem., **124**, 5086–5090, 2012

The publication above has partly been used in this thesis. The following table itemizes to what extent the different sections of the article have been reused at which position in the present work. The permission of reproducing this material was given by the publishing company holding the copyright, the corresponding document is attached at the end of this work. Additionally, the sources of adapted figures are indicated at the end of the corresponding figure captions.

publication	usage	dissertation
Ref. [1]		
pp. 1–2	text reproduced and modified	pp. 33–34
pp. 2–3	text reproduced and figures adapted	pp. 51–53
pp. 3–4	text reproduced and figure adapted	pp. 53–54
pp. 4–5	figure adapted and text reproduced	pp. 55–59
p. 4	table adapted	p. 63
pp. 5–6	figure adapted and text reproduced	pp. 59–61
pp. 7–9	text modified and adapted, figures reproduced	62–66

Ref. [1] – Reproduced in part with permission from ChemPhysChem, **19**, 138–147, 2018.© (2017) Wiley-VCH Verlag GmbH & Co. KGaA

CONTENTS

List of Publications **VII**

1 Introduction **1**

2 Theoretical concepts **5**
2.1 Mathematical description of femtosecond laser pulses 5
2.1.1 Temporal and spectral shape of $E(t, \omega)$ 6
2.1.2 The influence of dispersion and spectral phase on the temporal shape 9
2.1.3 Concept of a $4f$-pulseshaper 13
2.1.4 Spatial properties of electromagnetic waves 15
2.1.5 Nonlinear optical processes 21
2.2 Molecules and light 23
2.2.1 Electronic structure of molecules 23
2.2.2 Transitions in molecules 25
2.3 Time-resolved fluorescence spectroscopy techniques 27
2.3.1 Time correlated single photon counting 29
2.3.2 Fluorescence upconversion 30

3 Experimental Techniques **33**
3.1 Instrumentation for the fluorescence studies 33
3.1.1 Sample preparation 33
3.1.2 Fluorescence quantum yield determination 35
3.1.3 TCSPC device 37
3.1.4 Femtosecond fluorescence upconversion 38
3.2 Pulse-shaping setup 40
3.2.1 The laser system 40
3.2.2 LG-mode conversion 43
3.2.3 The $4f$-pulseshaper 45
3.2.4 The combined setup 47

4 Fluorescence studies of PTC **51**
4.1 Static absorption and fluorescence spectra 51

4.2 Quantum yield measurements 53
4.3 Time resolved fluorescence measurements 55
4.3.1 picosecond-dynamics 55
4.3.2 femtosecond-dynamics 59
4.4 Interpretation and discussion of the results 62

5 Pulseshaping of fs-Laguerre-Gaussian laser modes 67
5.1 Setup characterization 67
5.1.1 Pulse characterization of the LG and HG Arm 68
5.1.2 Time integrated LG-HG interference in 1st and 2nd order 70
5.1.3 Spatially-resolved crosscorrelation of the shaped and unshaped pulses 74
5.2 Temporally shaped LG pulses 75
5.3 Time evolution of the spatially resolved LG-HG interference 80
5.3.1 Simulation 82
5.3.2 Measurement 85

6 Summary and Outlook 89

List of Abbreviations VII

Biblography XIX

Permissions XXI

Acknowledgements XXIII

CHAPTER 1

INTRODUCTION

Light is as omnipresent in our daily lives as it is essential for it. The perception of light as an electromagnetic wave by James Clerk Maxwell in 1865 was as groundbreaking as it was ingenious at the time and is now considered as one of the greatest intellectual achievements mankind has ever made. Ever since then the study of the light-matter interactions has seen a tremendous scientific attention with the goal to unravel the mysteries of life and the universe.

Among the many quests surrounding electromagnetic radiation is its control and manipulation. The prediction of the laser by Einstein and its first experimental realization in the 1960s gave rise to an array of new techniques and methods for studying light-matter interactions. For the first time in history a monochromatic light source, that is highly collimated and intense, was available, although in its first implementations the laser was described as a solution searching for a problem. An assessment that turned out to be more than false from today's point of view. For a review of the laser development see ref. [2]. Soon after the first demonstration of the laser, effort had been made towards sub-nanosecond pulsed lasers, that eventually lead to pulses on the time scale of a couple femtoseconds (10^{-15} s). These electromagnetic events are among the shortest man-made and controllable events and have found their way into several high-tech applications and a lot of scientific methods. For example, they offer a great tool to understand the dynamics of chemical reactions, since those typically take place on time scales down to femtoseconds. The term *femtochemistry* describes a junction of chemistry and laser pulses on this time scale. In 1999 the Nobel Prize in Chemistry was awarded to one of the founders of this research field, Ahmed Zewail. Topics in this field range from observing to controlling chemical reactions in real time. The latter was termed *quantum control* and has given rise to several several schemes that allow the control of quantum mechanical systems [3–7].

The observation of chemical reactions on the other hand has also spawned its own unique methods and techniques involving femtosecond laser pulses. Most notably the pump-probe scheme [8, 9] is wide-spread and has found its way into many scientific applications. The advantage of knowing the exact point in time at which a photo-induced chemical reaction starts allows for a sampling of the detection with another pulse and thus monitoring the dynamics of the reaction in time. Light induced chemical reactions, that have been stud-

T. Bolze: Photodynamics of a fluorescent tetrazolium salt and shaping of femtosecond Laguerre-Gaussian laser modes in time and space, 2017

ied extensively by pump-probe schemes are dissociation, isomerization, and intersystem crossing [7, 10–13], however also intramolecular relaxation processes can be investigated by these methods. Such dynamics take place after a molecule absorbs energy of some kind and tries to equilibrate the energy within itself or its surroundings. Uptake of energy can lead to several types of dynamics, for example translation, rotation, and vibration. Also electronic excitation is possible, where an electron resting in the ground state of a molecule changes its potential energy surface, which is followed by another sequence of possible dynamics. Among those processes is the ability of certain molecules to emit light, which is called luminescence that can be differentiated into fluorescence and phosphorescence. The latter involves a spin flip in the system and is therefore classically spin forbidden, although spin-orbit coupling especially in larger molecules and atoms might loosen this rule. Fluorescence does not involve a spin flip and is therefore more common and easier to observe. The dynamics of the light emission of a molecule are strongly related to its quantum chemical structure, thus may offer insight into the latter. Fluorescence is also a way of relaxation for a molecule trying to reach its ground state, as such it is usually accompanied by other intra- and intermolecular relaxation processes. Especially in the liquid phase, where molecules are constantly interacting with the solvent, rich dynamics appear in the molecule and the solvent trying to equilibrate the energy that is deposited in the system for example though light absorption [14, 15].

The compound class of tetrazolium salts was first described in 1894 by Pechmann and Runge [16]. These molecules are characterized by a low reduction threshold, which makes them an ideal sensor for monitoring the reductive and oxidative features of their surroundings. Since metabolic reactions in the cellular environment often involve changing the local chemical potential, tetrazolium salts have found their way into many applications surrounding the metabolism of cells. Most notably are techniques in the fields of agriculture [17, 18], cell biology [19, 20], cancer [21, 22] and other medical research [23, 24], organic chemistry [25, 26], ionic liquids as cations [27, 28], and dosimetry for quantification of ultraviolet light [29, 30]. One rather unexplored feature of tetrazolium salts is their emission capability, although it is known that fluorescing specimen exist [31]. One goal of this thesis is to elaborate further into the dynamics of this compound by means of time resolved fluorescence spectroscopy.

Using fluorescent tetrazolium salts in cell biology would for example give access to the methods of fluorescence microscopy, which is a major tool to understand processes in living cells. Among the most cutting edge fluorescence microscopy methods is stimulated emission depletion (STED)[32], which was awarded with the Nobel Prize in Chemistry to Stefan Hell in 2014. In 2017 the newest iteration of this technique was reported [33], that is able to determine the coordinates of a molecule with minmal emission fluxes and is termed MINFLUX. The resolution of the STED method was already groundbreaking, as it surpassed the Abbe diffraction limit, however MINFLUX has a reported resolution of $\approx 1\,\mathrm{nm}$. The concept of both techniques relies on a pump-dump scheme, in which one laser excites the fluorescent molecules in the sample. A second laser then dumps the excitation by stimulated emission. The dump-beam has a doughnut-like shape, whereas the pump-beam is Gaussian in shape. This results in a detectable fluorescence of the sample that only originates from the dark spot in the center of the Laguerre-Gaussian (LG) beam, as doughnut-shaped beams are called.

These LG beams have a unique feature, since they have a helical spatial phase and are

therefore carrying an orbital angular momentum (OAM). They have first been described in 1992 by Padgett and Allen [34] and a lot of progress has been made in the last two decades regarding the understanding of their properties and prospective applications. Commercial optical communication systems use photons for information transfer. To encode as much information as possible into as few photons as possible frequency multiplexing is the common technique in optical communication. OAM multiplexing, that can be understood as a special kind of space-multiplexing, has been demonstrated in free space [35, 36] and fibers [37] to increase the information density much further. Also quantum cryptography using entangled pairs of OAM carrying photons is discussed in literature [38–40]. The laser systems used in these experiments are either continuous wave or narrow bandwidth infrared light sources. Although femtosecond pulses with LG beamprofiles have been demonstrated, not all methods of controlling and measuring fs pulses have been applied to LG beams yet. To close the gap this work will focus on some of them, namely fs temporal pulse-shaping, frequency conversion, and temporal characterization.
This work is ordered as follows: chapter 2 will give an insight into the theoretical concepts of femtosecond laser pulses, a quantum mechanical description of molecules and their transitions, and time-resolved fluorescence spectroscopy techniques used in this work. Chapter 3 gives a detailed overview of the instruments and methods used for the experiments. Chapter 4 will give an overview of the studies performed on the fluorescence dynamics of PTC in alcoholic solutions. First, steady-state absorption and emission spectroscopy will be employed to get information on the general electronic structure of the molecule and its fluorescence quantum yield in several alcoholic solvents. Time-resolved experiments with varying excitation wavelengths using time correlated single photon counting (TCSPC) and fs-fluorescence upconversion will be shown, that consistently demonstrate that one dominant process is responsible for the majority of the PTC fluorescence. Dynamics that depend on the alcoholic solvent used will be shown and discussed, in order to gain a deeper understanding of the intramolecular processes. Moreover solvent related relaxation dynamics will be disclosed with respect to the ultrafast part of the fluorescence. The accumulated observations will then be discussed and joined into a photoreaction scheme of PTC.
In chapter 5 the results of the experiments involving fs-LG pulses will be presented. After a detailed characterization of the mode conversion and related parts of the beam path it will be demonstrated that LG pulses can be generated from temporally shaped fs pulses and characterized by the same means as Hermite-Gaussian (HG) pulses. The last part of this chapter will deal with the temporal evolution of the LG-HG interference of two fs pulses. Its behavior in time will be calculated using space-time dependent fields and a method will be explored that involves frequency conversion to visualize and measure this time evolution. An experimental approach will be done to measure the predictions and discuss them in the context of the simulations.
The work will be summarized in chapter 6, a discussion will be given, and future experiments that could extend the findings of this work will be outlined.

CHAPTER 2

THEORETICAL CONCEPTS

This chapter will provide an overview of the theoretical concepts of the experiments presented in this thesis, which is divided in two parts. The first focuses on the investigation of fluorescence dynamics of molecules in different solvents. Since these processes occur on ultrashort time scales, techniques must be used that have access to these types of short-time events. This feat is accomplished by the use of laser pulses, which are shorter than the dynamics that are investigated. These light pulses are also highly controllable in terms of wavelength and timing, which makes them the ideal tool to start photoinduced dynamics and to monitor them as well. The second part will deal with manipulating the field of such a laser pulse in terms of its exact temporal and spatial shape. Therefore, a deep understanding of laser pulses as a prerequisite to all presented experiments is needed, which is given in section 2.1 of this chapter. It is followed by a section dealing with the quantum mechanical description of molecular systems in 2.2. In the end two time resolved spectroscopy techniques, that are used for the experiments in this thesis, will be presented in section 2.3.

2.1 Mathematical description of femtosecond laser pulses

In 1861 James Clerk Maxwell published his work on electromagnetism[41], wherein formulas that describe the interactions of electric $\vec{E}$ and magnetic $\vec{B}$ fields can be found. Based on that he published his "Electromagnetic Theory of Light" four years later [42]. Light as an electromagnetic wave can be can be described by the Maxwell equations in their Heavyside form:[43]

$$\vec{\nabla} \cdot \vec{E} = \frac{\rho}{\epsilon_0} \tag{2.1.1}$$

$$\vec{\nabla} \cdot \vec{B} = 0 \tag{2.1.2}$$

$$\vec{\nabla} \times \vec{E} = -\frac{\partial \vec{B}}{\partial t} \tag{2.1.3}$$

$$\vec{\nabla} \times \vec{B} = \mu_0 \vec{J} + \mu_0 \epsilon_0 \cdot \frac{\partial \vec{E}}{\partial t} \tag{2.1.4}$$

with the charge density ρ, the permittivity of free space ϵ_0, the permeability of free space μ_0 and the current density $\vec{J}$. These equations describe light as well, due to their electromagnetic nature, as Maxwell later deduced. Since light or electromagnetic radiation is omnipresent, its nature and interaction with matter is of great importance to understand phenomena and processes in our world. The invention of the laser (***l**ight **a**mplification by **s**timulated **e**mission of **r**adiation*) in the early 60s as a tool for these investigations was groundbreaking. For the first time in history an intense light source with coherent and highly collimated emission was available. Nowadays, lasers are widely used in almost every major industrial branch. On top of continuous emission also pulsed lasers have been constructed and have established themselves as a powerful tool for spectroscopic investigations of atomic and molecular systems.
This section will deal with the mathematical formulation of light pulses. First, a general description of the temporal and spectral structure of a pulse and its interconnection will be given in section 2.1.1. Then the effect of natural dispersion on the spectral phase and thus the temporal shape of the pulse will be discussed in section 2.1.2. Thereafter a concept of arbitrary alteration of the spectral phase will be introduced in section 2.1.3 with the principles of a $4f$-Pulseshaper. Section 2.1.4 will deal with the spatial properties of plane and non-planar waves. Discussion of nonlinear optical processes relevant to this work will top this section of in 2.1.5.

2.1.1 Temporal and spectral shape of $E(t, \omega)$

Inserting $\vec{\nabla} \times \vec{B}$ from equation 2.1.4 in the curl of $\vec{\nabla} \times \vec{E}$ in equation 2.1.3 and using the vector identity $\nabla \times \nabla \times E = \nabla(\nabla \cdot E) - \nabla^2 E$ leads to the wave equation in free space:

$$\nabla^2 E = \mu_0 \epsilon_0 \frac{\partial^2 E}{\partial t^2}. \tag{2.1.5}$$

Assuming a plane wave, equation 2.1.5 simplifies to the plane wave equation

$$\frac{\partial^2 E}{\partial z^2} = \mu_0 \epsilon_0 \frac{\partial^2 E}{\partial t^2} \tag{2.1.6}$$

where z is the direction of propagation. The sinusoidal solution to equation 2.1.6 for laser pulses takes the form:

$$E(z, t) = A(t) \cdot cos(\omega_0 t + \phi_0 + \phi(t)) \tag{2.1.7}$$

where $A(t)$ denotes time-dependent amplitude, ω_0 the central angular frequency, ϕ_0 the constant phase and $\phi(t)$ the time-dependent phase. Both phases have no impact on the envelope of the pulse, since its amplitude part is separated from the oscillating part, however, especially the time-dependent phase may change the frequency of the oscillation over the duration (e.g. the course) of the pulse. Therefore, the instantaneous frequency $\omega(t)$ is defined as

$$\omega(t) = \frac{d}{dt} \cdot (\omega_0 t + \phi_0 + \phi(t)) = \omega_0 + \frac{d\phi(t)}{dt}. \tag{2.1.8}$$

An equivalent form of equation 2.1.7 can also be written as

$$E(z,t) = \mathrm{Re}\left[A(t)e^{i\omega_0 t}e^{i\phi_0}e^{i\phi(t)}\right] \tag{2.1.9}$$

where Re denotes the real part. Here the separation of amplitude, oscillatory part and phase becomes apparent as well.
Since the superposition principle holds, a laser pulse that is fixed in space can be represented by a series of monochromatic waves that are fixed in space as well. This so-called Fourier decomposition is described by the Fourier transform

$$E(t) = \frac{1}{2\pi}\int_{-\infty}^{\infty} E(\omega)e^{i\omega t}d\omega \tag{2.1.10}$$

and the inverse Fourier transform

$$\tilde{E}(\omega) = \int_{\infty}^{\infty} E(t)e^{-i\omega t}dt. \tag{2.1.11}$$

This interconnection of time space and frequency space is known from acoustics[44, 45]. In optics the same principles holds, a short event has to have a broad spectrum, whereas a narrow spectrum corresponds to a near constant signal in time. Laser pulses can actually become so short (sub 5 fs) that their spectrum spans the whole visible region of the electromagnetic spectrum.
Analogue to equation 2.1.9 the spectral electric field can be separated into an amplitude and phase part. In its nature as the Fourier transform of the real valued temporal electric field, which is not necessarily symmetric with respect to time, the spectral electric field in general is complex and takes the form

$$\tilde{E}(\omega) = \sqrt{I(\omega)}e^{-i\phi(\omega)}, \tag{2.1.12}$$

where $I(\omega)$ is the spectral intensity, which is proportional to the power spectral density that can be measured with a spectrometer, and $\phi(\omega)$ is the spectral phase. Analogue to the instantaneous frequency, which describes the instance at which a certain frequency is present in time, a measure of the time delay for a specific frequency component can be derived from $\phi(\omega)$. This parameter is called group delay

$$T_g(\omega) = \frac{d\phi(\omega)}{d\omega}. \tag{2.1.13}$$

For any spectral phase $\phi(\omega)$ independent of the frequency ω the spectral and temporal amplitudes satisfy the uncertainty relation

$$\Delta t \Delta\omega \geq K \tag{2.1.14}$$

where the constant K depends on the shape of the spectrum. For Gaussian spectra, which will be discussed exclusively in this thesis, the constant becomes $K = 0.441$. This

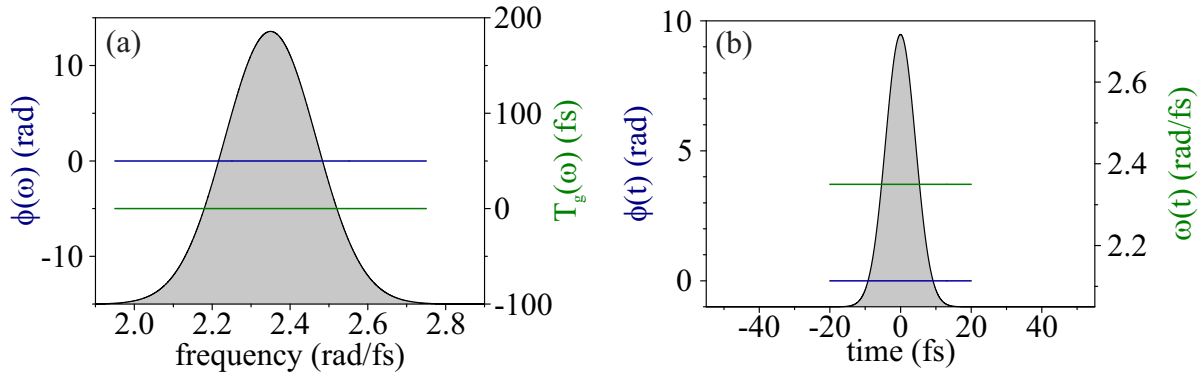

Figure 2.1.1: A bandwidth limited pulse with a central wavelength of 800 nm and a temporal FWHM of 10 fs. Spectral intensity $I(\omega)$, spectral phase $\phi(\omega)$ and group delay $T_g(\omega)$ are shown in (a). Temporal Intensity $I(t)$, temporal phase $\phi(t)$ and instantaneous frequency $\omega(t)$ are displayed in (b).

relation is known as the time-bandwidth product. A pulse that satisfies the equality is called bandwidth limited or Fourier-transform limited. An example of such a pulse is displayed in figure 2.1.1 for a central wavelength of 800 nm and a temporal full width at half maximum (FWHM) of 10 fs. The spectral intensity $I(\omega)$ along with the spectral phase $\phi(\omega)$ and the group delay $T_g(\omega)$ is illustrated in the left panel. Note that the spectral phase (and group delay) is zero over the whole spectral range of the pulse, which means that the pulse is bandwidth limited. In the right panel, the temporal intensity $I(t)$ is depicted along with the temporal phase $\phi(t)$ and the instantaneous frequency $\omega(t)$. The phase is again zero over the whole duration of the pulse and $\omega(t)$ is constant at $2.35\,\frac{\text{rad}}{\text{fs}}$, which is the central angular frequency. Any non-zero spectral phase can be expanded in a Taylor series for quantification. This series expands the phase into

$$\phi(\omega) = \sum_{n=0}^{\infty} \frac{\phi^n(\omega_0)}{n!} \cdot (\omega - \omega_0)^2$$

with

$$\phi^n(\omega_0) = \left.\frac{d^n\phi(\omega)}{d\omega^n}\right|_{\omega=\omega_0}.$$

Aborting the series after $n = 3$ yields:

$$\phi(\omega) = \phi(\omega_0) + \phi'(\omega_0)(\omega - \omega_0) + \frac{1}{2}\phi''(\omega_0)(\omega - \omega_0)^2 + \frac{1}{6}\phi'''(\omega_0)(\omega - \omega_0)^3. \qquad (2.1.15)$$

The effect of every polynomial of this series on the pulse shape will be discussed in the next subsection. Any nonlinear term applied to the spectral phase results in the inequality of equation 2.1.14 and thus broadens the pulse.

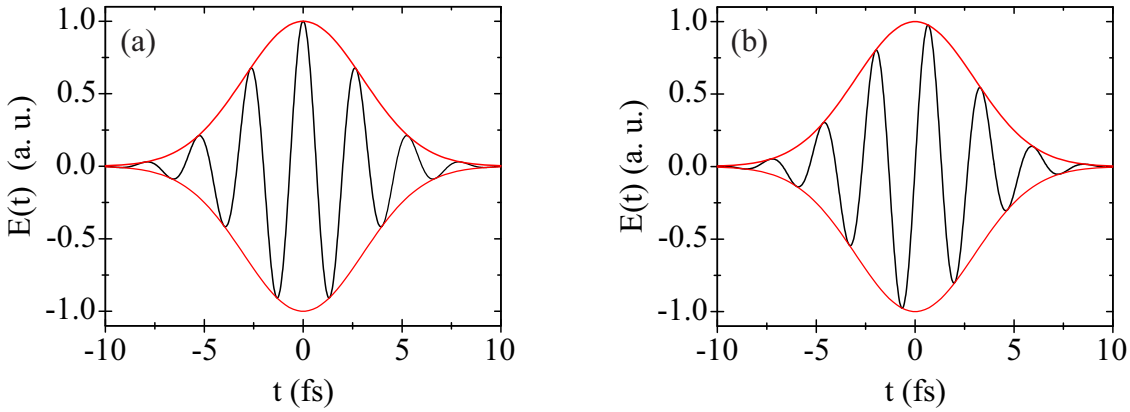

Figure 2.1.2: Temporal electric field (black) and envelope (red) of a pulse with a central wavelength of 800 nm and a temporal FWHM of 5 fs. If the spectral phase $\phi(\omega) = 0$ the maximum of the field and envelope coincide, leading to a cosine pulse (a). For a spectral phase of $\phi(\omega) = \frac{\pi}{2}$ the field is zero at the maximum of the envelope, leading to a sine pulse (b).

2.1.2 The influence of dispersion and spectral phase on the temporal shape

The simplest polynomial spectral phase is that of a constant, which is represented by the first term in equation 2.1.15. This term is often called b_0 and has no influence on the amplitude part of the temporal electric field but on the oscillatory part from equation 2.1.7. More precisely b_0 is the phase between the envelope and the oscillation, thus only becomes relevant for pulses that are consisting of only a few optical cycles[46, 47]. In figure 2.1.2 the oscillatory (red) and the amplitude (black) part of a pulse with a central wavelength of 800 nm and a FWHM of 5 fs are shown for a constant spectral phase of $\phi(\omega) = 0$ (left) and $\phi(\omega) = \frac{\pi}{2}$ (right). For a phase of zero, a maximum of the oscillation and the maximum of the envelope coincide at time $t = 0$ fs. This is called a cosine pulse. In case of $\phi(\omega) = \frac{\pi}{2}$ the oscillation is shifted a quarter of an optical cycle, which leaves the electric field at time zero $E(0) = 0$, thus generating a sine pulse. The implication of this is a slightly reduced maximum electric field strength, which can become relevant for highly nonlinear processes with few-cycle pulses[48, 49]. In the scope of this thesis, however, no such pulses are used.

The linear polynomial term of the spectral phase (referred to as b_1) does not change the oscillatory part of the electric field but the maximum of its envelope and thus shifting the pulse in time. Thereby, the pulse shape is not altered. In figure 2.1.3 the spectral (left) and temporal (right) intensities of an 800 nm pulse with a temporal FWHM of 10 fs and a linear spectral phase of $b_1 = 20$ fs are shown along with the respective phases $\phi(\omega)$ and $\phi(t)$, the group delay $T_g(\omega)$, and the instantaneous frequency $\omega(t)$. By applying a linear spectral phase, a constant group delay is introduced according to equation 2.1.13, which corresponds to a shift in the time domain. The temporal phase and instantaneous frequency, however, are not changed. The direction in which the pulse is temporally shifted is determined by the sign of b_1, the reference is the time zero of a pulse without a spectral phase.

The quadratic spectral phase term is referred to as 'linear chirp' and denoted as b_2. Ac-

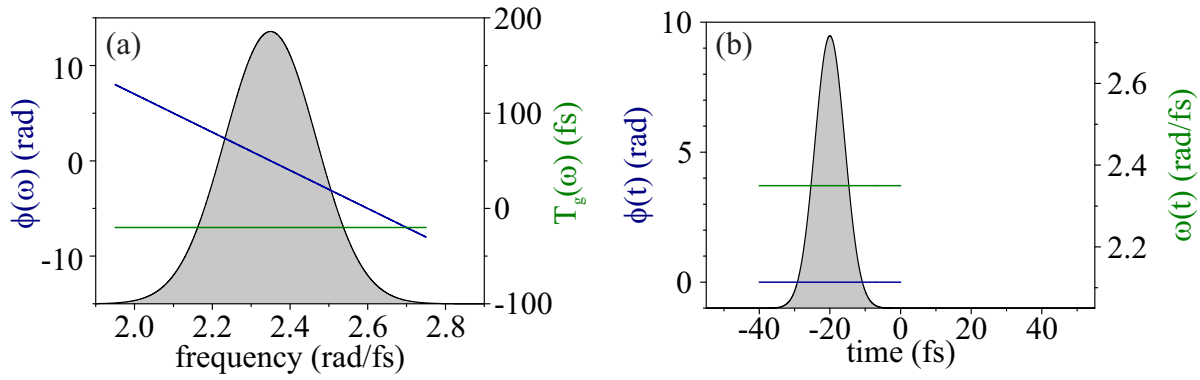

Figure 2.1.3: A pulse with a central wavelength of 800 nm, a temporal FWHM of 10 fs and a linear spectral phase term $b_1 = 20$ fs. Spectral intensity $I(\omega)$, spectral phase $\phi(\omega)$ and group delay $T_g(\omega)$ are shown in (a). Temporal Intensity $I(t)$, temporal phase $\phi(t)$ and instantaneous frequency $\omega(t)$ are displayed in (b).

cording to equations 2.1.8 and 2.1.13 it induces a linear change of the instantaneous frequency and the group delay, respectively. This entails that the different spectral components get ordered in time by increasing or decreasing frequency for positive or negative signs of b_2, respectively. A positive sign is referred to as an *up-chirp* and a negative as a *down-chirp*. In figure 2.1.4 the spectral (left) and temporal (right) intensities of a pulse with 800 nm central wavelength and a temporal FWHM of 10 fs with a quadratic spectral phase of $b_2 = 200\,\text{fs}^2$ is shown. The integral of the intensity over time, which is equivalent to the pulse energy, of the chirped pulse in figure 2.1.4 is the same as for the shifted pulse in figure 2.1.3. But due to the temporal broadening in case of a quadratic spectral phase the peak intensity decreases, thus any process dependent on the intensity (but not the energy) is sensitive to a chirp in the pulse. However, any pulse only becomes stretched out in time due to a quadratic spectral phase. If Gaussian spectra are considered, the pulse length Δt_{out} of an input pulse Δt_{in} after applying a quadratic spectral phase of ϕ'' can be estimated via[47, 50]

$$\Delta t_{out} = \sqrt{\Delta t_{in}^2 + \left(4ln2\frac{\phi''}{\Delta t_{in}}\right)^2}. \tag{2.1.16}$$

The cubic spectral phase term (also called **T**hird **O**rder **D**ispersion) gives rise to a quadratic group delay. This leads to a fragmentation of the pulse. The central frequency (around which the phase is applied) carries most of the spectral intensity and is almost not influenced by the phase, since a cubic function is in first approximation zero around ω_0. This results in a big sub-pulse around time zero, which is mostly composed of the central frequency components. However, around the carrier frequency all electromagnetic waves are dispersed in a way that two components with the same spectral separation from the central frequency, but in opposite directions, have the same delay. The instantaneous frequency remains constant, since the mean of all occurring waves at any time is equal to the central frequency. However, at any time two electromagnetic waves with different frequencies overlap and may interfere constructively or destructively. For some delay times this results in an annihilation and thus, a knot in the intensity profile and a formation of pulse fragments with different spectral composition. The temporal phase in this case

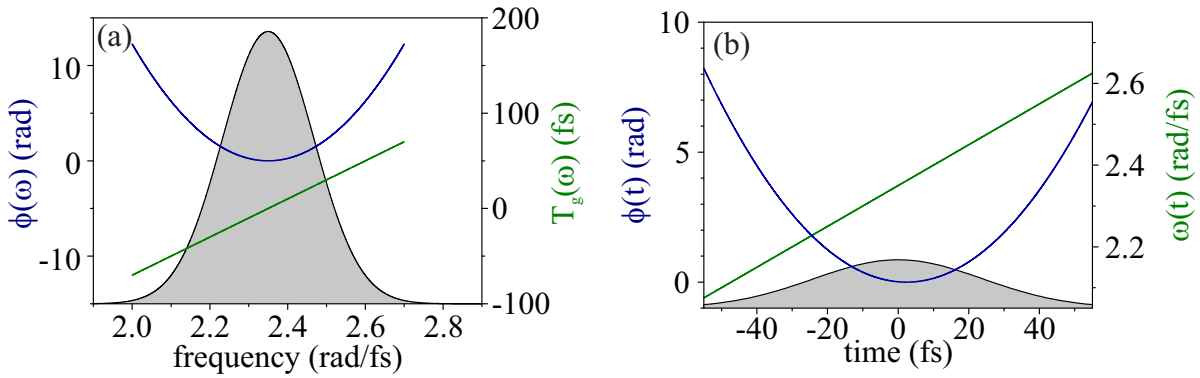

Figure 2.1.4: A pulse with a central wavelength of 800 nm, a temporal FWHM of 10 fs and a quadratic spectral phase term $b_2 = 200\,\mathrm{fs}^2$. Spectral intensity $I(\omega)$, spectral phase $\phi(\omega)$ and group delay $T_g(\omega)$ are shown in (a). Temporal Intensity $I(t)$, temporal phase $\phi(t)$ and instantaneous frequency $\omega(t)$ are displayed in (b).

jumps from 0 and π and back between the sub-pulses. This is illustrated in figure 2.1.5, where the spectral intensity, phase, and group delay is depicted on the left and the temporal intensity, phase, and instantaneous frequency is depicted on the right for a pulse with a central wavelength of 800 nm, a temporal FWHM of 10 fs and a cubic spectral phase of $b_3 = 1000\,\mathrm{fs}^3$. Phase components of third order also occur naturally in optical media, however, they are usually in the same order of magnitude than second order dispersion [47] and are therefore less relevant, due to their cubic dependence $(\omega - \omega_0)^3$. The natural dispersion may introduce complex amplitude and phase modulation in the time and frequency domain for ultrashort laser pulses. In general, the perturbation introduced via dispersion can be described by a temporal $M(t)$ and spectral $M(\omega)$ transfer function. Both functions represent a Fourier pair.

$$M(t) = \frac{1}{2\pi} \int_{-\infty}^{+\infty} M(\omega) e^{i\omega t} d\omega \qquad \Longleftrightarrow \qquad M(\omega) = \int_{-\infty}^{+\infty} M(t) e^{-i\omega t} dt$$

If a pulse propagates through an optical element the electric field $E_{in}(t)$ of the pulse gets convoluted with the transfer function $M(t)$ according to:

$$E_{out}(t) = E_{in}(t) \otimes M(t) = \int_{-\infty}^{+\infty} M(t - t') E_{in}^{+}(t') dt'$$

and results in the electric field $E_{out}(t)$ after passing through the element. The convolution theorem states that a convolution in one Fourier domain equals a multiplication of the Fourier pairs in the other domain. In the present case this leads to the much easier expression

$$E_{out}(\omega) = E_{in}(\omega) \cdot M(\omega), \tag{2.1.17}$$

where the incoming spectral electric field $E_{in}(\omega)$ gets multiplied with the spectral transfer function yielding the outgoing spectral electric field. The spectral transfer function can be written analogously to the spectral electric field of the pulse as

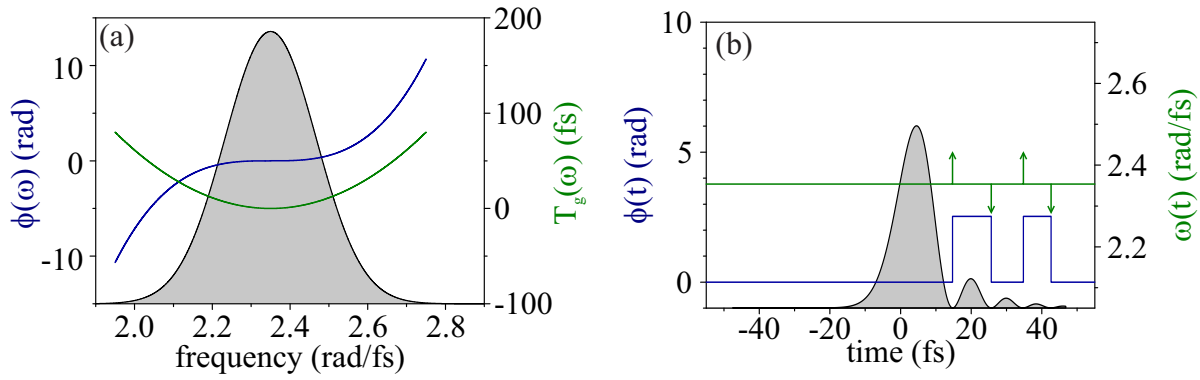

Figure 2.1.5: A pulse with a central wavelength of 800 nm, a temporal FWHM of 10 fs and a cubic spectral phase term $b_3 = 1000\,\mathrm{fs}^3$. Spectral intensity $I(\omega)$, spectral phase $\phi(\omega)$ and group delay $T_g(\omega)$ are shown in (a). Temporal Intensity $I(t)$, temporal phase $\phi(t)$ and instantaneous frequency $\omega(t)$ are displayed in (b).

$$M(\omega) = A_M(\omega)e^{-i\phi_M(\omega)}, \tag{2.1.18}$$

where $A_M(\omega)$ is the amplitude modulation, which is equivalent to the frequency dependent absorption of the element, and $\phi_M(\omega)$ is the phase modulation of the element[47, 51]. Inserting equation 2.1.18 into 2.1.17 vividly illustrates that the modulation phase gets added to the inherent phase of the pulse and therefore alters the pulse even in the absence of any absorption. Thus, the above-described decomposition of the spectral phase into polynomials of different orders is also useful for the natural dispersion of optical elements. A linear spectral phase is introduced by any optical element that involves the change of the refractive index. Since the speed of light c in a medium is connected to the speed of light in vacuum c_0 via the refractive index by

$$c = \frac{c_0}{n}$$

any change in the refractive index leads to a delay due to the lower velocity in the medium relative to a propagation where there is no medium. This delay can then be described by a linear spectral phase component b_1. The refractive index is in general also a function of frequency (or wavelength λ), therefore the speed of light in a medium is dependent on the frequency of the wave. If all the electromagnetic waves that make up a pulse enter an element with frequency dependent refractive index, every wave exits the medium with a different delay. Thus, an ordering of the frequencies is created, which can be described by a quadratic phase term b_2. Cubic phases may also be introduced by dispersion of optical elements, but are less relevant as discussed above. Higher order terms can often be neglected for linear optical media. The wavelength dependence of the refractive index of a given optical medium is usually a complex function. For wavelength that are not close to an absorption resonance of the medium, the refractive index function can be approximated by the empirical Sellmeier equation

$$n^2(\lambda) = 1 + \frac{B_1\lambda^2}{\lambda^2 - C_1} + \frac{B_2\lambda^2}{\lambda^2 - C_2} + \frac{B_3\lambda^2}{\lambda^2 - C_3} \tag{2.1.19}$$

with B_i and C_i being material constants. These coefficients are known and tabulated

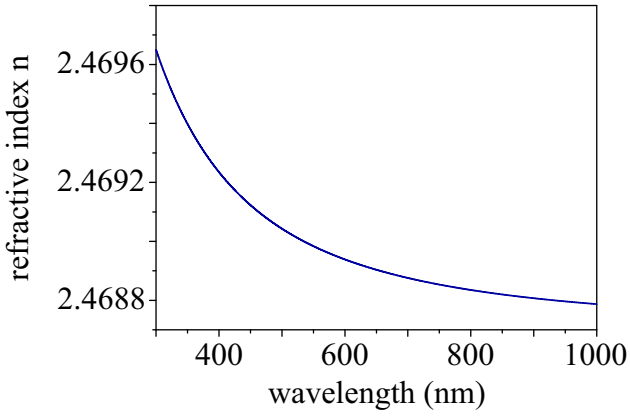

Figure 2.1.6: Approximation of the dispersion of the refractive index $n(\lambda)$ for *N-SF66* glass using the Sellmeier equation 2.1.19 for the visible and near infrared region.

by optical glass supplying companies (e.g. SCHOTT AG). For example for the glass *N-SF66* the constants are: $B_1 = 2.0245976$, $B_2 = 0.470187196$, $B_3 = 2.59970433$, $C_1 = 0.0147053225$, $C_2 = 0.0692998276$ and $C_3 = 161.817601$ [52]. An empirical approximation of the dispersion of the refractive index for *N-SF66* can thus be made and is shown in figure 2.1.6 for the visible and near infrared region.

2.1.3 Concept of a $4f$-pulseshaper

The effect of dispersion is usually an unwanted one occurring in all transparent optical media. However, the dispersion of a pulse may be compensated for by applying the same dispersion with a negative sign. Normal transparent media in the visible spectral regime are not suited for this, since the sign of the dispersion they introduce is always positive, unlike for the IR regime, where negative dispersion is possible [53]. But with diffractive elements such as prisms or gratings, it possible to disperse the pulse spectrally in space and then manipulate each frequency independently. Therefore an arrangement of two prisms or gratings and a mirror may be sufficient to compensate the natural positive dispersion by introducing a variable negative dispersion. These devices are called (prism or grating) compressor and are used routinely in mode-locked laser systems for dispersion control and in amplifier systems to enable *chirped pulse amplification*. An approach to imprint more arbitrary phases on pulses and thus, enable access to the field of pulse shaping, is the use of a zero dispersion compressor (ZDC) and a phase mask [54]. A ZDC is composed of two gratings or prisms and two cylindrical lenses or mirrors. The input pulse gets diffracted by the first grating (or prism). The first diffraction order is then collimated by a cylindrical lens (or mirror), which has its focus where the beam is diffracted on the grating. At a distance of one focal length in the direction of light propagation is the so called Fourier-plane. This is where each spectral component is projected into a sharp line. Putting a CCD detector here would yield the spectrum of the pulse. The ZDC is completed by a mirrored arrangement of a lens/mirror and a grating/prism, which has its Fourier-plane at the exact same location as the first setup. This device disperses the pulse spectrally, collimates it and then recombines the spectral components into a pulse again, without introducing any dispersion. However, it is easy to insert any phase or amplitude mask into the Fourier-plane of this device and thus, altering the spectral amplitude or

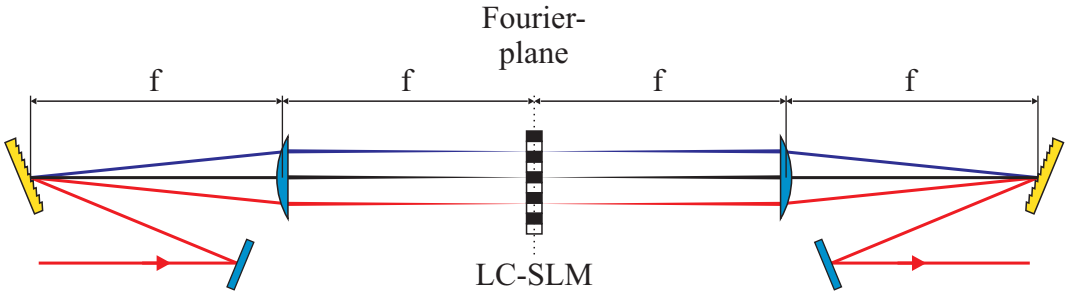

Figure 2.1.7: Basic layout of a $4f$-pulseshaper based on a zero dispersion compressor (ZDC) consisting of two gratings and two cylindrical lenses. The distance between the point of spatial dispersion and recombining of the pulse is four times the focal length as indicated. In the Fourier-plane a spatial light modulator (SLM) is placed to exert control over the spectral phase or amplitude of the pulse.

phase of the pulse. It is known from the previous section that such manipulation leads to control over the temporal profile as well.

It is evident that the shaping capabilities of this setup is highly dependent on the quality of the phase mask. For this purpose liquid crystal spatial light modulators (LC-SLM) are widely used [55–57]. These electronic devices are inserted into the Fourier-plane of the described ZDC and can be controlled via a computer. The geometry of this setup suggests the name of this device as a $4f$-pulseshaper, since it expands over a distance, which is just over four times the focal length of the used lenses/mirrors, to shape the spectral properties of the pulse. The whole setup is illustrated in figure 2.1.7. The LS-SLM is an electro-optical element consisting of two glass substrates with programmable pixels in between. These pixels are composed of two transparent electrodes made of indium tin oxide over which a voltage can be applied, as is depicted in figure 2.1.8a. In between these electrodes a solution of a nematic liquid crystals of rod-like molecules is placed. In absence of any voltage these rods are prealigned (see figure 2.1.8b) and therefore, the whole pixel is birefringent in nature because of the anisotropy of the electric dipole moments. Applying a voltage to the electrodes leads to a new alignment of the dipole moments of the liquid crystal molecules along the field lines (see figure 2.1.8c). This rotation takes place in one plane and therefore may change the refractive index of the pixel for an electromagnetic wave that is polarized in this plane. This can be done for every spectral component of the pulse separately and thus introduces a different group delay for every component, thereby changing the spectral phase of the pulse. This procedure is called phase shaping and alters the exponential term in equation 2.1.18. It is also possible to manipulate the amplitude of each spectral component, which corresponds to control over the first term in equation 2.1.18. This is achieved by placing a polarizer in front of the LC-SLM and a second one in crossed position behind the electro-optic element. The plane of alignment for the liquid crystals has to be 45° with respect to both axes of the polarizers. Thus the linear polarized electric field that enters a pixel can be written as two separate linear components that are polarized perpendicularly to each other. One of the polarization components is parallel to the plane of the liquid crystals and therefore may be manipulated. This results in a change of the polarization state of the overall electric field that exits the pixel. The second polarizer then absorbs the field either partially or completely and thereby alters the amplitude of that spectral component. This procedure

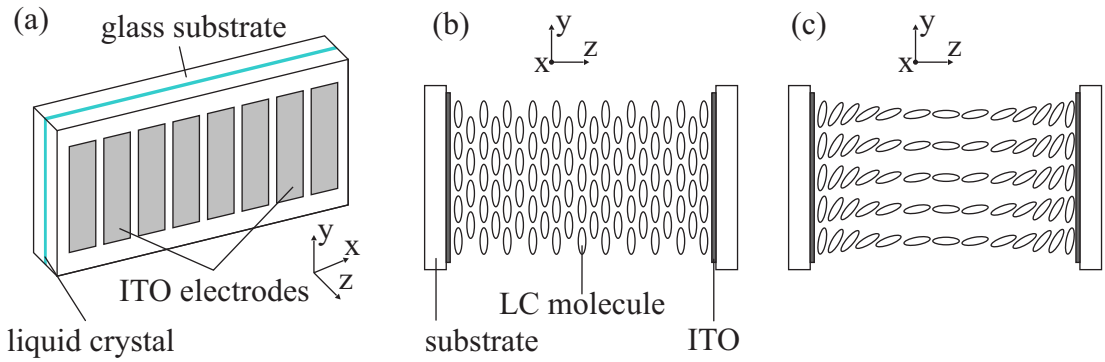

Figure 2.1.8: Basic layout of the pixels in an LC-SLM. (a) Front view: the pixelated indium tin oxide (ITO) electrodes are coated on the insides of the glass substrates and the liquid crystal solution is sealed inside. The light propagates in z-direction. (b) Top view into a single pixel with no voltage applied. All liquid crystals are oriented in y-direction. Upon applying a voltage the molecules rotate to face into the z-direction (c), thereby changing the refractive index for an electromagnetic wave with its polarization in the y-plane.

is done for every spectral component of the pulse and thus, amplitude shaping of the spectrum of a pulse is possible. By leaving the second polarizer out of the setup the same approach can be used to shape the polarization state of each spectral component[58, 59]. This whole technique can be expanded by using multilayer LC-SLMs [60], which enable the simultaneous control of two [61, 62] or even all three [63] of the mentioned properties.

2.1.4 Spatial properties of electromagnetic waves

The properties of electromagnetic waves discussed so far are solely time (or frequency) dependent. However, for the description of laser beams with their spatial and directional properties this is not sufficient. Therefore, the electric field in the wave equation 2.1.5 for beams is in general a function of the spatial variable $r = \sqrt{x^2 + y^2 + z^2}$. Furthermore the solution of 2.1.5 can also be complex, as already indicated by equation 2.1.9. Thus, complex valued solutions of the wave equation may take the form:

$$E(r,t) = \mathcal{E}(r)A(t)e^{i\omega_0 t}e^{i\phi_0}e^{i\phi(t)}. \tag{2.1.20}$$

Note that the spatial and temporal properties of the wave are separated here. Solutions for the temporal part of equation 2.1.20 have been discussed in section 2.1.1. In this case it was assumed that $\mathcal{E}(r) = 1$, hence equation 2.1.20 is a more generalized ansatz. Using this equation in the wave equation the *Helmholtz equation* for $\mathcal{E}(r)$ is obtained: [43]

$$\nabla^2\mathcal{E}(r) + k^2\mathcal{E}(r) = 0 \tag{2.1.21}$$

with

$$k^2 = \frac{\omega^2}{c^2}.$$

One solution of the Helmholtz equation is

$$\mathcal{E}(r) = \mathcal{E}_0 e^{ikr},$$

where k is the absolute value of the wave vector that is assumed to always point in the z-direction and $\mathcal{E}_0$ is a constant. Such a solution is called a plane wave and the electric field has the same amplitude at any point in a plane perpendicular to the z-direction. Thus, the field expands infinitely in the xy-plane. This does not describe regular laser beams, since they are not infinitely spread out. Another solution of 2.1.21 is

$$\mathcal{E}(r) = \frac{C}{r} e^{ikr}$$

where C is a constant. This field has the same amplitude on a sphere centered at $x = 0$, $y = 0$, $z = 0$ and is therefore called a spherical wave. Considering propagation in z-direction, the z coordinate may be replaced with the curvature radius R of the plane wave. Thus the spatial variable r changes to

$$r = \sqrt{x^2 + y^2 + R^2}.$$

However, spherical waves do neither describe laser beams, since they are propagating in all spatial directions at the same time and their intensity decreases by the inverse square law with respect to the point source, from which they originate. Beam-like solutions of equation 2.1.21 take the form

$$\mathcal{E}(r) = \mathcal{E}_0(r) e^{ikz}. \tag{2.1.22}$$

Assuming that $\mathcal{E}_0(r)$ and $\frac{\partial \mathcal{E}_(r)}{\partial z}$ only slowly changes with z leads to the *paraxial approximation* of the Helmholtz equation

$$\nabla_T^2 \mathcal{E}_0(r) + 2ik \frac{\partial \mathcal{E}_0}{\partial z} = 0 \tag{2.1.23}$$

which every beam-like electromagnetic wave has to satisfy [43]. In the most prominent form the solution to this equation takes the form of a Gaussian in the plane perpendicular to the propagation direction. It can be written as

$$\mathcal{E}_0(x, y, z) = A e^{ik \frac{x^2+y^2}{2q(z)}} e^{ip(z)}, \tag{2.1.24}$$

where A is a constant, q is a complex beam parameter that describes the size of the beamprofile in the xy-plane and p is a spatial phase parameter. Since both q and p are allowed to vary with z the beam diameter and phase within the spatial distribution may change upon propagation, respectively. Equation 2.1.24 is a solution to equation 2.1.23 if $q(z)$ and $p(z)$ meet certain requirements [43] that are

$$\frac{1}{q(z)} = \frac{1}{R(z)} + \frac{i\lambda}{\pi w^2(z)}$$

and

$$p(z) = i \ln \left(\frac{q_0 + z}{q_0} \right)$$

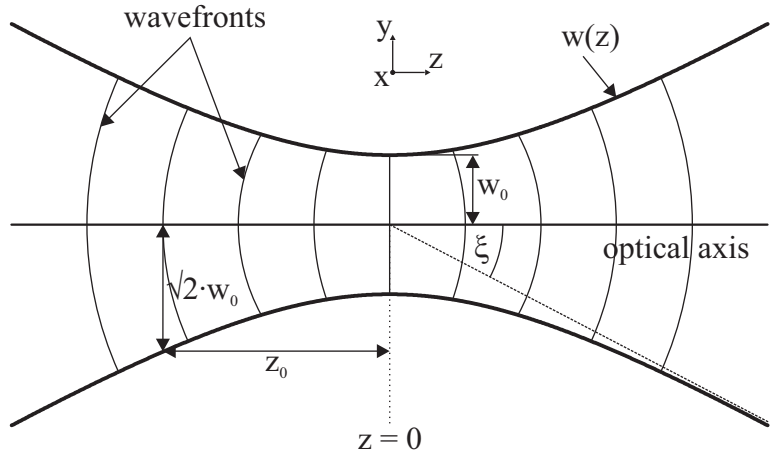

Figure 2.1.9: Gaussian laserbeam that propagates in space along z. The parameters characterizing the beam are the beam waist w_0 and the Rayleigh range z_0. Also displayed is the divergence angle ξ, the curvature of the wavefronts and change of the curvature upon propagating through $z = 0$.

where $R(z)$ is the radius of curvature of the waves at z, $w(z)$ is the spot size, that is the radius at which the intensity of the Gaussian distribution has decreased to a factor $1/e^2$ of its peak intensity [43] and $q_0 = q(0)$. By allowing $q(z)$ and $p(z)$ to be complex, it is possible to describe the complex spatial electric field by real parameters, which is convenient for describing laser radiation. Following this approach

$$R(z) = z + \frac{z_0^2}{z}$$

and

$$w(z) = w_0\sqrt{1 + \frac{z^2}{z_0^2}}$$

can be obtained. Where z_0 is defined by

$$z_0 = \frac{\pi w_0^2}{\lambda}$$

and is known as the *Rayleigh range*, and w_0 is the minimal sport size called *beam waist* along the direction of propagation. It is by definition located at $z = 0$. The Rayleigh range is the point in z-direction at which the beam waist has grown to $\sqrt{2}w_0$ and thus, describes how collimated the beam is. Following the above assumptions the last term in equation 2.1.24 can be rewritten as

$$e^{ip(z)} = \frac{1}{1 + \frac{iz}{z_0}} = \frac{1}{\sqrt{1 + \frac{z^2}{z_0^2}}}e^{-i\varphi(z)} = \frac{w_0}{w(z)}e^{-i\varphi(z)}$$

with

$$\varphi(z) = arctan\frac{z}{z_0}.$$

$\varphi(z)$ is called the *Gouy phase* and it describes the direction in which the wave front is curved upon propagation along z. In figure 2.1.9 the beam parameters for a Gaussian beam traveling along z and having a beam waist at $z = 0$ are visualized. The divergence angle ξ is also depicted. For $z >> z_0$ it can be assumed that the spot size grows linearly with z and thus, $\xi \approx \frac{w_0}{z_0}$. Note that figure 2.1.9 also displays the wavefronts of the electromagnetic wave along z and that the direction of curvature is the same for $-\infty < z < 0$, but flips at $z = 0$ to be opposite for $0 < z < \infty$. The behavior is described by the Gouy phase. This also implies that only at $z = 0$ the wavefronts are truly planar and outside the beam waist the wavefronts are curved like those of a spherical wave. For $z \to \infty$ the radius of curvature of the wave goes to infinity and therefore the Gaussian beam can be approximated as a plane wave for large z.
Bringing all the above definitions together to formulate the spatial field of a Gaussian laserbeam leads to:

$$\mathcal{E}(x, y, z) = A\frac{w_0}{w(z)}e^{ik\frac{x^2+y^2}{2R(z)}}e^{-\frac{x^2+y^2}{w^2(z)}}e^{ikz}e^{-i\varphi(z)}. \tag{2.1.25}$$

Higher-order Hermite-Gaussian laser beams

Equation 2.1.25 is however, only the simplest solution to the Helmholtz equation 2.1.21. Equation 2.1.24 can be modified to obtain a more generalized ansatz [43] in the form of

$$\mathcal{E}_0(x, y, z) = A \cdot g\left(\frac{x}{w(z)}\right) h\left(\frac{y}{w(z)}\right) e^{iP(z)}e^{ik\frac{x^2+y^2}{2q(z)}}. \tag{2.1.26}$$

The functions g and h scale with the spot size and determine the beam profile in the xy-plane perpendicular to the direction of propagation. Since g and h are functions of independent variables, a separation ansatz can be used to solve the differential equations associated with solving the wave equation. However, this whole procedure is rather lengthly [43] and therefore the solutions will only be discussed qualitatively here. The differential equations obtained for g and h are independent of each other, but resemble the problem of the harmonic oscillator from quantum mechanics. Thus, it is not surprising that the solutions g and h are in fact a perpendicular basis set formed by the Hermite polynomials [64, 65]

$$g\left(\frac{x}{w(z)}\right) = H_m\left(\sqrt{2}\frac{x}{w(z)}\right) \qquad h\left(\frac{y}{w(z)}\right) = H_n\left(\sqrt{2}\frac{y}{w(z)}\right)$$

with m and n being integer numbers describing the order of the polynomial. The phase parameter $P(z)$ in equation 2.1.26 reduces such that

$$e^{iP(z)} = \frac{w_0}{w(z)}e^{-i(m+n+1)\varphi(z)}.$$

Putting the solutions together yields the generalized Hermite-Gaussian field equation for laser beams:

$$\mathcal{E}_{mn}(x, y, z) = A\frac{w_0}{w(z)}H_m\left(\sqrt{2}\frac{x}{w(z)}\right)H_n\left(\sqrt{2}\frac{y}{w(z)}\right)e^{ik\frac{x^2+y^2}{2R(z)}}e^{-\frac{x^2+y^2}{w^2(z)}}e^{ikz}e^{-i(m+n+1)\varphi(z)}. \tag{2.1.27}$$

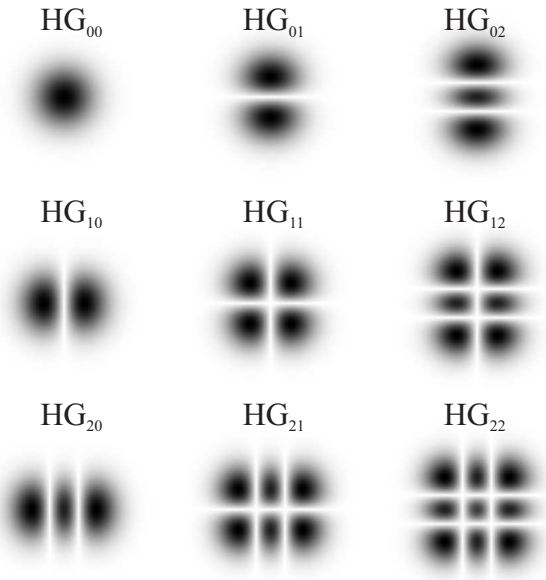

Figure 2.1.10: Intensity patterns of Hermite-Gaussian leaser modes according to equation 2.1.27 for mode indices of $m = 0, 1, 2$ and $n = 0, 1, 2$.

For $m = 0$ and $n = 0$ it is apparent that equation 2.1.27 reduces to equation 2.1.25 since the zeroth Hermite polynomial is a constant. Therefore, the simplest solutions of the Helmholtz equation is part of the more generalized set of solutions obtained here. In figure 2.1.10 the intensity of the simplest Hermite-Gaussian (HG) modes are depicted for $m = 0, 1, 2$ and $n = 0, 1, 2$. For increasing m or n an increasing number of intensity nodes appear within the beam profile. The nodes are oriented horizontally and vertically, also note their regular distribution. Most lasers produce exclusively the lowest order mode HG_{00}, however, this can be changed by introducing a slight disturbance within the cavity. If done correctly this disturbance lowers the gain for the HG_{00}-mode and the cavity prefers oscillation in a higher-order mode. This principle can also be used to suppress any higher-order mode.

Laguerre-Gaussian laser beams

From figure 2.1.10 it can be seen that the HG_{mn} modes show a rectangular symmetry. This is due to the Cartesian notation x and y in the plane perpendicular to the direction of propagation. By transforming the coordinates into the polar representation in r and θ, where r is now the distance from the beam propagation axis, a different set of solutions can be obtained for the Helmholtz equation in polar coordinates. This set of solutions takes the form [34]

$$\mathcal{E}_{pl}(r,\theta,z) = A\frac{w_0}{w(z)}\left(\frac{r\sqrt{2}}{w(z)}\right)^l L_p^l\left(\frac{2r^2}{w^2(z)}\right) e^{\frac{ikr^2}{2R(z)}} e^{-\frac{r^2}{w^2(z)}} e^{ikz} e^{-i(2p+|l|+1)\varphi(z)} e^{-il\theta} \tag{2.1.28}$$

with L_p^l being the associated Laguerre polynomials defined by [64, 65]

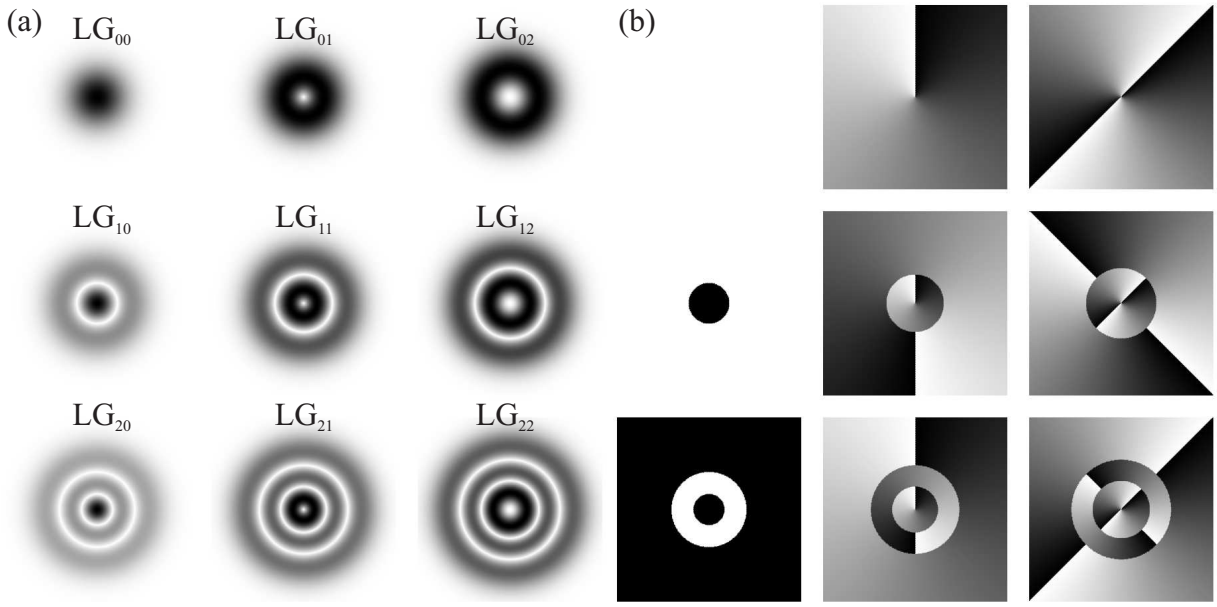

Figure 2.1.11: Intensity patterns of Laguerre-Gaussian laser modes according to equation 2.1.28 for mode indices of $p = 0, 1, 2$ and $l = 0, 1, 2$ (a) and the corresponding spatial phases on a scale from $-\pi$ to π (b).

$$L_p^l(x) = x^{-l} \frac{\left(\frac{d}{dx} - 1\right)^p}{p!} x^{p+l}.$$

The second fracture in equation 2.1.28 results in radial nodes in the intensity pattern, while L_p^l determines the intensity distribution around the nodes. The last exponential term $e^{-il\theta}$ in equation 2.1.28 leads to an azimuthal phase going on a circle around the beam axis. For any $l \neq 0$ this results in the existence of a phase singularity on the beam axis since all azimuthal phases from 0 to 2π are present. This produces an additional intensity node on the beam axis. This spatial phase corresponds to a orbital angular momentum (OAM) of the beam, which is not to be confused with the spin angular momentum of photons, which is associated with the polarization state. A photon can carry a spin and an orbital angular momentum, the total angular momentum is the sum of both. The intensity pattern of the first Laguerre-Gaussian LG_{pl} laser modes for $p = 0, 1, 2$ and $l = 0, 1, 2$ are illustrated in figure 2.1.11a. For $p = 0$ and $l = 0$ equation 2.1.28 again reduces to equation 2.1.25 and thus the lowest order mode in this basis set is the simple Gaussian laser mode again. The azimuthal phases of the modes are displayed in figure 2.1.11b on a scale from $-\pi$ to π. One unique property of the LG_{pl} mode set is that the mode indices l can also become negative integer numbers. This changes the handedness of the azimuthal phase, analogue to left- and right-handed polarization states. An interesting side effect of this is that the total angular momentum of a photon can be zero although the photon is circularly polarized, when the orbital angular momentum of the photon has the same magnitude but the opposite sign.

2.1.5 Nonlinear optical processes

To describe the light matter interaction, Ampère's law in the Maxwell equations has to be generalized from its free space form to contain the properties of the medium [50]. To that end the electric flux density $D = \epsilon_0 E + P$ is introduced. The modified equation takes the form:

$$\nabla \times B = \mu_0 J + \mu_0 \epsilon_0 \cdot \frac{\partial E}{\partial t} + \frac{\partial P}{\partial t}$$

with the polarization P of the medium

$$P = \chi_e \epsilon_0 E$$

that can be understood as the result of the interaction between field and medium. The parameter χ_e is the electric susceptibility of the medium. For dielectrics the polarization is mostly linear to the field E, however, for high field intensities there might be nonlinear components such that the above equation need to be modified to

$$\vec{P} = \epsilon_0 \left(\chi^{(1)} \vec{E} + \chi^{(2)} \vec{E} \cdot \vec{E} + \chi^{(3)} \vec{E} \cdot \vec{E} \cdot \vec{E} + ... \right)$$

with $\chi^{(n)}$ being the *nth* order susceptibility. The contributions of the terms to the overall interaction are diminishing quite fast with the order. The linear and quadratic terms are sufficient for all deliberations in the scope of this thesis. Thus, the polarization can be written with a linear and a nonlinear term $P = P_L + P_{NL}$. Inserting a real electrical field that consists of two frequencies ω_1 and ω_2 into the nonlinear polarization term yields [50]

$$\begin{aligned} P_{NL} &= \frac{\epsilon_0}{4} \chi^{(2)} \left[E(\omega_1) e^{i\omega_1 t} + E(\omega_2) e^{i\omega_2 t} + c.c \right]^2 \\ &= \frac{\epsilon_0}{4} \left[\chi^{(2)} E^2(\omega_1) e^{i2\omega_1 t} + \chi^{(2)} E^2(\omega_2) e^{i2\omega_2 t} + 2\chi^{(2)} E(\omega_1) E(\omega_2) e^{i(\omega_1+\omega_2)t} \right. \\ &\quad \left. + 2\chi^{(2)} E(\omega_1) E^*(\omega_2) e^{i(\omega_1-\omega_2)t} + \chi^{(2)} E(\omega_1) E^*(\omega_1) + \chi^{(2)} E(\omega_2) E^*(\omega_2) + c.c \right] \end{aligned}$$

with * denoting the complex conjugate. It can be seen from the equation that the nonlinear polarization has different contributions in this case. There are two terms that oscillate with $2\omega_1$ and $2\omega_2$, respectively. These are the second harmonics of their respective driving field, thus these terms describe the second harmonic generation (SHG). There is also one term that oscillates with $\omega_1 + \omega_2$, this is called the sum frequency of both driving fields (SFG). Next there is an oscillation with $\omega_1 - \omega_2$, which is the difference frequency (DFG). The last two terms are connected to optical rectification and are of no further interest. On a microscopic level the occurrence of this nonlinearity can be understood as a classic particle in an anharmonic potential driven by an external field. The equation of motion for this particle may be solved perturbatively leading to a time dependent motion of the particle that involves a term of oscillation with the driving frequency, but also a term that allows motion with twice the frequency of the driving field.
The above equation for the nonlinear polarization of the medium describe the second order processes that could occur. Each of these processes gives rise to an oscillation in the polarization, which becomes a source of electromagnetic radiation itself. Thus, second

harmonic, sum, and difference frequencies can be emitted by any medium with a sufficient second order susceptibility coefficient. However, there is an additional requirement that needs to be fulfilled and will be discussed by means of second harmonic generation. Considering a real 2ω field of the form

$$E = \frac{1}{2}\left[\mathcal{E}_{2\omega}(z)e^{-i(2\omega t - k_{2\omega}z)} + c.c\right]$$

which must satisfy the Maxwell equation

$$\nabla^2 E - \epsilon_0\mu_0\frac{\partial^2 E}{\partial t^2} = \mu_0\frac{\partial^2 P}{\partial t^2}$$

under the assumption that the polarization of the medium has a quadratic term. Finding a solution for $\mathcal{E}_{2\omega}(z)$ is possible when assuming that the driving ω field does not decrease in amplitude upon propagation along z. This leads to [43]

$$\mathcal{E}_{2\omega}(z) = i\omega\sqrt{\frac{\mu_0}{\epsilon_{2\omega}}}\chi^{(2)}\mathcal{E}_{\omega}^2(z)ze^{i\Delta kz/2}\left[\frac{sin\left(\frac{\Delta kz}{2}\right)}{\frac{\Delta kz}{2}}\right] \tag{2.1.29}$$

with

$$\Delta k = 2k_{\omega} - k_{2\omega} = 2\omega\sqrt{\epsilon_0\mu_0}[n(\omega) - n(2\omega)]. \tag{2.1.30}$$

Two things to note are that $\mathcal{E}_{2\omega}(z)$ scales with the square of the fundamental field and that Δk has a big influence on the overall field via the last term in equation 2.1.29. The first is not surprising when considering second order nonlinear effects, however, it unambiguously demonstrates that this process is more prominent in the intense field of a laser and laser pulses. However, the second requirement to the medium besides the existence of a second-order susceptibility, is shown by the emergence of Δk, which is called the phase mismatch. For Δk to vanish and thus, obtaining a maximum second-order field according to equation 2.1.30 the refractive index to the ω and 2ω field must be the same. This process is called phase matching and can be achieved in real media by different means. It is obvious that in a normal isotropic medium phase matching is not possible, since the refractive index of the medium is in general always a function of frequency. However, for a birefringent material this is not necessarily the case. Birefringence in crystals usually appears when there is no inversion center in the unitcell. This leads to a direction dependence of the materials polarization vector $\vec{P}$. In the simplest case a crystal has only one axis with respect to which it is birefringent and thus the material is uniaxial. This axis is called the optical axis and any electromagnetic wave polarized perpendicularly to this axis witnesses a refractive index of n_o, where $_o$ stands for ordinary. For a linear polarization parallel to the plane that formed by the optical axis and the direction of propagation the refractive index is n_e, with $_e$ denoting extraordinary [43]. By tilting the optical axis and varying its angle towards the propagation axis of the beam it is possible to match the refractive indices for the ordinary and extraordinary beam. Therefore this process is termed angular phase matching, which is the most prominent and in this thesis exclusively used method of phase matching. This means that the ω and 2ω fields do not have the same polarization. For Ti:Sapphire based femtosecond lasers with a central wavelength of about 800 nm, β-Barium borate (BBO) is the most common SHG crystal. To generate 400 nm light this way, a BBO crystal is needed that has its optical axes cut at 29.2° with respect to the

Phase matching Type	Polarization		
	ω_3	ω_2	ω_1
Type I	e	o	o
Type IIA	e	o	e
Type IIB	e	e	o

Table 2.1.1: Polarization of ω_1, ω_2 and ω_3 along the ordinary (o) and extraordinary (e) direction with respect to the optical axis for the different types of phase matching in the SFG process $\omega_3 = \omega_2 + \omega_1$ in a negative uniaxial crystal like BBO.[50]

beam propagation axis. This phase matching scenario is called Type I. There are also other types that originate from different starting conditions. In the above case energy that is transferred from the ω to the 2ω field must also obey the energy conservation, thus two photons from the ω field are converted to one photon of the 2ω field. In general, the two original photons do not need to originate from the same field. In fact, in the case of sum frequency generation there are already two different fields present. The polarizations of these fields do not need to be the same, they can even be perpendicular. In this case the phase matching angle for the crystal is just different. This leads to the different types of phase matching that are listed in table 2.1.1 for the general sum frequency case

$$\omega_3 = \omega_2 + \omega_1$$

which reduces to the in depth discussed case of SHG for $\omega_1 = \omega_2$.

2.2 Molecules and light

The previous section outlined the temporal and spatial structure of a laser beam by considering it as a wave. In this section the quantum mechanical structure of molecules will be explained alongside their interaction with the aforementioned light fields. The understanding of the dynamics followed by these interactions are necessary for understanding the studies presented in chapter 4.

2.2.1 Electronic structure of molecules

The state of a molecule consisting of N atoms and M electrons is fully described by its corresponding hamiltonian $\hat{H}$ in dependence on the locations r_M and momenta P_M of the electrons and locations R_N, momenta P_N, mass M_N, and charge Z of the nuclei, respectively: [66–68]

$$\hat{H}(r_M, R_N) = T_N(P_N, M_N) + T_e(P_M) + V_{eN}(Z, R_N) + V_N(Z, R_N) + V_e(r_M), \qquad (2.2.1)$$

where T denotes the kinetic energy of either the nuclei (N) or electrons (e). V describes the potential arising from the interactions of the electrons with the nuclei (eN), the nuclei among themselves (N) and electrons among themselves (e). Using this hamiltonian with the time independent Schrödinger equation

$$\hat{H}(r_M, R_N) \left|\Psi(r_M, R_N)\right\rangle = W \left|\Psi(r_M, R_N)\right\rangle \tag{2.2.2}$$

yields the total molecular energy W when $|\Psi(r_M, R_N)\rangle$ is the molecular wavefunction. Solving equation 2.2.2 for a molecule would give its energy, however, most of the time this is not possible in an analytical way. Therefore, approximations are necessary to simplify the computation. Most notably, the Born-Oppenheimer approximation is the most well-known estimation in the quantum mechanics of molecules. It states that since the nuclei are several orders of magnitude heavier than the electrons, the latter and the first are can be treated independently during the light matter interaction. This would result in a molecular wavefunction that consists of a wavefunction for the electrons that solely depends on the electron locations and the nuclei coordinates as a parameter and a wavefunction for the nuclei that solely depends on the nuclear locations. Therefore in the Born-Oppenheimer approximation the molecular wavefunction takes the form

$$\left|\Psi(r_M, R_N)\right\rangle = \left|\Psi_e(r_M, R_N)\right\rangle \left|\Psi_n(R_N)\right\rangle , \tag{2.2.3}$$

where the wavefunction of the electrons Ψ_e contain the nuclear coordinates R_M as a parameter, whereas the nuclear wavefunction Ψ_n is completely independent of the electron locations r_N. In that way, a time independent Schrödinger equation can be written for the electronic and the nuclear wavefunction:[67, 68]

$$(T_e + V_e + V_{eN}) \left|\Psi_e(r_M, R_N)\right\rangle = E(R_N) \left|\Psi_e(r_M, R_N)\right\rangle \tag{2.2.4}$$

$$(T_N + E(R_N) + V_N) \left|\Psi_n(R_N)\right\rangle = E \left|\Psi_n(R_N)\right\rangle . \tag{2.2.5}$$

The first gives the electronic energy eigenvalue $E(R_N)$ for a fixed conformation of the nuclei and the latter the energy eigenvalue E of the total system, which contains $E(R_N)$ as the averaged electron-electron and electron-nuclei interactions. Solving equations 2.2.4 and 2.2.5 in that order yields the potential energies of the molecule for every electronic state. These potential energy curves are actually surfaces in a multidimensional space since the degrees of freedom of the whole system increases with the number of nuclei and electrons in the system. For simplicity, the whole surface is usually projected on one interatomic coordinate for the purpose of a better visualization. The degrees of freedom of a molecule are translation, rotation, vibration, and electronic excitation and the exact energy of a molecule depends on the potential energy of the state (i.e. electronic state) and the energy within its degrees of motion. Especially the vibrational and rotational states can carry energy in the same or a few orders of magnitude less than the potential energy of the molecule. The electronic states of the molecule resemble an anharmonic potential, in which the vibrational states are stacked with decreased spacing towards higher energy. On top of the vibrational states are the rotational ones, which are of no further interest for this thesis and are therefore not discussed. In figure 2.2.1 the potential energy curves S_0 and S_1 of a fictional molecule are displayed in dependence on the internuclear distance R. For each electronic state the absolute squares of the vibronic wavefunctions for the states $\nu = 0$ and $\nu = 3$ are shown as well. Note that both curves have their minimum at different coordinates, which is common and known from atomic states, where the mean distance of an electron also increases with its energy. Another aspect that is hinted in figure 2.2.1 is that there are only a finite number of bound vibrational states within one electronic state. This means that by increasing the vibrational energy of a molecule an

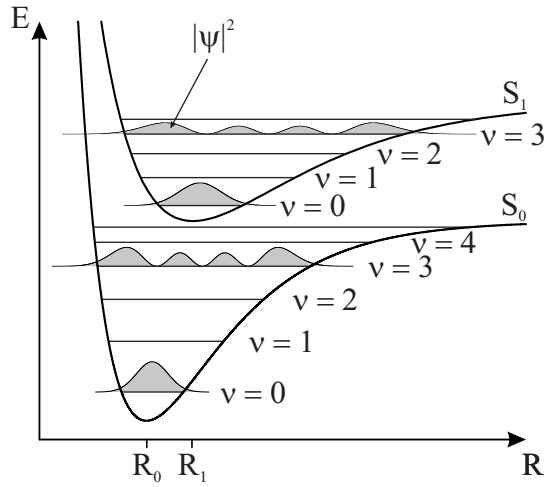

Figure 2.2.1: The first two potential energy curves S_0 and S_1 of a fictional molecule. Since the electronic states have a strong anharmonic character the energy distance between adjacent vibrational states decrease with the vibrational quantum number ν.

unbound state can be reached, which is equivalent to thermal dissociation of the molecule. [67]

2.2.2 Transitions in molecules

The interaction of molecular systems described in the previous section with light fields described in section 2.1 lead to different types of transitions in the molecule. According to Fermi's golden rule the probability of a transition w_T is proportional to the square of the dipole matrix element, which is the result of the electric dipole operator μ acting upon the wavefunctions of the initial an final state of the system

$$w_T \propto |M_{i\to f}|^2 = |\langle\Psi_i|\,\mu\,|\Psi_f\rangle|^2.$$

When taking the Born-Oppenheimer approximation into consideration and writing the wavefunctions of the initial an final state as a product of an electric and a nuclear wavefunction the dipole matrix element can be rewritten as

$$M_{if} = \langle\Psi_{n,i}\Psi_{e,i}|\,\mu_n + \mu_e\,|\Psi_{n,f}\Psi_{e,f}\rangle$$

assuming that the dipole operator consists of two parts that depend either on the electrons or the nuclei. Furthermore, since the electric wavefunctions are an orthogonal set of functions the dipole matrix element takes the form

$$M_{if} = \langle\Psi_{e,i}|\,|\mu_e|\,|\Psi_{e,f}\rangle \times \langle\Psi_{n,i}|\,|\Psi_{n,f}\rangle$$

where the absolute square of the second term is called the Franck-Condon factor. It describes if and to what extent a transition is possible by looking at the overlap integral of the vibrational wavefunctions. The better the overlap the higher the transition probability. These transitions would be depicted as vertical lines in the representation of the molecular energy state diagram illustrated in figure 2.2.1 in compliance with the Born-Oppenheimer approximation that assumes electronic motions to be much faster than

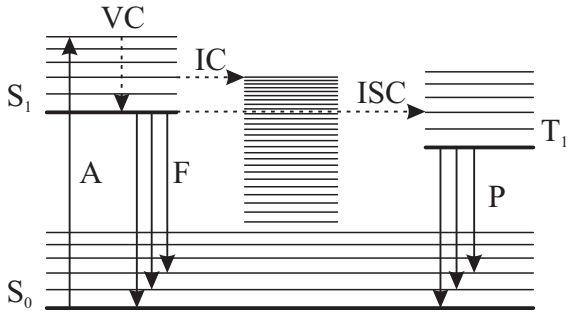

Figure 2.2.2: Jablonski diagram of the electronic and vibrational states of a fictional molecule. The electronic states S_1 and S_2 have the same symmetry, whereas T_1 has a different one. The radiative (solid) and nonradiative (dashed) intramolecular transitions are depicted as arrows connecting two states. The processes absorption (A), fluorescence (F), phosphorescence (P), vibrational cooling (VC), internal conversion (IC) and intersystem crossing (ISC) are differentiated.

nuclear ones. The overlap for a transition from the vibrational ground state of the electric ground state to the vibrational ground state of an excited state is usually lower than to a vibrationally excited state. This is due to the relative shift in the equilibrium distance of the electronically excited states as can be seen from figure 2.2.1. The representation of molecular transitions on potential energy surfaces or curves is often complicated and thus visualization is usually done on a more simple energy diagram. These Jablonski diagrams can be seen as an integration over all molecular coordinates, the potential energy surfaces are therefore converted into lines of constant energy [67]. In figure 2.2.2 such a diagram is shown for a system of three states. The ground state S_0 with its vibrational levels is the lowest electronic state. The state S_1 is energetically higher, whereas the state T_1 is in between S_0 and S_1. T_1 is different to the other two states and has a different symmetry. Radiative transitions in the diagram are depicted as solid arrows and nonradiative as dashed arrows. Radiative transitions are absorption (A), fluorescence (F) or phosphorescence (P). Nonradiative processes are vibrational cooling (VC), internal conversion (IC) and intersystem crossing (ISC). After the absorption of a photon, the excess energy within the electronically excited state is quickly redistributed, either within the molecule, which is termed intramolecular vibrational relaxation, or by energy transfer to the solvent, which is called vibrational energy transfer. These processes are usually fast, on the order of several ten femto- to some hundred picoseconds [69], depending on the solvent properties. Subsequently to the vibrational cooling, several different processes can occur. The vibrational ground state of the electronic excited state can undergo internal conversion (IC) into a vibrationally excited state of the electronic ground state, which can occur in most systems, although it might not be the dominant relaxation path. The system can also go back to its equilibrium state by emitting electromagnetic radiation in form of fluorescence (F) followed by further vibrational cooling. The latter and IC are both spin conserving, whereas the next two are not. From the vibrational ground state of the excited electronic state the molecule can undergo intersystem crossing (ISC) to reach the triplet state T_1. After VC within T_1 the system can relax to the electronic ground state by another ISC (not shown) or by phosphorescence (P), which involves emitting a photon and simultaneously changing the symmetry of the wavefunction. Both ISC and P are dipole forbidden and are usually less likely, but not impossible, and in some systems

ISC can even be the dominant process [70].
Since fluorescence is of further interest for chapter 4 it shall be discussed in more detail. After excitation, vibrational cooling of a molecule may end in a state from which it can emit a photon and thus, relax to the ground state. The emission itself is a statistical effect and for a single molecule it can occur at any time after excitation, however, the probability is a function of time. Considering an ensemble of N_i excited molecules that undergo fluorescence, then the change in the population of the excited state over an interval dt can be written as

$$dN_i = -k_r N_i dt, \tag{2.2.6}$$

where k_r is the radiative rate for the respective transition. Therefore the time dependent population of the excited state is

$$N_i(t) = N_i(0)e^{-k_r t}, \tag{2.2.7}$$

where $N_i(0)$ is the population at the beginning. This exponential decay is fully characterized by $k_r = \tau^{-1}$, where τ is the so called lifetime of the fluorescence. Usually there are more than one deactivation channels at work in a real molecule, so not all N_i molecules, that populate the excited state, may take the radiative pathway. The fraction

$$\Phi = \frac{N_i^r}{N_i} \tag{2.2.8}$$

of the subpopulation N_i^r taking the radiative channel to the total excited molecules N_i is called fluorescence quantum yield. The rate equation for multiple relaxation processes changes to

$$dN_i = -(k_r + k_{nr})N_i dt, \tag{2.2.9}$$

where k_{nr} denotes the nonradiative relaxation rate. The fluorescence quantum yield can then also be defined as

$$\Phi = \frac{k_r}{k_{nr} + k_r}. \tag{2.2.10}$$

Experimentally the sum of all rates that depopulate the radiative state can be obtained from time-resolved fluorescence measurements that are outlined in the next section, but the radiative rate alone is difficult to measure. However, by knowing the fluorescence quantum yields the radiative and nonradiative rates can be estimated as

$$k_{nr} = \frac{1-\Phi}{\tau} \qquad \text{and} \qquad k_r = \frac{\Phi}{\tau}. \tag{2.2.11}$$

2.3 Time-resolved fluorescence spectroscopy techniques

In the previous section the dynamics of fluorescence were introduced. This section will deal with the techniques used to measure it. To this end, first a general model of multi-exponential decays measured by any experimental setup will be given. Following that, a universal detection scheme for light will be introduced. In the end two subsections will

present two standard techniques of time resolved fluorescence detection.
An excited molecule usually has multiple ways of relaxing as already mentioned. There is also the possibility of multiple radiative pathways back to the ground state. This would result in a multiexponential decay of the fluorescence, one decay constant for each path. The fluorescence intensity I_{fluo} is proportional to the number of molecules choosing a radiative decay path. Equation 2.2.7 then takes the form

$$I_{fluo} = \sum_{j=1}^{n} A_j \cdot e^{-t \cdot k_j} \tag{2.3.1}$$

with j being the number of radiative decay pathways. The amplitude constant A_j for each decay includes the proportionality factor between the population and the intensity. In the last step this equation is convoluted with the instrument response function (IRF), which includes the time resolution of the instrument with which the decay is measured, to form the model function which describes all the measured data in this thesis:

$$I_{measured} = \mathrm{IRF} \otimes \sum_{j=1}^{n} A_j \cdot e^{-t \cdot k_j} + c, \tag{2.3.2}$$

where the convolution is denoted by $\otimes$ and c is a constant baseline offset. The IRF is characteristic for each device and may vary significantly for different techniques. The time resolution of any such device is basically limited by its gate function. The most common device for measuring coherent light is a photo diode, which is a semiconductor base opto-electric instrument. However, its sensitivity is limited and the spontaneous emission of fluorescence may not exceed the sensing threshold of such diodes. Therefore, photo multiplier tubes (PMT) are commonly used for the detection of incoherent light such as fluorescence. A PMT consists of a series of electrodes. Upon irradiation and absorption of a photon on the first electrode a photoelectron is released via the photoelectric effect [71, 72]. This electron is then accelerated with a high voltage onto the second electrode, where it releases several electrons via the energy transfer of its collision. This process is repeated many times until a measurable current is generated. The amplitude of this current is proportional to the amount of photons starting this whole sequence. The amplification of the signal intensity by the PMT can be as high as 10^6, which even enables detection single photons [73]. However, a PMT is only sensitive to the amount of light, not its frequency. Unfortunately, the photon energy carries information about the states that were involved upon generating the photon and is thus interesting for understanding the occurring processes. Therefore, a second device is necessary to enable frequency resolution for the detection. The most common way of doing this is by using a monochromator. This instrument consists of two slits and a dispersive element, usually a grating. Light entering the monochromator through the first slit is dispersed into its spectral components via the dispersive element. Only a narrow bandwidth of the spectrum may then exit through the second slit. By turning the dispersive element, the spectrum of the incident light can be shifted across the second slit and thus, only a specified portion of the incident spectrum can exit the monochromator and be measured by a PMT. This monochromator-PMT unit is commonly found in steady state and time resolved spectrometers for measuring absorption and emission.

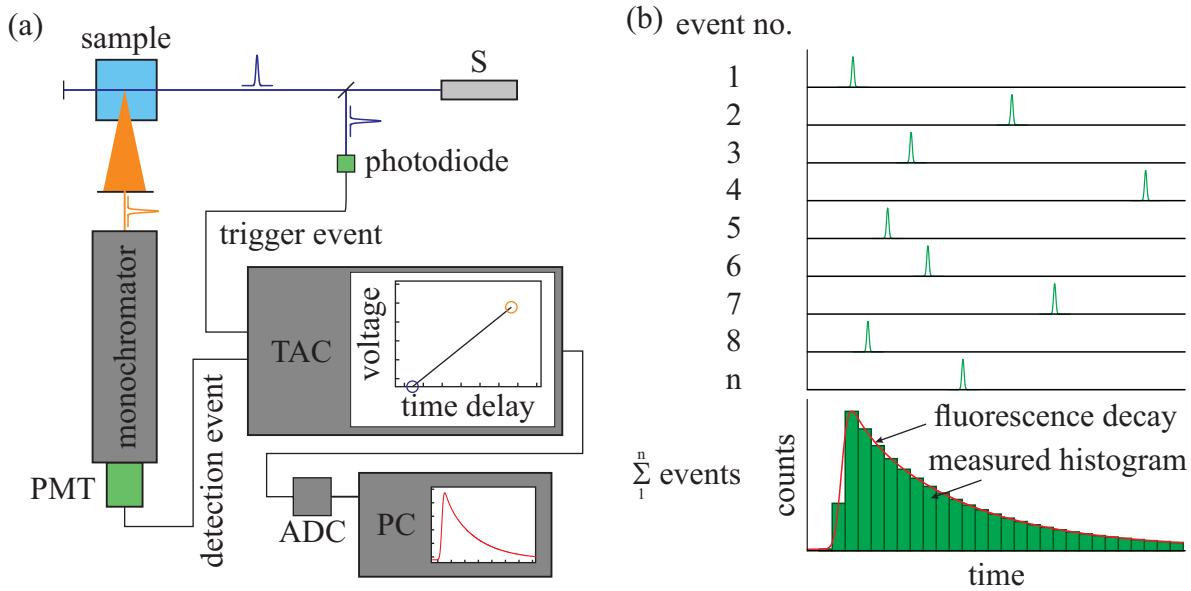

Figure 2.3.1: Scheme of the TCSPC technique (a) with an excitation light source (S), the sample, a detector (D), the time-to-amplitude converter (TAC), analog-to-digital converter (ADC) and a computer (PC). All registered events sum up to a histogram, that follows the fluorescence decay (b).

2.3.1 Time correlated single photon counting

One of the more commonly used techniques to determine the time constants of fluorescence processes is the time correlated single photon counting (TCSPC). The basic setup of these devices is depicted in figure 2.3.1a. A pulsed light source (S) excites the sample. At the same time as the pulse exits the source an electric signal is given to the time-to-amplitude converter (TAC). The excited sample emits a fluorescence photon, which is registered by the detector (D) that sends a second signal to the TAC. Within this device, the first signal starts a linear voltage ramp that increases on the nanosecond timescale. The second signal then stops the ramp and the voltage represents the time delay between the start of the experiment by the excitation pulse and the end by the detection of the fluorescence photon. The travel times of the photons to the sample and the detector are constant and only the temporal evolution of the emission process dictates the overall time between the trigger and detection event. Since fluorescence is a spontaneous effect it is more or less random when the emission of a photon from the sample occurs. Despite that, a single photon does not carry information about the whole emission process, the key to this technique is that this experiment is repeated millions and millions times. The TAC output voltage of each iteration is stored in a PC via a analog-to-digital converter (ADC). All registered events then take the form of a histogram, which follows the fluorescence time evolution convoluted with the IRF of the instrument as visualized in figure 2.3.1b. The pulsed light sources that can be used in this technique range from nanosecond to femtosecond lasers and also laser diodes (LD) and pulsed light emitting diodes (LED). The latter two being the most common nowadays, as they provide short pulses in the range of several tenth picoseconds, give access to a wide range of excitation wavelength and are very compact. The repetition rate of the source is another crucial feature, since the single experiment has to be done many times over. This gets further stressed out by

the fact that only every 100th excitation pulse is supposed to lead to the detection of an emission photon. This has to be the case since the TAC is stopped by the first photon that the detector registers. Since the probability of the emission of a photon for early times of the decay is much higher than for the later times the count rate on the detector must be low enough that events where two photons are emitted can be excluded. In these cases the second photon would be omitted and the measured histogram would be biased towards early emission events. The detector usually is a PMT since it is sensitive and has a fast reaction time. The addition of a monochromator enables wavelength sensitivity of the measured fluorescence decay. The limitation of the time resolution of this technique originates from the detection unit, which is several hundred picoseconds for most PMTs or by the light source if nanosecond pulses are used. If the dynamics surrounding the fluorescence are faster than 100 ps TCSPC is unable to give reliable results. [74]

2.3.2 Fluorescence upconversion

To overcome the limitation of the time resolution of the TCSPC, a differently designed technique has to be applied. Femtosecond fluorescence upconversion comprises an all-opticalprinciple and has a significantly more complex setup. It relies on the shortest time events in the visible region that are possible, femtosecond laser pulses. An introduction to these pulses is given in section 2.1. However, the light source is not the limiting factor for TSCPC either, rather than the detection scheme. With fs pulses this can be overcome by a design shown in figure 2.3.2. The key to this technique is that the pulses delivered by the laser are split into two beams of an interferometer-like setup. While one beam excites the sample, the second one can be delayed with respect to the first. The fluorescence generated by the first beam is collected, usually by spherical or parabolic mirrors, and then focused into a sum-frequency generating crystal after the excitation beam is blocked by a filter. There, the second pulse is spatially overlapped and temporally varied. The SFG process (for details see section 2.1.5) results in a signal whose intensity is dependent on the delay of the second beam with respect to the first one and thus, which respect to the emitted fluorescence. This allows gating of the fluorescence decay by spatially elongating one beam path. The fluorescence and gate are focused into the crystal with a small angle between them. For reasons of momentum conservation, the generated SFG signal travels in between the two incident beams. Those are then easily spatially filtered and thus do not interfere with the detection of the SFG signal. The time resolution of this technique is therefore only limited by the actual pulse length and not the temporal response of the detector. The generated SFG signal can then be measured by a monochromator-PMT unit to evaluate its intensity and gain access to the spectral information. The excitation wavelength of this technique is not strictly limited to the wavelength of the laser spectrum, but also includes its higher harmonics. The SHG of the laser can very easily used by implementing a suitable BBO crystal and optical filter into the excitation beam. Also the third harmonic generation (THG) is accessible via an additional SFG step involving the SHG and fundamental pulse. Since fs lasers can also be constructed with a certain variability in its central frequency there is some flexibility in the excitation wavelength with one laser, which is explained in section 3.1.4 and demonstrated in the experiments in chapter 4. However, to span the whole frequency range of LDs and LEDs several lasers and more complicated frequency conversion schemes would be needed in

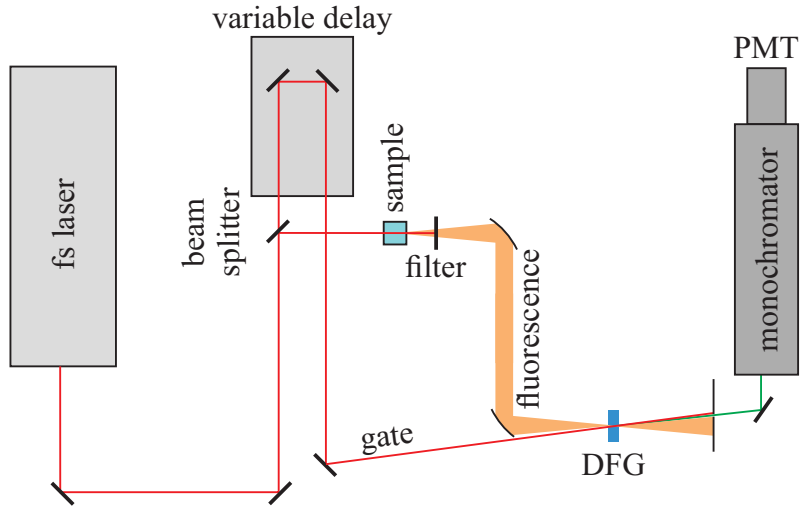

Figure 2.3.2: General setup for femtosecond fluorescence upconversion. The laser is split into two paths, one that excites the sample and one that pose as a variable gate for a sum frequency signal that is detected by a monochromator-PMT unit.

addition to fs lasers being more complex themselves. [74, 75]

CHAPTER 3

EXPERIMENTAL TECHNIQUES

The previous chapter outlined the theoretical background of the studies presented in this thesis, starting from femtosecond laser pulses and their temporal, spectral and spatial properties to the energetic molecular structure and the basic principle of the time resolved spectroscopy techniques used here. This chapter will give a more detailed overview of the instrumentation. The first section will provide a detailed insight into how the fluorescence studies of the investigated tetrazolium salt were performed. Therefore, the sample preparation from the precursor will be explained, how the quantum yield of the prepared sample in different solvents was determined, and a detailed insight into the TCSPC and fs-upconversion devices will be given. The second section will deal with the setup for shaping the temporal and spatial properties of light. To this end, the laser system with its pulse parameters and their determination will be presented, how the conversion of a HG-mode to a higher order LG-mode is performed, the used $4f$-pulseshaper will be discussed in more detail, and how the whole setup is combined on the laser table.

3.1 Instrumentation for the fluorescence studies

The goal of this project was to determine the fluorescence dynamics of a tetrazolium salt in solutions of different alcohols. This class of molecules is known since 1894 [16] and is known to have a rich photochemistry [25, 31, 76], which led to many applications[17–24]. The investigated compound is one of the few known fluorescing tetrazolium salts[31]. The study included steady-state absorption and emission spectroscopy as well as determination of the fluorescence quantum yield in different alcohols. Furthermore, time resolved experiments have been performed to reveal the emissive decay lifetimes on the time scale from a couple of nanoseconds down to 100 femtoseconds.

3.1.1 Sample preparation

Tetrazolium salts are widely used in cell biology, agriculture and cancer research, for example, therefore it is not surprising that a lot of compounds in this class are readily available from commercial retailers. Unfortunately, the investigated phenyl-benzo[c]tetrazolo-

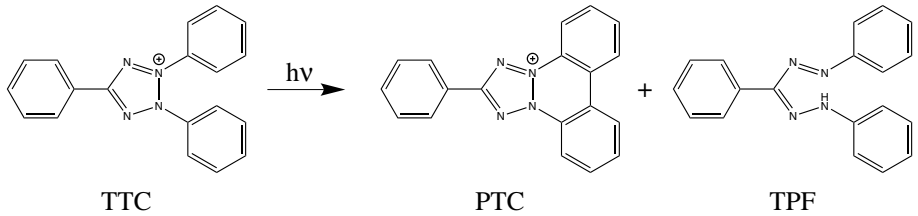

Figure 3.1.1: Photoreaction of TTC to PTC and TPF. In alcohols, only PTC is formed, while aqueous solutions favor a mixture of TPF and PTC.

cinnolium chloride (PTC) is not, due to its light sensitivity and up to now limited commercial applications. However, it can be derived from the commercially available 2,3,5-triphenyl-tetrazolium chloride (TTC) (CAS number 298-96-4, Sigma-Aldrich) by means of a simple photoreaction. This reaction (illustrated in figure 3.1.1) has PTC as its sole product in alcohols [31, 76] but may also lead to 1,3,5-triphenyltetrazolium formazan (TPF), which is the main photoproduct in aqueous solutions. The normalized absorption spectra of TTC and TPF are shown in figure 3.1.2 (a) and (b) respectively. The samples for the studies presented in this thesis were prepared by illuminating a TTC sample with 254 nm light from a VL-4.LC lamp by Vilbert Lourant, which has an output power of 4 W at 254 nm. The generation of PTC was monitored via a Jasco V-770 steady state absorption spectrometer and a Jasco FP-8300 steady state emission spectrometer. The accumulation of PTC from a 3.9 μmol/L TTC solution can be seen in the absorption spectra in figure 3.1.3 for steps of two minute exposure to the UV lamp. The spectral features are of no further interest here and are explained in detail in section 4.1. At this point, only note that the shape of the spectrum does not significantly change upon irradiation, only the amplitude of the whole spectrum is altered. Also no absorption above 400 nm is present, thus TPF generation can be excluded. The inset in figure 3.1.3 shows the absorbance at 265 nm versus the exposure time. From this, it is evident that a rapid buildup of the absorption at this wavelength takes place and that after about ten minutes photodegradation sets in and PTC gets partially destroyed. The quantum yield and TCSPC measurements were performed with cuvettes of 2 mm thickness, in which the samples were also prepared. For TCSPC experiments the starting concentration of TTC for the samples was 8.1 μmol/L, the corresponding results can be found in section 4.3.1. The quantum yield determination was performed according to section 4.2 and the

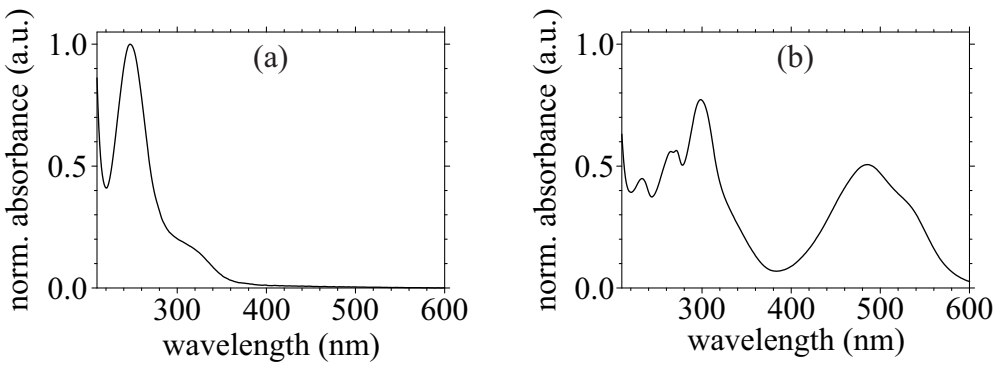

Figure 3.1.2: Normalized absorption spectra of TTC in ethanol (a) and TPF in ethanol (b).

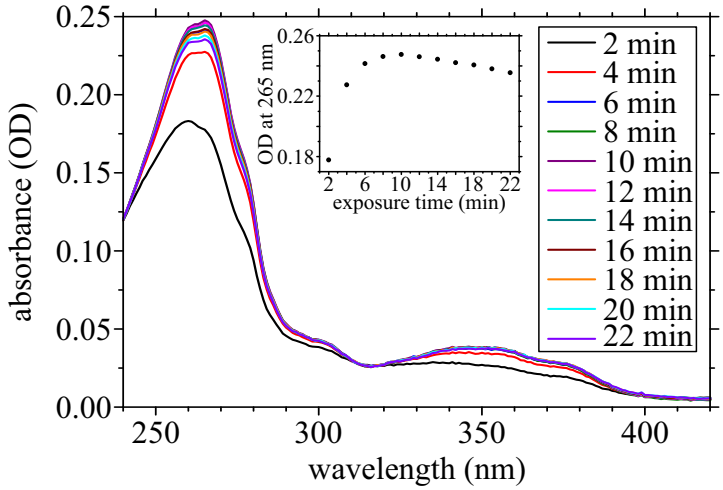

Figure 3.1.3: Photogeneration of PTC from TTC in ethanol visualized via the change in the absorbance after two minute steps of exposure to the 254 nm lamp. The inset shows the absorbance at 265 nm versus the exposure time.

results can be found in section 4.2. For the upconversion measurements, however, the photodegradation has to be considered, since measurements of this kind naturally take more time. Therefore, a peristaltic pump was necessary to achieve an exchange of PTC in the interaction volume with the excitation laser. To this end, a volume of 100 mL of a 40.3 μmol/L TTC solution was irradiated in a beaker with the UV lamp shining from the top into the solution, since the glass of the beaker is not transparent for the used UV light. Similar as before the time of optimal irradiation was tested and found to be about 70 min before photodegradation sets in. The results of this study can be found in section 4.3.2.

3.1.2 Fluorescence quantum yield determination

The ratio of radiatively decaying molecules to the total of the excited molecules is the fluorescence quantum yield according to section 2.2.2. The determination of the absolute fluorescence quantum yield of a fluorophore is quite challenging. There are however some techniques that allow its deduction rather accurately. The definition of the quantum yield can be rewritten as the ratio of the emitted photons relative to the absorbed photons. Estimating the number of absorbed photons experimentally can be done with photon counting devices such as photodiodes and PMTs down to a single-photon scale. However, measuring the exact amount of emitted photons is rather complicated since fluorescence is spontaneous in its timing and direction. The most common setup for the latter is an integrating sphere, where the sample is put in the center of a sphere that is reflective on the inside [77]. The excitation light can enter through a small hole. The fluorescence that is radiated in all directions gets reflected multiple times in the inside of the sphere and eventually exits into a fiber that is coupled to the sphere. The accurate measurement of the number of emitted photons is then done with a spectrometer with a highly sensitive detector to enable single (or near single) photon accuracy[78]. There are also other methods of determining the absolute fluorescence quantum yield like thermal lensing [79] and photoacoustic spectroscopy [78, 80]. Both exploit the temperature change of the sam-

ple upon absorption. The first directly measures the temperature change in the sample and thus estimates the nonradiatively decaying subpopulation, while the second does the same by measuring the amplitude of the pressure wave emanating from the temperature jump by an acoustic sensor. All three methods are however quite complicated and are not suited for every day lab routine. Fortunately, there is also a method to determine the relative fluorescence quantum yield [81, 82]. All that is needed for this are steady-state spectrometers and one or two reference fluorophores with known quantum yield. These references can be found in literature and are usually determined by means of an absolute method. A measurement of the absorption and fluorescence spectrum of both the reference and investigated substance is enough for an estimation of the fluorescence quantum yield. Since the relative absorption is connected to the number of absorbed photons and the integration of the emission spectrum is an equivalent of the amount of emitted photons, only an instrument factor remains in both cases. Thus the ratio of the quantum yields Φ_i of the reference R and test sample X is the same as the ratio of their integrated fluorescence intensity EM to their absorbance AB at the excitation wavelength

$$\frac{\Phi_X}{\Phi_R} = \frac{\dfrac{\int EM_X(\lambda)}{AB_X(\lambda_{ex.})}}{\dfrac{\int EM_R(\lambda)}{AB_R(\lambda_{ex.})}} \tag{3.1.1}$$

and the instrument factors cancel each other. However, this method is rather prone to errors, since concentration effects, different solvents and the reliability of the reference are not considered. A more refined way is the use of two references and performing a series of measurements for different fluorophore concentrations. The absorbance is expected to rise with the concentration according to the Beer-Lambert law, and so does the fluorescence intensity. Plotting the latter against the first leads to a linear increase, whose slope is proportional to the fluorescence quantum yield. That way, concentration effects can be excluded. By using two reference substances, one can be calibrated against the other and vice versa, if both calibrations lead to the respective literature value the spectrometer settings and calibrations can be seen as constant factors. Lastly, the refractive indices n_i of the solvents are added to form the empirical relation

$$\Phi_X = \Phi_R \left(\frac{G_X}{G_R}\right) \left(\frac{n_X}{n_R}\right)^2 \tag{3.1.2}$$

with G_i being the gradient of the integrated fluorescence intensity versus the absorbance at the excitation wavelength. For the studies in this thesis harmane in H_2SO_4 and anthracene in ethanol were chosen, since they have similar absorption and emission characteristics as PTC. Furthermore, their fluorescence quantum yields from literature are 81%[83] for harmane at 365 nm excitation wavelength and 27%[84] for anthacene at 340 nm excitation. For each reference, six solutions with concentrations between 6.6 μmol/L and 12.1 μmol/L for harmane and 6.7 μmol/L and 12.3 μmol/L for anthracene were prepared. For the PTC investigation six TTC solutions with concentrations from 36 μmol/L to 66 μmol/L were prepared in methanol, ethanol, ethylene glycol, and glycerol. The preparation of each sample was done according to section 3.1.1 with irradiation times ranging from 22 min to 32 min for the respective concentrations to make sure the actual PTC concentration in

the samples was at its maximum.

3.1.3 TCSPC device

The TCSPC experiments presented in this thesis were performed with a commercial FluoTime 200 device by PicoQuant GmbH. It is a state-of-the-art instrument [85, 86] using the same principle described in section 2.3.1. The time-to-amplitude as well as the analogue-to-digital converter are integrated into a card on a PC board. In addition to what is described in section 2.3.1 there are two polarizers implemented, to enable the device to perform anisotropy experiments. All the measurements shown in this thesis were performed under the magic-angle of $\theta = 54.7\,^{\circ}$ [87, 88], so no anisotropy results are reported. The excitation light source used was a LDH-P-C-375 picosecond laser diode with a central frequency of 375 nm. The diode was operated by a PDL 800-B driver, which triggered the diode as well as the TAC. The driver also controlled the pulse energy of the attached laser head and its repetition rate between 2.5 MHz and 40 MHz. The latter enables an adjustable time window of the measurement from 400 ns down to 25 ns for the respective frequency. For the measurements done in this thesis, it was found that the fluorescence dynamics in methanol and ethanol are finished within 25 ns, while it lasted slightly longer in ethylene glycol and glycerol. Therefore, the repetition rate was set to 40 MHz for the measurements in methanol and ethanol and to 20 MHz in ethylene glycol and glycerol. The laser diode was specified with a pulse width of 52 ps, however the IRF of the whole instrument was limited to the reaction time of the PMA-C 182-N-N PMT. Therefore, the IRF was measured in situ by the elastic scattering of a LUDOX® (colloidal silica) solution, which can be seen as instantaneous on the time scale of this device [89]. By detecting at different wavelengths, uncertainties in the central frequency of the diode were accounted for. Also the pulse energy is supposed to have an effect on the pulse width, so it was varied as well. The resulting curves were fitted to obtain their FWHM, which was then plotted against the output power for each wavelength and can be seen in figure 3.1.4. For all wavelengths the FWHM increases drastically for output powers above 1.0 mW, but all frequencies display the same behavior. For the measurements presented in section 4.3.1 three IRFs at 373.5 nm, 375.0 nm, and 376.5 nm were recorded (for their FWHM see table

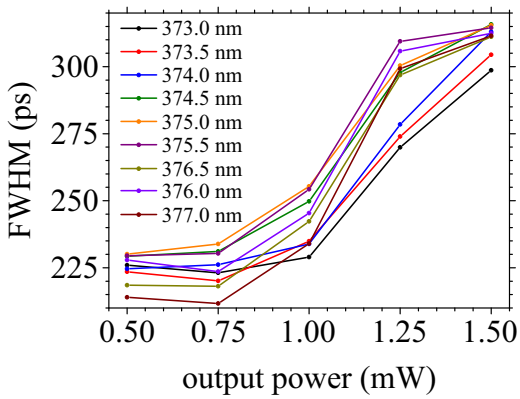

Figure 3.1.4: FWHM of the excitation pulse versus output power of the diode for wavelength between 373 nm and 377 nm.

wavelength (nm)	FWHM (ps)
373.5	220
375.0	243
376.5	218

Table 3.1.1: FWHM of the IRFs at 373.5 nm, 375.0 nm, and 376.5 nm.

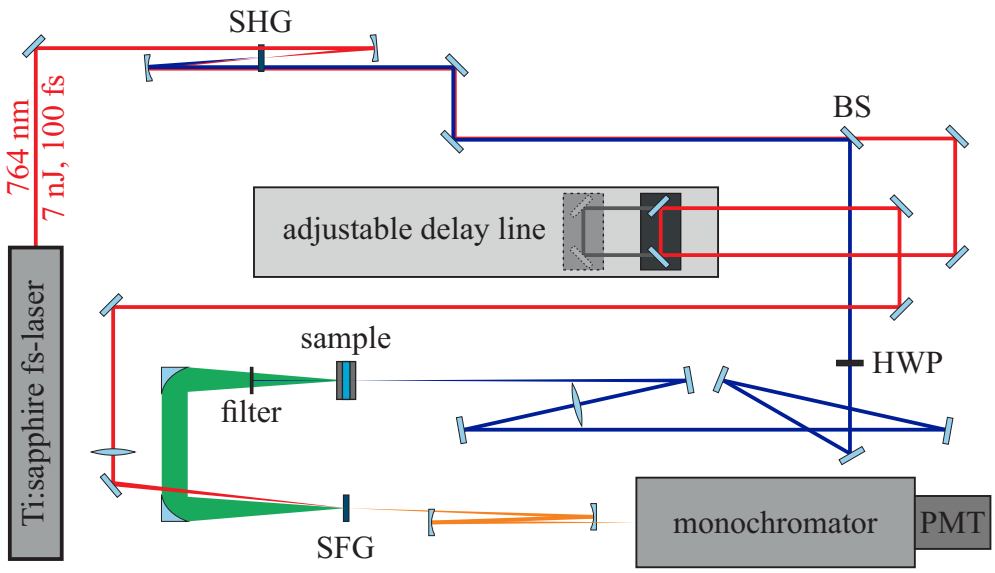

Figure 3.1.5: Experimental scheme of the fs fluorescence upconversion setup used to investigate fluorescence dynamics of PTC under excitation of 382 nm.

3.1.1). The central frequency of 375.0 nm showed a slightly higher FWHM in its IRF, however the response function was less noisy and had the highest count rates. For the data analysis all three IRFs were used in the evaluation and the results were compared. In all cases it was found that the IRF of the central frequency produced the best results and no significant deviations for the other IRFs was found. The data recording was performed directly after the sample was prepared, to exclude photodegradation. The quartz cuvette was put in the sample chamber of the TCSPC device and the count rates were adjusted with an iris before the monochromator, such that the counts on the detector were low enough to satisfy the condition that only for every 100th pulse a fluorescence photon is detected. The control software of the device also allowed for subsequent measurements at different wavelengths. Thereby, for every sample a region from 410 nm to 470 nm was scanned in 13 steps. This covers the major part of the fluorescence peak of PTC, as discussed in section 4.1. Since the output power of the excitation source is rather low and the whole measurement of one sample was done in less than 30 minutes, photodegradation can be excluded. However, it should be mentioned that especially for the glycerol sample a decrease in the count rates has been noticed. The acquired data sets were analyzed globally using a MATLAB script. The fitting routine includes several decay time constants, whose amplitudes are individual fit parameters for each wavelength trace. Also a convolution of the measured IRF with the assumed decay was performed to model the experimental data. Statistical error estimations for each parameter were derived from the determinant of the Jacobi matrix of the fit.

3.1.4 Femtosecond fluorescence upconversion

The upconversion measurements were performed with a FLUOMAX-SC spectrometer by IB Photonics Ltd., that was modified and optimized to increase performance [90]. The Ti:Sapphire fs-laser source is described in detail in section 3.2.1. To obtain an excitation wavelength of 382 nm the central wavelength of the laser was detuned from its optimum

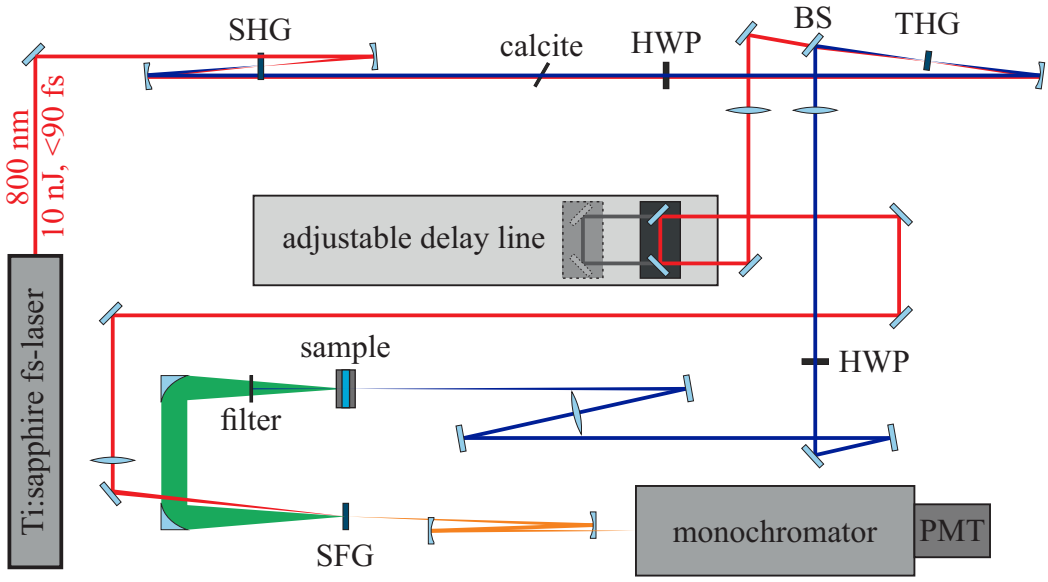

Figure 3.1.6: Experimental scheme of the fs fluorescence upconversion setup used to investigate fluorescence dynamics of PTC under excitation of 266 nm.

at 800 nm to 764 nm. At the corresponding settings, the laser produced pulses with approximately 7 nJ energy and 100 fs FWHM. The first step in the upconversion setup was the second harmonic generation of the input beam to obtain 382 nm for the excitation. The SHG and unconverted fundamental were split using a dichroic beamsplitter. The UV light was turned in polarization using a $\lambda/2$ wave plate to ensure magic-angle configuration [87, 88], redirected by a couple of mirrors to achieve temporal overlap with the fundamental later, and was then focused into the sample. After the sample, a long pass filter with a cut-on wavelength of 420 nm was used to block the excitation light. The fluorescence passes the filter and gets collimated by a parabolic mirror and focused by a second one into the SFG crystal. In the birefringent crystal the focused fundamental beam, which in the meantime had passed an adjustable delay line, is spatially overlapped with the fluorescence. The generated sum-frequency signal is collimated and focused into the double monochromator and in the end detected by a PMT. This whole setup is illustrated in figure 3.1.5. The pulse energy at the sample position with 382 nm excitation was approximately 0.4 nJ.

Also the third harmonic of the fundamental at 800 nm was used to investigate the fluorescence dynamics of PTC. In this setting the laser produced pulses with 10 nJ energy and sub 90 fs FWHM. For this excitation scheme, the generated SHG and remaining fundamental passed a calcite plate to adjust their temporal mismatch acquired in the BBO crystal for the SHG. After that, a half wave plate turned the polarization of both beams to be parallel. Subsequent focusing into a second BBO crystal that is optimized for third harmonic generation leads to 266 nm pulses. The collinear UV and NIR pulses are split using a dichroic mirror. The fundamental travels the same path as for the SHG excitation scheme after it has been collimated and rotated by a half wave plate to ensure magic-angle configuration. The UV pulses are also collimated and the SHG is filtered using a high reflective mirror for 400 nm. The THG is then set onto the same beam path as for the SHG excitation scheme. The pulse energy at the sample position for THG excitation

was approximately 60 pJ. The whole THG excitation scheme is illustrated in figure 3.1.6. The sample for the upconversion measurements were prepared according to section 3.1.1. Since the data acquisition takes several hours, a significant photodegeneration was noticed and constant exchange of PTC in the interaction volume was required. To this end, a peristaltic pump and a flow-through cuvette with 2 mm thickness was implemented to enable overnight measurements. The fluorescence peak was again scanned from 430 nm to 470 nm with nine steps. The fluorescence decay was scanned up to 2 ns for each wavelength and this cycle was repeated up to 75 times to increase the signal to noise. The acquired data sets were analyzed with the same MATLAB script as the TCSPC data, however the IRF was assumed to be Gaussian shaped and its FWHM was one of the fit parameters.

3.2 Pulse-shaping setup

This section will explain the instrumentation and setup for the pulse shaping experiments. First, the laser system used in these studies as well as the PTC experiments presented in chapter 4 will be explained and characterized in section 3.2.1. In section 3.2.2, the conversion of the fundamental transverse laser mode to a higher order Laguerre-Gaussian mode will be explained. The $4f$-pulseshaper arrangement, characteristics, and calibration will be presented in section 3.2.3. In the last part 3.2.4, all elements presented in the previous sections will be combined and the general concept of the whole setup will be outlined.

3.2.1 The laser system

This section will describe the laser system that is used for all studies involving femtosecond pulses, that are presented throughout this thesis. The instrument is a femtosecond oscillator MIRA® model B by COHERENT®, that is based on a titanium doped sapphire crystal Ti:Al_2O_3. The setup of the laser is illustrated in figure 3.2.1 according to [91]. The oscillator is pumped by a Nd:YAG solid state cw laser VERDI® V5 in the earlier segment of the thesis and was later replaced by a V6 version of the same series due to a damaged laser head. For the theory of laser operation and pulse generation via mode locking see

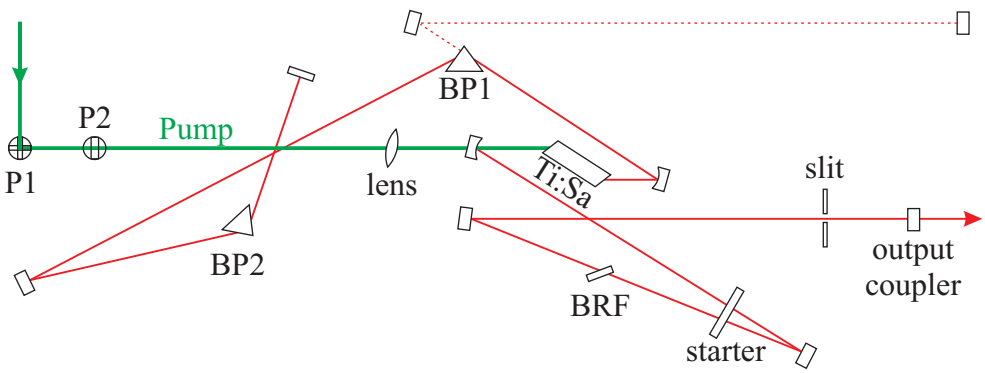

Figure 3.2.1: Setup of the pulsed Ti:Sa laser system MIRA® model B that is pumped by a VERDI® V5/V6, both by COHERENT®. According to [91].

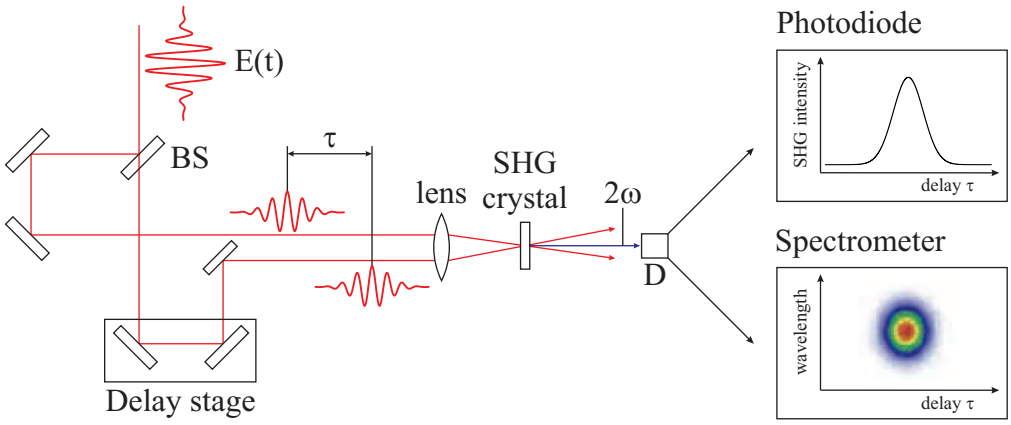

Figure 3.2.2: General setup of a non-collinear characterization scheme for femtosecond pulses. An interferometric setup splits the input beam in two parts by a beamsplitter BS, delays one of them variably, and focuses both into a BBO crystal. The generated SHG signal is detected either by a photodiode, which leads to an intensity autocorrelation (AC), or by a spectrometer, which generated a 2D intensity map, that is called frequency resolved optical gating (FROG) trace. [47]

references [43, 47, 50]. The pump beam is frequency doubled inside the laser head of the VERDI® to 532 nm and coupled into the laser cavity of the oscillator via two periscopes P1 and P2 to adjust height and polarization. The cavity of the MIRA® is divided into two parts, one that consists of the output coupler, the starter for passive modelocking, a birefrigent filter (BRF) for wavelength adjustment, two focusing mirrors and the laser crystal and one that houses a Brewster prism compressor for dispersion management. Without the prism BP1 an auxiliary cavity is formed for alignment purposes by the first part of the laser and two additional mirrors. Inserting the prism after prealignment allows for an easier to achieve modelocked operation and the length of the beampath inside the prisms BP1 and BP2 enabled dispersion compensation of all transmissive elements in the cavity, especially the laser crystal, to achieve near bandwidth limited pulses.
The characterization of the generated pulses was carried out by two well established schemes, namely intensity autocorrelation (AC)[92] and frequency resolved optical gating (FROG)[93]. The fundamental setup for both techniques is very similar and illustrated in figure 3.2.2. Both are based on an interferometric measurement of the pulses. The input beam, that is supposed to be characterized, is split into two beams, one of which has an adjustable beam path length by the use of a delay stage. In the non-collinear geometry depicted in figure 3.2.2, both beams are then focused into a BBO crystal with spatial overlap. The autocorrelation can also be performed collinear, but a disentanglement of different signal contributions has to be done and no further information is gained [47]. By changing the length of the second beam path an adjustable delay τ is introduced between both pulses. The generated SHG signal strength (for details about second harmonic generation see section 2.1.5) is therefore dependent on τ. Note that the signal is background free and that contributions from SHG of one of the two beams is geometrically displaced and only the cooperative signal from both pulses gets detected. The difference between AC and FROG arises from the used detector. For the autocorrelation a photodiode is used and only the overall intensity of the signal is detected as a function of τ, whereas FROG uses a spectrometer, therefore generates a spectrum in dependence on the delay,

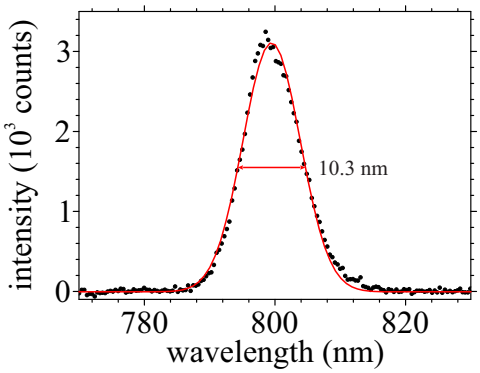

Figure 3.2.3: Typical MIRA spectrum (black dots) for operation at a central wavelength of 800 nm. A fit of the data with a Gaussian distribution (red line) yields a FWHM of $\Delta t = 10.3$ nm.

thus the data is a 2D intensity map.
Since the correlation of one pulse with itself is mathematically a convolution, the evaluation of the autocorrelation function is quite simple. Assuming a Gaussian input pulse with a temporal FWHM Δt, the convolution is also of Gaussian shape with a FWHM of $\sqrt{2} \cdot \Delta t$. The assumption of a Gaussian pulse is good for most applications, however for a completely arbitrary pulse it is impossible to retrieve the pulse shape and phase with just the autocorrelation function. Additional information has to be known, for example the spectrum of the pulse [47].
The spectral information is inherently included in the FROG trace, thus making it superior in terms of information that can be gained by one measurement. However, an analytic computation of the pulse shape is also not possible for FROG. A FROG trace basically poses a two-dimensional phase retrieval problem [94–96]. Therefore, it had been established to use adaptive algorithms to find the optimal retrieval [97–100]. After measuring a FROG trace the algorithm starts by guessing an arbitrary pulse and computes its FROG trace, which will then be compared to the measured one and a fitness of the guessed pulse will be calculated. This fitness is fed back into the loop for the generation of the next guessed pulse. After several iterations a maximum is found, however this is always a local one, not necessarily the global one. The algorithm can be improved to always yield results close to the global maximum. The remaining uncertainty and the more complicated analysis is a drawback of FROG over AC.
The instruments used for characterization are compact commercial adaptations of the above described techniques. Autocorrelations were measured using a PulseCheck USB 15 ShortPulse by APE and FROG traces came from a GRENOUILLE Model 8-50-ECO by Swamp Optics, which is explained in detail in [101]. Spectra were measured by an Ocean Optics USB2000+ CCD spectrometer and the pulse energy was derived from the laser power that was measured by a FieldMax II powermeter by COHERENT®. A typical laser spectrum is displayed in figure 3.2.3. The central frequency is 800 nm, which was adjusted by the BRF. The spectral FWHM of a Gaussian fit of the spectrum is 10.3 nm and the pulse energy is ≈ 10 nJ. The bandwidth limited pulse length of this spectrum according to equation 2.1.14 under the assumption of a Gaussian pulse shape is $\Delta t = 91$ fs. However, the real pulse length might be influenced by dispersion, especially originating from the output coupler. An autocorrelation measurement was performed and is displayed

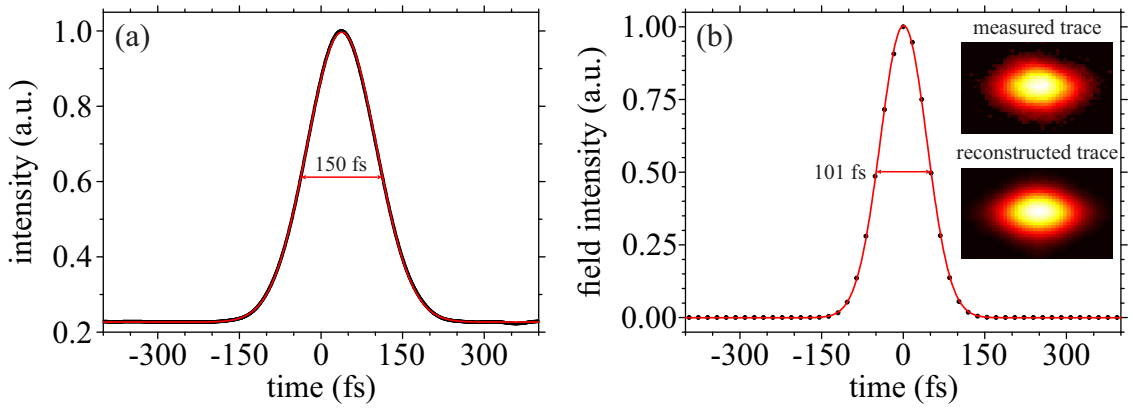

Figure 3.2.4: Characterization of the 800 nm pulses with (a) an autocorrelation shows a Gaussian pulse shape with a FWHM of $\Delta t_{AC} = 150$ fs. FROG traces were measured with a GRENOUILLE (b), the algorithm reconstructed the measured trace well (see insets) and a pulse FWHM of $\Delta t = 101$ fs was retrieved.

in figure 3.2.4a as black dots alongside a Gaussian fit marked as a red line. The fit yields a FWHM of the autocorrelation of 150 fs, assuming Gaussian shaped pulses results in a pulse FWHM of $\Delta t = 106$ fs. A characterization of the pulse by the GRENOUILLE yields a FROG trace illustrated in the upper inset of figure 3.2.4b. The reconstruction algorithm retrieved a matching trace displayed in the lower inset. The reconstructed temporal intensity of the pulse is shown in the main graph of figure 3.2.4b. A Gaussian fits results in a pulse FWHM of $\Delta t = 101$ fs. Both characterization methods yield similar results within the accuracy of such devices. However, both results do not match the computed bandwidth limited pulse of the spectrum. Some dispersion remains, which cannot only be attributed to the output coupler that has a 10 mm substrate of N-BK7. It should be noted at this point that spectra usually were recorded from the scattered beam for convenience and not by focusing into the fiber. Detection of the scattered light is dependent on the exact angle of incident between the scattering origin and optical fiber.
The experiments presented in section 4.3.2 were performed with the same laser system. For excitation with 266 nm the same laser configuration was used as discussed above. For 382 nm illumination of the sample the BRF of the laser was turned to approximately 760 nm. To achieve modelocked operation the second concave mirror encompassing the laser crystal was moved and adjusted in its angle. Pulses with energies of ≈ 7 nJ and a similar spectral FWHM were generated.

3.2.2 LG-mode conversion

The concept of Laguerre-Gaussian laser modes and their orbital angular momentum has been discussed in literature for the first time in 1992 [34]. In the same year, the first observation of optical phase singularities generated from a computer-generated hologram was reported [102]. Only two years later the first demonstration of such a mode can be found using a spiral phase plate (SPP) [103]. These optical elements introduce a spatial phase due to their staircase-like geometry and thus introduce a different optical path length for different parts of the spatial intensity distribution. It has been demonstrated that a number of discrete phase steps as low as eight produces a reasonably good LG

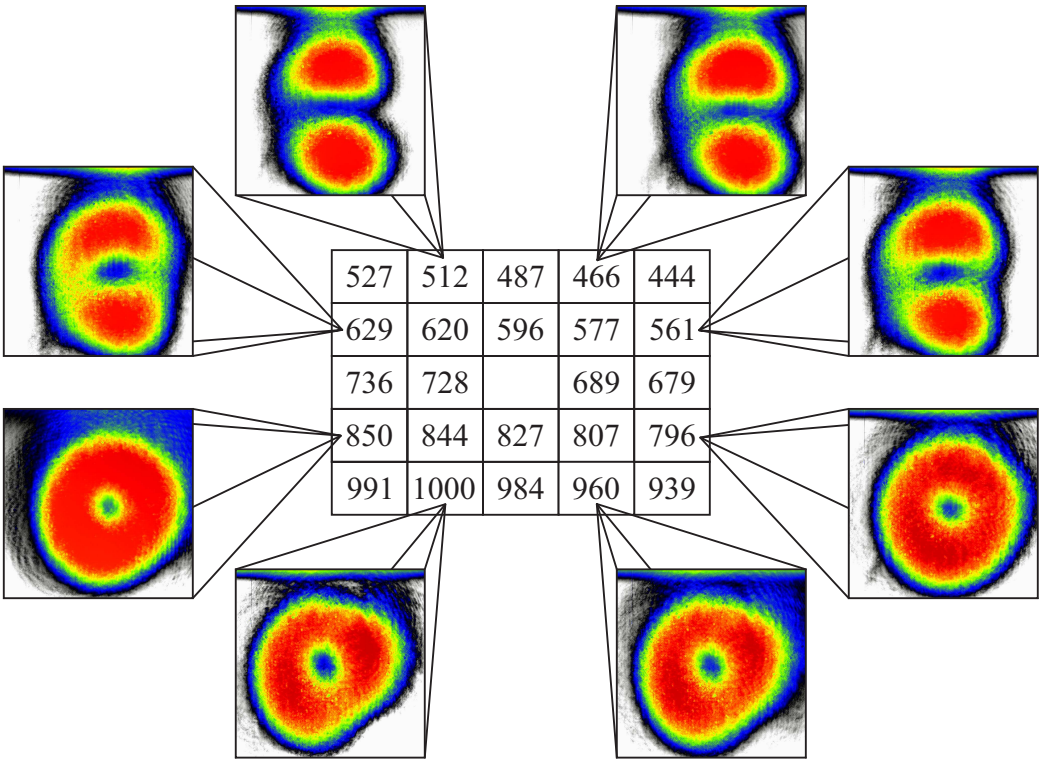

Figure 3.2.5: Sketch of the SPP array of the used VPP-1a phaseplate by RPC Photonics. The wavelength each square was optimized for is marked according to the manufacturer. The LG modes generated from some selected SPPs are indicated.

mode [104]. Both computer-generated holograms [105] and spiral phase plates [106] have been successfully applied to femtosecond pulses. For SPPs, pulse energies as high as 200 mJ were achieved for a 130 fs pulse [106], however this generation scheme was demonstrated not to be suitable for pulses shorter than 15 fs [107]. The issue originates from the concept of different optical path lengths for each spatial component, which is no longer applicable for broadband pulses. The dispersion of the material would result in different spectral components in different spatial parts of the beam, having the same spatial but a different spectral phase, thus the generation of a proper phase singularity is not possible. Eventually, broadband optical vortices in the NIR were reported using a mode converter involving a axial symmetric halfwave plate [108] and spiral gratings [109]. Also spatial light modulators (SLMs) were used in a $2f$ and $4f$ geometry to achieve shaping of the spatial properties of laser beams [110–112]. The advances in orbital angular momentum carrying beam have been reviewed in [113, 114].

Within this thesis the generation of fs-LG modes was achieved using a VPP-1a phase plate by RPC Photonics, which consists of a array of 25 elements including 24 SPPs optimized for wavelength ranging from 527 nm to 1000 nm that is depicted in figure 3.2.5 according to the manufacturer. From the figure, it is evident that the square with the number 20, when starting to count from the top left corner, should contain the SPP for 796 nm, which is the one most closely optimized for the used pulses. To check the alignment marker by the manufacturer the laser was used to generate optical vortices from the array elements 2, 4, 6, 8, 16, 20, 22, and 24, that are also illustrated in figure 3.2.5. The best result was obtained from square 20, which was then exclusively used for

the presented experiments. The detection of all laser modes in this thesis was performed with a TE/CCD-512TKBM/1/UVAR CCD camera by Roper Scientific, that consists of a 512x512 pixel array and was cooled to $-40\,^\circ$ to decrease the background noise. At this point, only the successful generation of a doughnut-shaped intensity profile is reported. The results of the beams' OAM determination via interference with a Gaussian beam will be presented in section 5.1.2.

3.2.3 The $4f$-pulseshaper

Manipulation of the temporal structure of the pulses was achieved with a $4f$-pulseshaper, that was build up from two blazed gratings with 1800 lines/mm, two cylindrical lenses with a focal length of 80 mm, two half-wave plates/polarizers, and a NIR-PHS spatial light modulator by Cambridge Research & Instrumentation with 128 individually controllable pixels [115]. The zero dispersion compressor was first constructed without the SLM and the wave plates, to guarantee the correct positioning of the gratings and lenses. This was checked with an autocorrelation measurement performed simultaneously as a feedback signal. The recorded autocorrelation curve for the best alignment of the ZDC is illustrated in figure 3.2.6 alongside a Gaussian fit with a FWHM of 134 fs. This results in a pulse length after the compressor of $\Delta t \approx 95$ fs, which is slightly lower than the reported pulse length of the laser system (see section 3.2.1). This might be connected to a slight deviation in the spectral width of the pulse from day to day or to a compression of the dispersion the pulse had acquired by passing several transmissive optical elements. The total transmission of the ZDC was $\approx 60\%$. However, the data suggests that an optimal alignment of the ZDC was achieved.
To complete the pulseshaper, the SLM was reinstalled and crossed polarizers were placed instead of the half-wave plates. The transmission axis of the first polarizer was oriented $45\,^\circ$ relative to the incoming polarization that is parallel to the laser table. This setup enables amplitude shaping of the spectrum, where the SLM is effectively used as a programmable half-wave plate with spectral resolution. It was also used for the calibration of the pulseshaper. The voltage of all pixels were increased in 4096 steps and the transmitted spectrum of the shaper was measured, this is illustrated in figure 3.2.7a. The data shows that for several voltages maximal and minimal transmission of the device can be

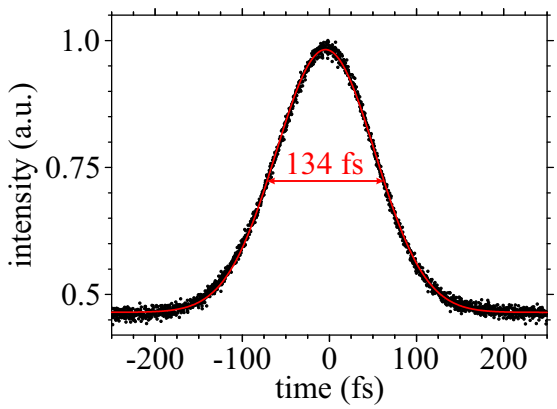

Figure 3.2.6: Autocorrelation of the pulse after an optimal alignment of the zero dispersion compressor was achieved. A Gaussian fit with a FWHM of 134 fs is noted as well.

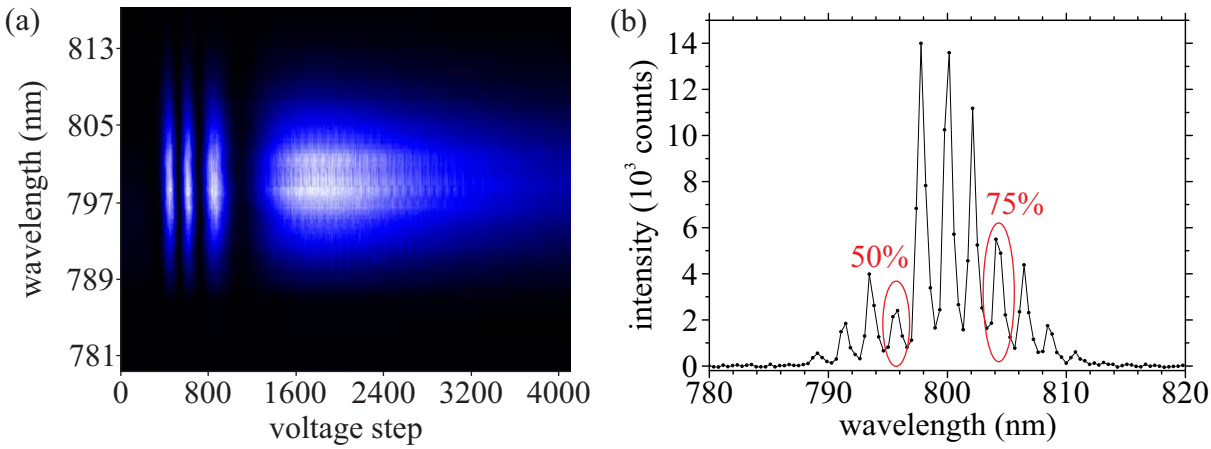

Figure 3.2.7: (a) Voltage calibration of the pulseshaper in amplitude shaping mode. The voltage of all pixels were increased in 4096 steps and the transmission spectrum was recorded. (b) Wavelength calibration spectrum. Every fourth pixel of the SLM is set to transmission and two indicated pixels are set to 50% and 75% transmission.

achieved. The wavelength calibration was done with the voltages 850 for maximum and 1090 for minimum transmission. The SLM was programmed in a way that every 4th pixel was set to transmission, whereas the three pixels in between were set to no transmission. This results in a change of the spectrum into a comb-like shape as it is illustrated in figure 3.2.7b. Fitting the peak positions allowed for the wavelength to pixel assignment. The direction of the wavelength axis on the display was established using two special pixels with a transmission of 50% and 75% (see figure 3.2.7b). The combined voltage and wavelength calibration was analyzed and phase calibrations curves for every pixel were derived. These phase curves were then used to calculate the voltages that had to be applied to the SLM to achieve a desired phase in the basis set of the Taylor coefficients introduced in section 2.1.2. The first test of the calibration was performed by trying to compress the pulse to be as short as possible. For this purpose the GRENOUILLE was

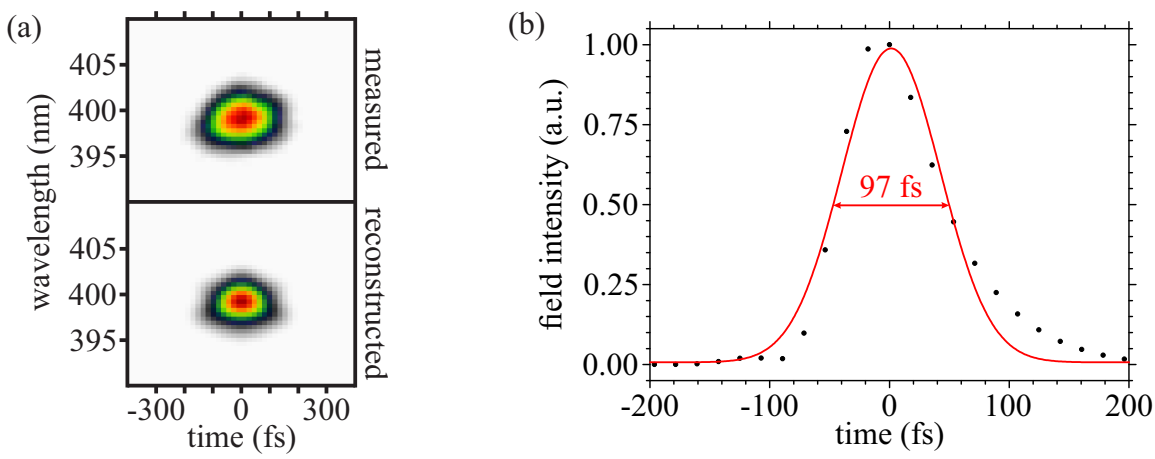

Figure 3.2.8: Measured and reconstructed FROG trace of the pulse with the applied compensation phase (a). Temporal profile of the retrieved pulse with a FWHM of $\Delta t \approx 97\,\mathrm{fs}$ (b).

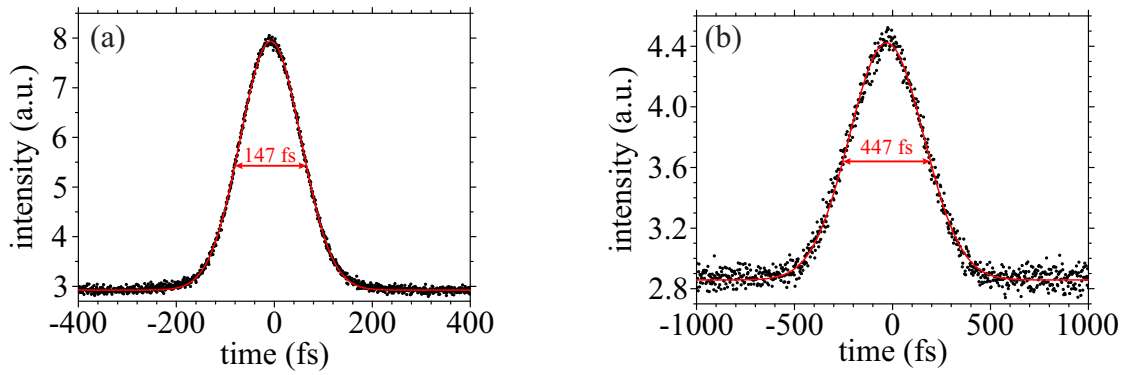

Figure 3.2.9: Autocorrelation of the compensated pulse and a Gaussian fit with a FWHM of 147 fs (a) and for an additional quadratic phase term of $b_2 = 10000\,\mathrm{fs}^2$ added to the compensation phase, alongside a Gaussian fit with a FWHM of 447 fs (b).

used as a feedback signal, since it is more sensitive to smaller pulse features. The FROG trace of the measured and retrieved compressed pulse are illustrated in figure 3.2.8a. The reconstructed temporal profile alongside a Gaussian fit is displayed in figure 3.2.8b. The compressed pulse has a FWHM of $\Delta t \approx 97\,\mathrm{fs}$ and the FROG trace shows only minor asymmetries and no higher order phase components. Thus, it can be assumed that the pulse was successfully compressed. To quantify the calibration a quadratic phase component was added to the compensation phase and the pulse length of the dispersed pulse was compared to the compressed pulse. To this end, the autocorrelation of the compressed pulse was measured and is displayed in figure 3.2.9a. The Gaussian fit revealed a pulse length of $\Delta t \approx 104\,\mathrm{fs}$. In the next step a quadratic phase term of $b_2 = 10000\,\mathrm{fs}^2$ was added to the compensation phase and the autocorrelation was measured again. The result is illustrated in figure 3.2.9b, where a significantly longer pulse is depicted. The Gaussian fit of the data revealed a pulse with a duration of $\Delta t \approx 316\,\mathrm{fs}$. From equation 2.1.16 it can be calculated that an input pulse of $\Delta t_{in} = 100\,\mathrm{fs}$, that acquires a quadratic spectral phase of $b_2 = 10000\,\mathrm{fs}^2$, is dispersed to a FWHM of $\Delta t_{out} = 295\,\mathrm{fs}$. The measurement is consistent with this result, therefore it can be assumed that the calibration is quantitatively working well. More details about the pulseshaper and a comprehensive instruction on its alignment can be found in [115].

3.2.4 The combined setup

The experiments presented in chapter 5 were performed using the whole or parts of an interferometer-like setup that is depicted in figure 3.2.10. The output of the laser is spatially cleaned by a telescope consisting of a lens with a focal length of $f = 150\,\mathrm{mm}$, that focuses the beam through a pinhole with a diameter of $100\,\mu\mathrm{m}$ before it is recollimated by a second lens with a focal length of $f = 50\,\mathrm{mm}$, the total transmission was $\approx 70\%$. All lenses used in the setup are made of NBK-7 glass. The beamprofile after the telescope is perfectly round, without any residual fluorescence or stray light from the oscillator. A periscope then changes the beam height to match the desired height over the breadboard the setup is build on. The wave vector of the beam is inverted after the element and two subsequent mirrors allow for incoupling of the beam into the setup via two irises. Two beamsplitters BS1 and BS2 create two of the three beam paths and the third was

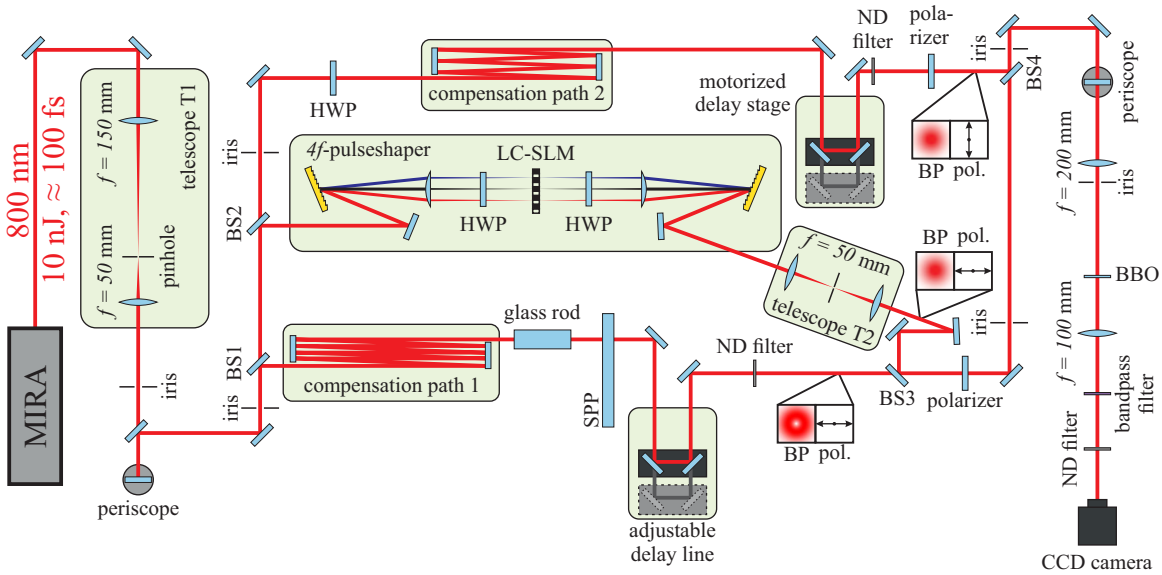

Figure 3.2.10: Combined setup for fs-LG spatial pulse shaping. In the interferometer-like setup the output of the soucre is split into three beams via beamsplitters (BS). The first beam is mode converted by an SPP and its delay is adjusted. The second beam contains the $4f$-pulseshaper and the third acts as the gate beam with a computer-controllable delay for the subsequent type II SHG process. The beam profiles (BP) and polarizations of each path are indicated at the end of the path.

constructed from the residual beam.
The first path contains a compensation path, which elongates the arm to match the length of the second path. A subsequent glass rod, that is made of SF-66 heavy flint glass and is 74.5 mm long introduces a dispersion of $b_2 \approx 20000\,\mathrm{fs}^2$ into the pulse. This is needed for the experiments presented in section 5.3. For all other experiments the glass rod was left out of the setup. The HG_{00} laser mode is then converted into a LG_{01} by means of the spiral phase plate (SPP), for further detail see section 3.2.2. After an adjustable delay stage for fine tuning of the path length, a reflective neutral density (ND) filter is used to attenuate the beams intensity to match the one in the second arm of the interferometer-like setup.
The $4f$-pulseshaper, that is described in detail in section 3.2.3, is the main component of the second beam path. The polarizers inserted instead of the half-wave plates (HWP) were only used for calibration. In all experiments presented in chapter 5 the wave plates were used, thus allowing phase shaping of the pulses. A subsequent telescope T2 with a total transmission of $\approx 50\%$, consisting of two lenses with a focal length of $f = 50\,\mathrm{mm}$ and pinhole with a diameter of $300\,\mu\mathrm{m}$, ensures a Gaussian beamprofile. The polarization of the shaped HG and LG pulses is parallel to the laser table and is ensured to be exactly the same by a VISIR-CW02 polarizer by CODIXX AG after the recombining beamsplitter. Both beams are spatially aligned to be collinear by two irises.
The third beam path consists of a half wave plate to turn the polarization axis, a compensation path to match the overall path length, and a delay stage motorized by a T-NA08A50 linear actuator by Zaber Technologies Inc., that allows for scanning the delay of the third pulse relative to the first two. A ND filter attenuates the beam intensity and a polarizer fixes the polarization to be orthogonal to the first two beams. The intensity profile re-

mains Gaussian in the third arm, that acts a gate in the following type II SHG step. The gate pulse is aligned collinear to the first two beams via two irises.
All three combined beams are adjusted in height by a periscope, that does not change the direction of the wave vector. A lens with a focal length of $f = 200\,\mathrm{mm}$ focuses the pulses into a BBO crystal and a second lens with $f = 100\,\mathrm{mm}$ recollimates the beam. A subsequent bandpass filter with a central frequency of 400 nm and a FWHM of 40 nm was inserted for detection of UV light and a ND filter was used to attenuate the beams to levels that do not damage the CCD camera. SHG singals were generated using either a 1 mm type I BBO cut under $\theta = 29.2\,^\circ$ for the experiments shown in section 5.1.2 or a 0.2 mm type II BBO cut under $\theta = 42.4\,^\circ$ for experiments shown in section 5.1.3 and 5.3. The spatial overlap at the BBO position was ensured by replacing the crystal with a pinhole with a diameter of $150\,\mu\mathrm{m}$ and optimizing the power throughput of all three beams independently. The temporal overlap was adjusted with the type II BBO in place, by maximizing the SHG signal on the cameras CCD chip. Arm one and two were aligned by moving the polarizer behind BS3 in front of the beam splitter and by inserting a HWP and polarizer in the second beam path to ensure orthogonal polarizations of the two beams. The path of the gate pulse was adjusted relative to the second arm of the interferometer-like setup in the original configurations, since both already had orthogonal polarization.
The studies presented in section 5.2 used a slightly modified setup. Only the second beam path used and no focusing or birefringent optics were placed in front of the CCD camera. The SPP was moved behind beam splitter BS3 so that it was possible to investigate whether the temporal shaping of the pulse had any impact on the mode conversion or vice versa. Also the characterization techniques for fs-laser pulses were tested with LG laser modes.

CHAPTER 4

FLUORESCENCE STUDIES OF PTC

In this chapter, the steady state and time-resolved fluorescence studies of PTC in methanol, ethanol, ethylene glycol, and glycerol will be presented. The employed setups and the sample generation are reviewed in section 3.1. The majority of the results of this chapter has been published in [1], alongside transient absorption measurements, that will not be covered in this thesis. The chapter is organized as follows: first, an overview of the static absorption and emission characteristics of PTC and the associated substances will be given in section 4.1, followed by the results of the quantum yield measurements of PTC in methanol, ethanol, and ethylene glycol in section 4.2. In glycerol, the determination was prevented by the formation of TPF. Section 4.3 is focused on the time-resolved results and is split into the dynamics on the picosecond time scale that are observed using TC-SPC and the femtosecond dynamics investigated via fs fluorescence upconversion. Lastly, section 4.4 will provide and interpretation and discussion of the results presented in the first three sections.

4.1 Static absorption and fluorescence spectra

This section will give an overview of the static absorption and emission spectra of the compounds involved in this study. As already presented in section 3.1.1 the investigated PTC is acquired through a photoreaction of TTC, which could have TPF as a byproduct as well. It has already been noted in literature that PTC is one of the few tetrazolium compounds that exhibit fluorescence and that it can be formed through a photoreaction of TTC [31][116][117]. However, it is at this point not clear why PTC does partially relax radiatively while TTC does only non-radiatively. The only structural difference between both compounds are the locked phenyl rings in PTC, which may rotate in TTC. This subunit of the molecule is called benco[c]cinnoline (BCC) and is also formed upon PTC reduction [116]. In TTC both phenyl rings can freely rotate in solution [76] and are also found to be twisted in the crystal structure [118][119]. This could hint towards a link between the emission characteristics of PTC and BC. The normalized absorption spectra are illustrated in figure 4.1.1 for PTC (solid), TTC (dashed), and BCC (dotted), all measured in ethanol. Through the photoreaction the main absorption peak of TTC at

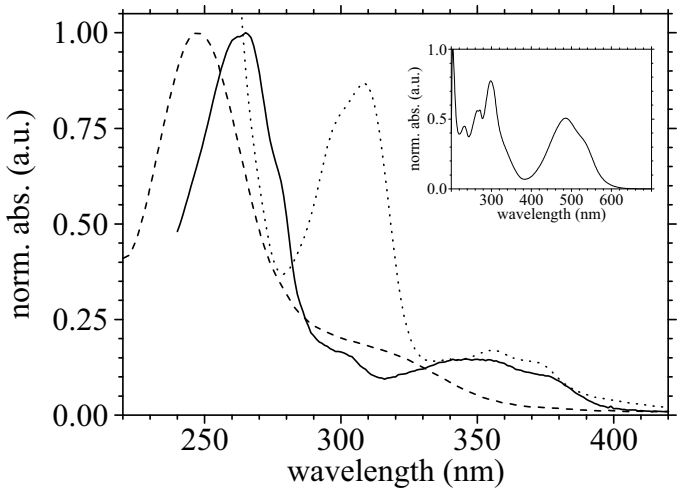

Figure 4.1.1: Normalized absorption spectra of TTC (dashed), accumulated PTC (solid), and BCC (dotted) in ethanol. The BCC spectrum is amplified by a factor of four for comparison. The inset shown the absorption spectrum of TPF in ethanol. Adapted from ref. [1].

247 nm shifts to 265 nm, the main peak for PTC. The progress of the sample preparation has been monitored via the rise of the latter peak (see section 3.1.1). Also note that for PTC a separated absorption band centered at 350 nm appears, whereas TTC only exhibits a shoulder towards this region. The absorption spectrum of BCC shown in figure 4.1.1 is scaled by a factor of four. The similarity between the aforementioned absorption band of PTC and a similar band of BCC becomes more striking by the scaling. The inset shows the absorption spectrum of TPF, which might be formed as a byproduct due to impurities of the solvents. A large absorption band at around 500 nm is present, that could interfere with the fluorescence of PTC, as can be seen from figure 4.1.2a. Here the normalized fluorescence spectra are depicted for PTC under excitation of 266 nm (solid) and 350 nm (dashed). The only difference between both excitation wavelength is the presence of a small double peak feature at 343 nm / 358 nm for deeper UV excitation. This points towards contributions from higher lying orbitals than the S_1. For comparison,

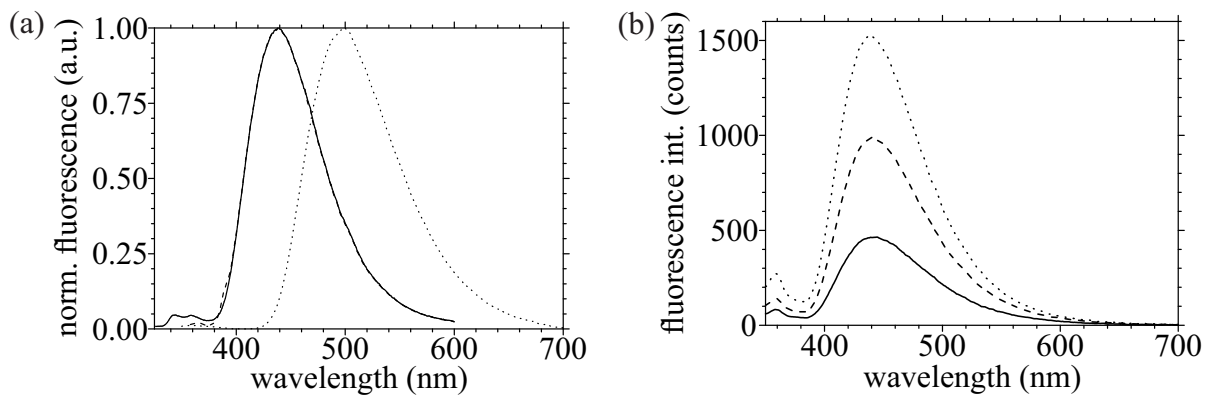

Figure 4.1.2: (a) Normalized fluorescence spectra for PTC in ethanol for excitation at 267 nm (solid) and 350 nm (dashed) and BCC (dotted) in ethanol for 252 nm excitation. Taken from ref. [1]. (b) Absolute fluorescence intensity of a sample of initially only TTC in ethanol for three consecutive measurements of the same sample.

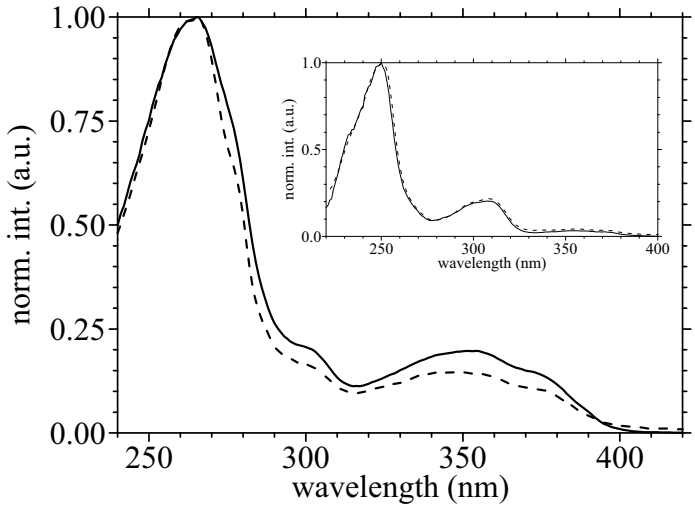

Figure 4.1.3: Normalized spectra of absorption (dashed) and excitation (solid) for an emission at 439 nm of PTC in ethanol. The inset shows the normalized absorption and emission spectrum of BCC for an emission at 490 nm.

also the emission spectrum of BCC under excitation of 252 nm is displayed. Apart from the maximum being at around 500 nm the structure of the fluorescence peak is remarkably similar to PTC, although it should be noted that the absolute intensity of the emission of BCC is much weaker than for PTC. This is supported by the reported quantum yield of BCC of only 2% [120]. It should also be noted that an emission spectrum of TTC can be recorded, however it is found that the intensity of the emission increases after subsequent measurements of the same sample. This is illustrated in figure 4.1.2b, where TTC in ethanol was measured three times. Each previous measurement increased the signal strength by approximately the same amount. This can be attributed to a formation of PTC in the sample due to the excitation light. The almost identical emission spectra of PTC under excitation with 266 nm and 350 nm (figure 4.1.2a) imply that the emission is independent of the electronic state that is excited through the absorption. To further corroborate this argument the excitation spectrum of PTC in ethanol for emission at 439 nm is displayed in figure 4.1.3 (solid) alongside the normalized absorption spectrum (dashed). Both spectra match sufficiently well over the whole measured region. This further confirms that there is only one radiating relaxation path in PTC. Note that this behavior is very similar in BCC as can be seen in the inset of figure 4.1.3. The excitation spectrum (solid) also follows the absorption spectrum (dashed) over the whole measured wavelength region. Therefore, it can be assumed that also in BCC only one radiating species is present.

4.2 Quantum yield measurements

The determination of the quantum yields of PTC in methanol, ethanol, ethylene glycol, and glycerol was performed according to section 3.1.2. First the results for harmane in H_2SO_4 and anthracene in ethanol under excitation with 365 nm and 340 nm, respectively, have been analyzed. The emission of harmane is a broad, structureless feature with a peak at 433 nm, similar in shape as what was reproted for PTC in section 4.1. The fluorescence

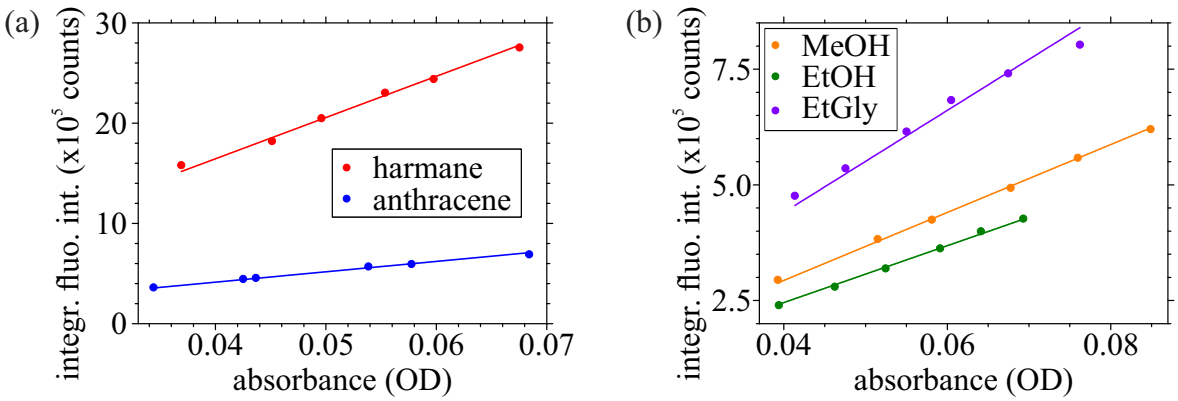

Figure 4.2.1: (a) Integrated fluorescence intensity versus absorbance for the reference substances harmane in H_2SO_4 (red) and anthracene in ethanol (blue) under excitation of 365 nm and 340 nm, respectively. (b) Integrated fluorescence intensity versus absorbance for PTC in methanol (orange), ethanol (green), and ethylene glycol (purple) for excitation with 375 nm. Adapted from ref. [1].

of harmane was integrated from 384 nm to 600 nm. The emission of anthracene is a red-shifted and mirrored version of its absorption spectrum with several peaks at 378 nm, 399 nm, 423 nm, and 448 nm. The fluorescence was integrated from 350 nm to 700 nm. The integrated fluorescence intensities were plotted against the absorbance at the excitation wavelength for six samples with different substance concentration in figure 4.2.1a. In addition, a linear regression with an intercept of zero was performed for each data set and included in the plot. Note that the slope for harmane and anthracene differs greatly, as is expected from their different quantum yields. Using equation 3.1.2 for deriving the yields for each substance, while the other is treated as the reference, results in a quantum yield of 81% for harmane and 27% for anthracene. Both values match the reported one exactly for the respective molecules [83][84]. Therefore, the chosen method, instrument settings, and instrument calibrations seem to be suited for quantum yield determination. Solutions of PTC in methanol, ethanol, ethylene glycol, and glycerol have been prepared. However, it was observed that the glycerol samples turn pale red during the irradiation with UV light for the PTC generation. This is attributed to the formation of TPF impurities. However, this interferes with the quantum yield determination, since TPF absorbs the emission of PTC, as can be seen from figures 4.1.1 and 4.1.2. For the other solvents the measured data sets followed the expected linear model well, as can be seen from figure 4.2.1b. The quantum yields for methanol, ethanol, and ethylene glycol are (18.2 ± 0.3)%, (16.0 ± 0.2)%, and (31.6 ± 0.6)%, respectively. The quantum yields together with the fluorescence lifetimes presented in the next section will enable an estimation of the radiative and non-radiative rates. Setting these into relation to solvent parameters like viscosity η or polarity will provide further insight into the nature of the processes. At this point, only a dependence of the non-radiating relaxation pathway on the solvent can be assumed, which would imply some sort of molecular motion or twist in the non-radiative relaxation. These motions could be hindered or supported in different solvents, thus having an impact on the competing relaxation path, which is fluorescence in this case. These findings will be discussed together with the time resolved results in section 4.4.

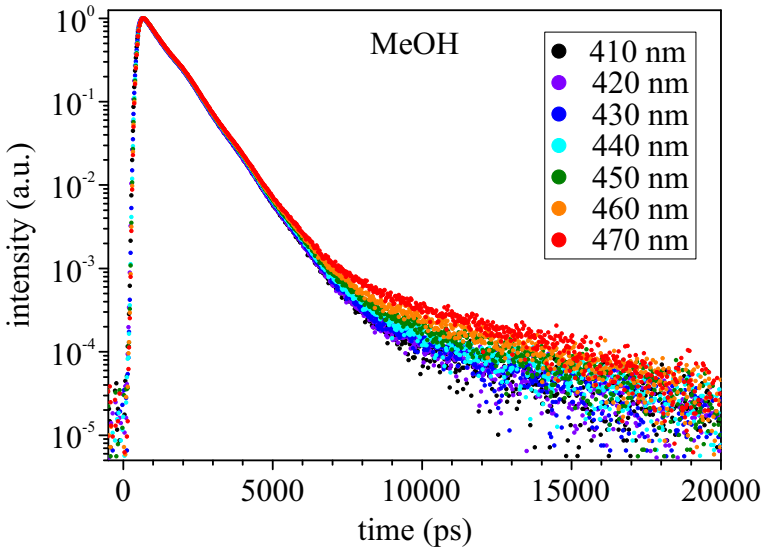

Figure 4.3.1: TCSPC results for PTC in methanol for emission wavelength between 410 nm and 470 nm under 375 nm excitation.

4.3 Time resolved fluorescence measurements

The time resolved emission characteristics of PTC was investigated on the picosecond time scale for different solvents using TCSPC and on the femtosecond time scale for one solvent using fluorescence upconversion. The details of how these experiments were performed can be found in section 3.1.3. The analysis of the recoded data was done with a Matlab script involving a fit model in the form of equation 2.3.2. In the following the results for both time scales will be presented separately and discussed in the context of the other results in section 4.4.

4.3.1 picosecond-dynamics

The TCSPC data were recorded according to section 3.1.3. The emission of PTC was scanned from 410 nm to 470 nm in 10 nm steps for each solvent. The magic angle configuration was ensured by the polarizer in front of the monochromator. Figure 4.3.1 displays

Table 4.3.1: Results of the global analysis of the TCSPC data of PTC in methanol for the time constants τ_0, τ_1, τ_2, and their respective amplitudes A_i. For methanol a biexponential model was sufficient to describe the data.

wavelength [nm]	τ_0 [ns]	A_0	τ_1 [ps]	A_1	τ_2 [ps]	A_2
410		0.000		1.000		-
420		0.000		1.000		–
430		0.000		1.000		–
440	3.0 ± 2.0	0.000	808 ± 1	1.000	-	–
450		0.001		0.999		–
460		0.002		0.998		–
470		0.003		0.997		–

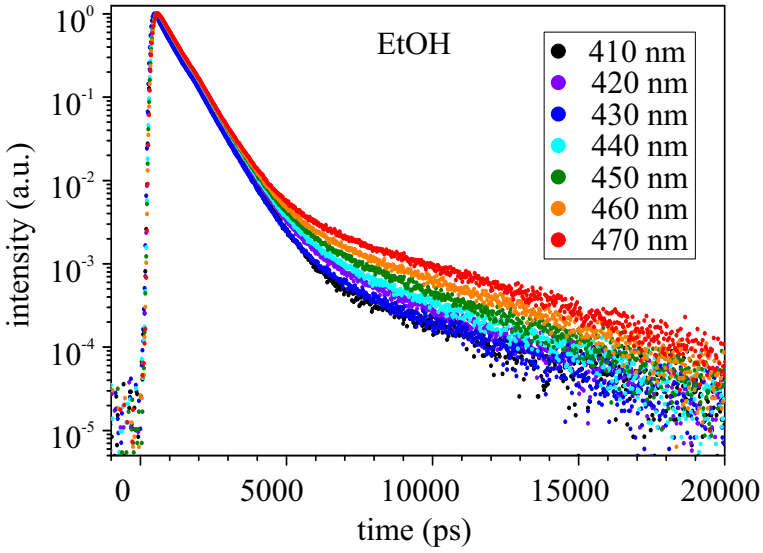

Figure 4.3.2: TCSPC results for PTC in ethanol for emission wavelength between 410 nm and 470 nm under 375 nm excitation. Adapted from ref. [1].

the background subtracted results for PTC in methanol. Note that the intensity-scale is logarithmic, in this representation a monoexponential decay looks linear. The decay in methanol is mainly monoexponential, however a slight tail towards longer time scales is observed especially for longer emission wavelengths. Therefore, a biexponential model was used for the global analysis. The time constants for the decay and the amplitudes for each wavelength are listed in table 4.3.1. The major contribution is $\tau_1 = (808 \pm 1)$ ps, which has an amplitude of over 99% for all emission wavelengths. A longer time constant of $\tau_0 = (3.0 \pm 2.0)$ ns is also observed, which describes the aforementioned tail. Its amplitude is well under 1% even for the most red shifted emission wavelength. Also note that the error is very large at 67%, due to the low amplitude. The emission characteristics of PTC in ethanol changes slightly compared to methanol, which is expected due to their quantum yields also differing a little (compare section 4.2). The data for ethanol is visualized in figure 4.3.2, where it becomes apparent that the tail towards longer times becomes bigger in amplitude but similar in time scale. This can also be extracted from the results of the global analysis in table 4.3.2. The main emission feature has a time

Table 4.3.2: Results of the global analysis of the TCSPC data of PTC in ethanol for the time constants τ_0, τ_1, τ_2, and their respective amplitudes A_i. For ethanol a biexponential model was sufficient to describe the data.

wavelength [nm]	τ_0 [ns]	A_0	τ_1 [ps]	A_1	τ_2 [ps]	A_2
410		0.002		0.998		-
420		0.004		0.996		–
430		0.004		0.996		–
440	3.2 ± 0.3	0.005	671 ± 1	0.995	-	–
450		0.007		0.993		–
460		0.009		0.991		–
470		0.011		0.989		–

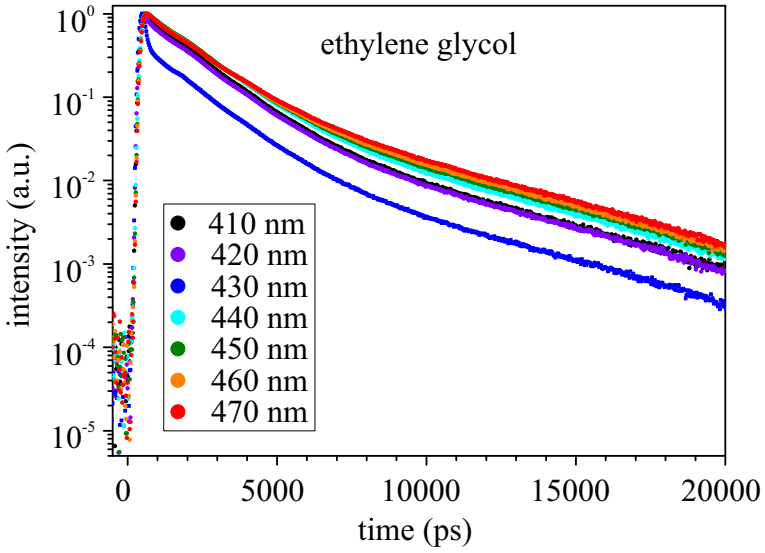

Figure 4.3.3: TCSPC results for PTC in ethylene glycol for emission wavelength between 410 nm and 470 nm under 375 nm excitation.

constant of $\tau_1 = (671 \pm 1)$ ps, which is faster than in methanol, which is expected due to the lower quantum yield. The amplitude for the longer emission with $\tau_0 = (3.2 \pm 0.3)$ ps rises to about 1% for 470 nm in ethanol. Note that the statistical error of the global analysis is now much lower for τ_0. For ethylene glycol even longer emission time constants are expected, due to the greatly increased quantum yield. Indeed, a significant difference in the fluorescence dynamics can be seen from figure 4.3.3. First note that the emission wavelength 430 nm displays the fast dynamics of the Raman peak, which is calculated to be at 429 nm. This inelastic scattering is accounted for in the global analysis by adding the IRF to the model, since inelastic, much like elastic scattering, is instant on the time scales of the TCSPC. Overall, the decay in ethylene glycol is much longer compared to methanol and ethanol. However, one more time constant is necessary to model the decay. The results of the global analysis are found in table 4.3.3. Note that τ_0 increases to (3.93 ± 0.07) ns and has a much higher amplitude of up to 10% for the longest emission wavelength. The main emission however, is much longer with $\tau_1 = (1360 \pm 10)$ ps compared to methanol and ethanol. Additionally, a short time constant of $(\tau_2 = 125 \pm 5)$ ps

Table 4.3.3: Results of the global analysis of the TCSPC data of PTC in ethylene glycol for the time constants τ_0, τ_1, τ_2, and their respective amplitudes A_i. For ethylene glycol a triexponential model was sufficient to describe the data.

wavelength [nm]	τ_0 [ns]	A_0	τ_1 [ps]	A_1	τ_2 [ps]	A_2
410		0.061		0.625		0.314
420		0.079		0.838		0.083
430		0.076		0.743		0.181
440	3.93 ± 0.07	0.090	1360 ± 10	0.782	125 ± 5	0.128
450		0.099		0.721		0.180
460		0.102		0.582		0.316
470		0.104		0.548		0.348

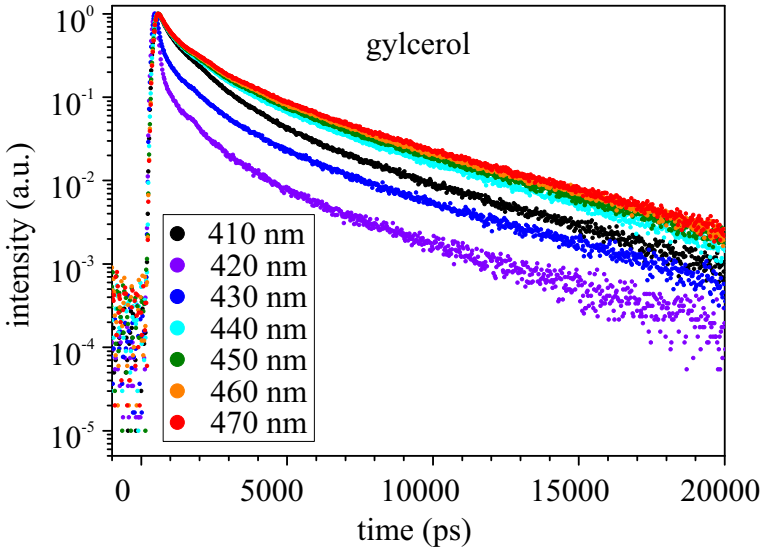

Figure 4.3.4: TCSPC results for PTC in glycerol for emission wavelength between 410 nm and 470 nm under 375 nm excitation.

appears with a fairly large amplitude. However, A_2 does not seem to vary consistently with the emission wavelength. Also note that the IRF of the system is approximately 220 ps, thus τ_2 might represent a faster dynamic, that is simply not correctly resolved due to the limited time resolution of the system. The dynamics in glycerol are somewhat similar, but not identical to ethylene glycol. The quantum yield in glycerol is expected to be a bit larger than in ethylene glycol, however due to formation of TPF it was not possible to measure it. The TCSPC results, illustrated in figure 4.3.4, show that the main emission with $\tau_1 = (1030 \pm 20)$ ps is faster than in ethylene glycol, however not as fast as in the monoalcohols. The long emission constant of $\tau_0 = (3.94 \pm 0.04)$ ps is almost identical to the one in ethylene glycol, but has slightly larger amplitude, for the longest emission wavelength it reaches 15%. However, a third time constant of $\tau_2 = (204 \pm 4)$ ps emerges from the analysis as well. It is longer compared to ethylene glycol and in the same range as the IRF of the instrument. Therefore, it has a much higher significance than in the case of ethylene glycol. Its amplitude is around $50\% - 55\%$ except for the emission wavelength 420 nm and 430 nm, which also happen to be the one most affected

Table 4.3.4: Results of the global analysis of the TCSPC data of PTC in glycerol for the time constants τ_0, τ_1, τ_2, and their respective amplitudes A_i. For glycerol a triexponential model was sufficient to describe the data.

wavelength [nm]	τ_0 [ns]	A_0	τ_1 [ps]	A_1	τ_2 [ps]	A_2
410		0.058		0.388		0.554
420		0.058		0.298		0.647
430		0.077		0.340		0.583
440	3.94 ± 0.04	0.109	1030 ± 20	0.357	204 ± 4	0.534
450		0.125		0.351		0.524
460		0.138		0.344		0.518
470		0.149		0.335		0.516

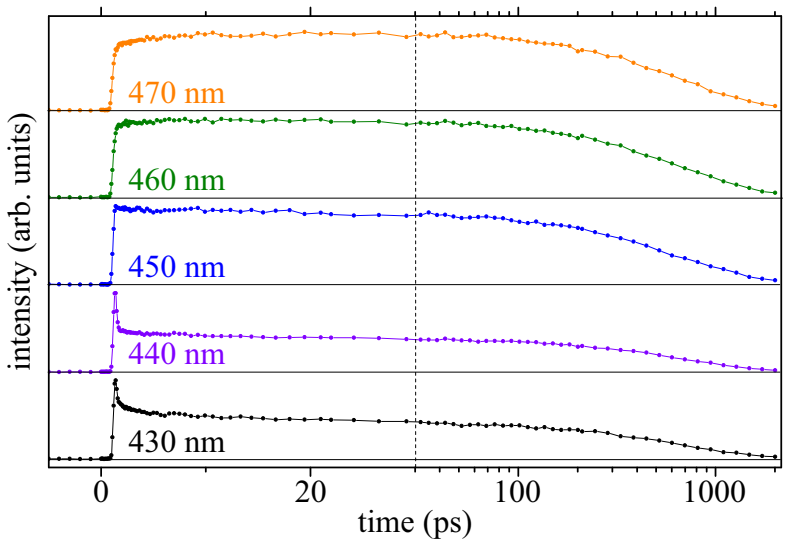

Figure 4.3.5: Femtosecond upconversion results for PTC in ethanol for emission wavelength from 430 nm to 470 nm at an excitation wavelength of 380 nm. The scale changes from linear to logarithmic at 30 ps (dashed vertical line). Adapted from ref. [1].

by the Raman scattering. Although inelastic scattering was included in the analysis of the glycerol data as well, the deviation of the amplitudes of τ_2 for 420 nm and 430 nm might be attributed to it. The overview of the results of the global analysis for PTC in glycerol is given in table 4.3.4.

4.3.2 femtosecond-dynamics

To unravel dynamics on the femtosecond time scale, that cannot be investigated with TCSPC, fs fluorescence upconversion experiments have been performed on PTC in ethanol. Details on the setup and how the measurements were performed can be found in section 3.1.4. Also note that the setup unambiguously gives excess to excitation of different electronic states by either irradiating the sample with the second or third harmonic of the fundamental. Although for PTC in ethanol the TCSPC results do not disclose dynamics on the order of hundreds of picoseconds, faster dynamics on the scale of a few pico- down to several hundred femtoseconds could be present due to solvation and cooling effects. Time traces of the fluorescence evolution have been taken for several wavelengths across

Table 4.3.5: Results of the triexponential global analysis of the upconversion data of PTC in ethanol for the time constants τ_1, τ_2, τ_3, and their respective amplitudes A_i under 380 nm excitation.

wavelength [nm]	τ_1 [ps]	A_1	τ_2 [ps]	A_2	τ_3 [ps]	A_3
430		0.318		0.119		0.563
440		0.483		0.080		0.437
450	680 ± 10	0.869	9 ± 1	0.025	0.21 ± 0.04	0.106
460		1.960		−0.159		−0.801
470		1.987		−0.359		−0.628

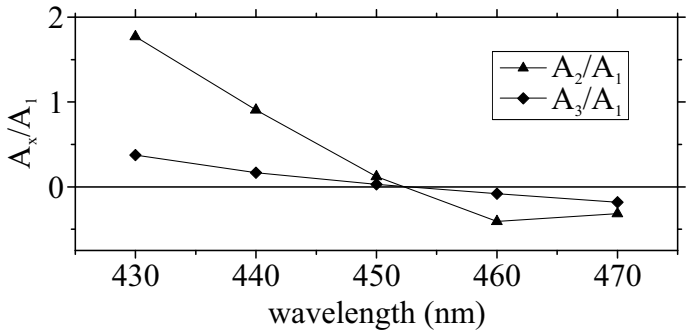

Figure 4.3.6: Evolution of the amplitudes from the global analysis of the decays τ_2 (triangles) and τ_3 (diamonds) relative to the slowest constant τ_1 as a function of emission wavelength for an excitation with 380 nm. Adapted from ref. [1].

the fluorescence peak of PTC. However, it should be noted that the used edge-pass filter restricted the detection to wavelengths above 425 nm. Excitation in the red edge of the S_1 absorption feature of PTC (see figure 4.1.1) with 380 nm led to the traces depicted in figure 4.3.5. The first 2 ps of the PTC fluorescence are shown for emission wavelengths ranging from 430 nm to 470 nm. Note that the time axis changes from linear to logarithmic at 30 ps indicated by the dashed vertical line. In the data a dominant Raman peak (located at $\approx$ 437 nm) can be seen for a fluorescence wavelength of 430 nm and 440 nm. Its temporal profile follows the cross correlation of the involved pulses, which are mainly responsible for the system IRF. This is included in the fit model in the same way as for the TCSPC measurements. Apart from the Raman peak, the more interesting ultrafast dynamics of the vibrational cooling can be observed from the traces of the red edge emission. A global fit was performed using a triexponential function. The fit parameters are listed in table 4.3.5. The slowest time constant $\tau_1 = (680 \pm 10)$ ps matches well with the time constant τ_1 from the analysis of the TCSPC data in ethanol (see section 4.3.1). How-

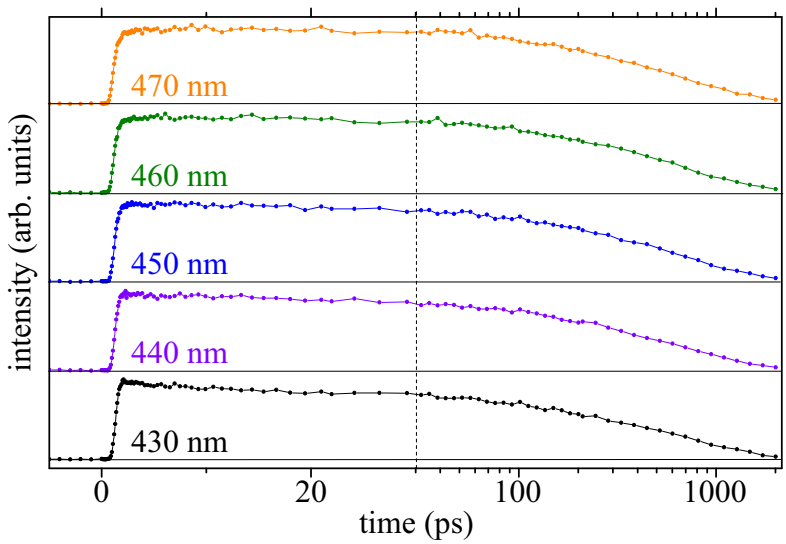

Figure 4.3.7: Femtosecond upconversion results for PTC in ethanol for emission wavelength from 430 nm to 470 nm at an excitation wavelength of 266 nm. The scale changes from linear to logarithmic at 30 ps (dashed vertical line). Adapted from ref. [1].

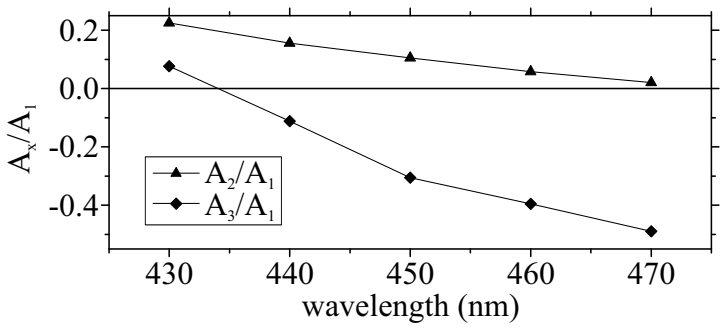

Figure 4.3.8: Evolution of the amplitudes from the global analysis of the decays τ_2 (triangles) and τ_3 (diamonds) relative to the slowest constant τ_1 as a function of emission wavelength for an excitation with 266 nm. Adapted from ref. [1].

ever, two additional ultrafast time constants of $\tau_2 = (9 \pm 1)$ ps and $\tau_3 = (0.21 \pm 0.04)$ ps have been found. These constants are most likely associated with the spectral cooling and thus with the solvent rearrangement after excitation. The amplitudes of the ultrafast dynamics vary significantly across the acquired data set. This is visualized in figure 4.3.6, where the amplitudes A_2 (triangles) and A_3 (diamonds) are normalized to A_1 and plotted against the emission wavelength. Note that both of them switch sign at around 450 nm, which means that they no longer describe dynamics that depopulate the fluorescent state, but rather ones that populate the red shifted emissive states. The results for excitation with 266 nm are shown in figure 4.3.7. The Raman peak is not observed in this data set, since the elastically scattered excitation light has a wavelength of 292 nm. Despite that, the emission dynamics look similar to excitation with 380 nm, the global analysis reveals some subtle differences. The parameters of the fit are listen in table 4.3.6. The first time constant $\tau_1 = (655 \pm 15)$ nm does vary slightly from the results with SHG excitation, however it is still consistent with the TCSPC results. Furthermore, both ultrafast time constants increase to $\tau_2 = (34 \pm 6)$ ps and $\tau_3 = (0.6 \pm 0.1)$ ps. Therefore, an excitation-energy-dependent process seems to be connected to them. The amplitudes of these time constants show a trend similar to the SHG excitation that is illustrated in figure 4.3.8. However, only for τ_3 a switch in the sign is observed, for τ_2 this change is only indicated by the trend. The interpretation of these findings are discussed in the next section alongside the TCSPC and steady state results.

Table 4.3.6: Results of the triexponential global analysis of the upconversion data of PTC in ethanol for the time constants τ_1, τ_2, τ_3, and their respective amplitudes A_i under 266 nm excitation.

wavelength [nm]	τ_1 [ps]	A_1	τ_2 [ps]	A_2	τ_3 [ps]	A_3
430		0.768		0.173		0.059
440		0.958		0.149		−0.107
450	655 ± 15	1.251	34 ± 6	0.131	0.6 ± 0.1	−0.382
460		1.509		0.087		−0.596
470		1.884		0.039		−0.923

4.4 Interpretation and discussion of the results

This section will combine the collected data on the fluorescence characteristics on PTC in various solvents that were presented throughout sections 4.1, 4.2, 4.3.1, and 4.3.2 to give a deeper insight into the occurring processes and converge the findings into a conceivable photoreaction scheme.

Long lived emission τ_0

From the TCSPC measurements a nanosecond decay with the time constant τ_0 arose in all investigates solvents, although it should be noted that this decay was very weak in methanol and ethanol with amplitudes below 0.1% and 1%, respectively. Nevertheless, a tail towards longer emission times can be seen with the help of a logarithmic intensity scaling in those data sets as well. In the more viscous solvents ethylene glycol and glycerol the time constant itself is a bit larger, which might be attributed to the bigger amplitude those solvents exhibit as well. A bigger amplitude reduces the uncertainty of the fit results, this can be seen in the statistical errors given in the respective tables 4.3.1, 4.3.2. 4.3.3, and 4.3.4. Nonetheless, the amplitude is low in all solvents compared to the main emission time τ_1. Therefore, its origin is either an impurity or a subensemble of the excited molecules. PTC in solution might form different conformers, one of which could be the source of the long-lived emission. However, it is also possible that an impurity might cause nanosecond fluorescence. One possible candidate is BCC, since it is also a byproduct of the photo-generation of PTC from TTC via illumination with UV light [121]. Also photo-degradation of PTC under UV light into BCC is possible [116]. The fluorescence of BCC has been investigated in [120] and a lifetime of 4.3 ns was found accompanied by a quantum yield of 2%. Although the reported lifetime does not match the ones presented in section 4.3.1 of this thesis, it is conceivable that the observed emission originates from a different species. This argument gets further reinforced by the fact that degradation of PTC and also the formation of TPF is faster in ethylene glycol and glycerol than it is in methanol and ethanol. This has been observed in form of decreasing count rates during the TCSPC measurements in ethylene glycol and glycerol, whereas methanol and ethanol did not show this behavior. Also TPF formation was the reason that it was not possible to determine the quantum yield in glycerol. On the ground of these arguments and the fact that amplitudes of this emission is comparably low, τ_0 will be neglected in the further discussion of the results, since it is likely not originating from PTC.

Main fluorescence τ_1

The fluorescence of PTC decays mainly with the time constant τ_1, which has been independently confirmed via TCSPC and fluorescence upconversion. The latter has also shown that the emission is insensitive to the excitation energy. A characteristic has already been hinted by the steady-state excitation spectra in figure 4.1.3 for an emission wavelength of 439 nm. This means that in PTC only one electronic state exists, which displays a radiative relaxation. This time constant has also been confirmed by transient absorption studies performed on PTC in methanol with excitation wavelength of 260 nm and 351 nm [1]. An overview of τ_1 in the different solvents alongside the respective quantum yields is given in table 4.4.1. Also the viscosity η and the empirical Kamlet-Taft parameter for

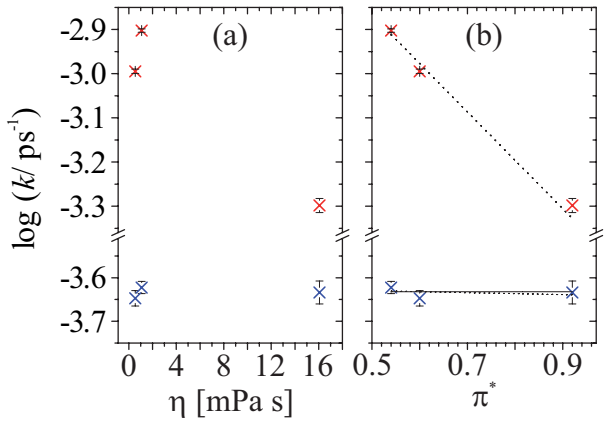

Figure 4.4.1: Dependence of the logarithmic radiative (blue crosses) and nonratiavite (red crosses) rates of the solvent viscosity η (a) and the Kamlet-Taft parameter π^* for solvent polarity (b). A linear dependence is indicated by the dotted lines, whereas the solid line shows a fit independent of π^*. Taken from ref. [1].

solvent dipolarity /polarizability for the respective solvent is noted. From the quantum yield and the lifetime the radiative rate $k_r = \frac{\Phi}{\tau_1}$ and the non-radiative rate $k_{nr} = \frac{1-\Phi}{\tau_1}$ are computed for methanol, ethanol, and ethylene glycol. Note that the error estimations for both are derived from the statistical error of Φ and τ_1. In this light, the radiative rate k_r seems to be independent of the solvent within the experimental error. Both solvent properties viscosity and dipolarity/polarizability might change the dynamics of the non-radiative relaxation however. To elucidate further on this k_r and k_{nr} are plotted against η in figure 4.4.1a and versus π^* in figure 4.4.1b. The radiative rates marked with blue crosses do not change with either property of the solvent. For the correlation with the Kamlet-Taft parameter, a fit with linear dependence to π^* is added as the dotted line alongside a fit that is independent of π^* as the solid line. Only a slight deviation is seen between both fits, which further suggests that within the experimental error the radiative rate is independent of the solvent. For the non-radiative rate however, an almost linear dependence to the Kamlet-Taft parameter is observed, which means that the process is polarity sensitive, rather than viscosity. The implication of this is is further discussed

Table 4.4.1: Solvent parameters viscosity η and Kamlet-Taft parameter π^* for dipolarity/polarizability and overview of the time constants τ_1 for the fluorescence decay of PTC in these alcoholic solvents as obtained by TCSPC. The radiative rate $\frac{\Phi}{\tau_1}$ and non-radiative rate $\frac{1-\Phi}{\tau_1}$ are also given for for methanol, ethanol and ethylene glycol (τ_0 is neglected for this calculation). Adapted from ref. [1].

solvent	η [122] [mPa s]	π^*	Φ [%]	τ_1 [ps]	$\frac{\Phi}{\tau_1}$ [10^8s^{-1}]	$\frac{1-\Phi}{\tau_1}$ [10^8s^{-1}]
methanol	0.544	0.60[123]	18.2 ± 0.3	808 ± 1	2.25 ± 0.04	10.12 ± 0.05
ethanol	1.074	0.54[123]	16.0 ± 0.2	671 ± 1	2.38 ± 0.03	12.52 ± 0.05
ethylene glycol	16.06	0.92[123]	31.6 ± 0.6	1360 ± 10	2.32 ± 0.06	5.03 ± 0.08
glycerol	934	1.07[124]	–	1030 ± 20	–	–

later in this section.

Relaxation times τ_2 and τ_3

Relaxation processes usually take place on the timescale of tens of femtoseconds to tens of picoseconds. Among the dynamics are intramolecular vibrational redistribution (IVR), vibrational and structural relaxation, and solvation, the latter meaning that solvent molecules reorient upon the excitations and the accompanied change in the dipole moment of the solute. IVR usually proceeds in less than a picosecond [13], while vibrational relaxation may be described with a biphasic model, where the first sub-ps component describes the transfer of vibrational energy to the first solvation shell, and the subsequent thermalization takes tens of picoseconds [125][126]. Solvation dynamics are usually complex, i.e. not monoexponential, and may consist of an ultrafast component followed by a slower process, that may take up to several nanoseconds for more viscous solvents [13][127]. All the above mentioned contributions are entangled and may add up to form the Stokes shift. Unraveling the whole process is difficult and often not possible.
The fluorescence upconversion studies revealed the time constants τ_2 and τ_3, which represent one or a sum of the previous mentioned processes. This can be seen from figures 4.3.6 and 4.3.8, where the amplitudes of τ_2 and τ_3 are plotted against the emission wavelength. For both excitation energies it is observed that the ultrafast components describe processes that decrease the fluorescence for the shorter wavelength emission, whereas for the longer emission wavelength they describe a rise time. This is characteristic for a Stokes shift, which τ_2 and τ_3 are most likely linked to. The determined time constants may describe the part of the shift that occurs after the IVR, in ethanol the short-time and long-time behavior of this is characterized by the time constants 0.29 ps and 16 ps [69]. Vibrational relaxation takes place on similar time scales and the observed time constants might be a convolution of solvation dynamics and vibration relaxation. This is hinted by the fact that an excitation energy dependence of τ_2 and τ_3 is found in the upconversion experiments. Both time constants were larger after excitation with 266 nm than the respective decay constants for 380 nm excitation. This is likely been caused by the excitation into a higher-lying electronic state by 266 nm and thus the additional internal conversion step causes a prolonged cooling process. That τ_2 and τ_3 do not only describe vibrational cooling, but also include the solvation dynamics is hinted by the TCSPC data in the viscous solvents. In ethylene glycol a solvation constant of $\approx$ 30 ps is reported [128][129]. This time constant is well below the resolution of the used TCSPC device, therefore this time constant would show up in the data as dynamic with a decay constant close to the resolution limit of the device, which happens to be around 110 ps. For glycerol, solvation is solute dependent (at least for coumarin dyes) and is usually on the order of several hundred picoseconds [130][131]. For PTC in glycerol a value of $\tau_2 = 204$ ps is found, which might correspond to these observations.

Conceivable photoreactions

The results presented and the discussion given so far allows for an assessment of a possible photoreaction scheme. In the simplest case PTC is excited into one or another higher-lying electronic states, then solvation and vibrational relaxation occurs and all molecules end up in the lowest lying excited state. From here a radiative path associated with τ_1 and

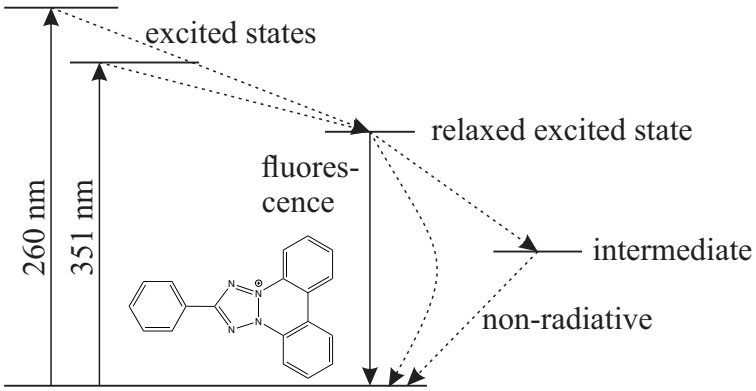

Figure 4.4.2: Conceivable photoreaction scheme of PTC after excitation via different wavelength. Taken from ref. [1].

a non-radiative path compete for the relaxation back to the ground state. This scheme is illustrated in figure 4.4.2 and the associated lifetimes and rates are listed in table 4.4.1. In the simplest case, the non-radiative path is an internal conversion, which however is not the case for PTC. This is known from transient absorption (TA) studies [1] , where a long lived TA signal is found on the nanosecond time scale. This persisting signal does not grow with τ_1, therefore the fluorescence does not lead to this state. The remaining absorption is also not connected to TPF, since its peak is located at around 560 nm (for the TPF absorption see inset of figure 4.1.1). However, it is known that PTC can be reduced to a radical [31][132][133], which is not stable in alcohols. Photo-induced formation of a PTC radical has not been reported yet, however it might occur on the short time scale as a transient species. The uptake of an electron, which is required for the generation of a radical, would be in line with the polarity dependence of the non-radiative rate seen in figure 4.4.1b, hence a radical might be formed in the non-radiative path. However, the PTC radical has a reported absorption feature at 515 nm [132]. The remaining signal in the reported TA data in [1] has a different peak wavelength, even when considering that the solvent is different and that overlap with different other features occurs, then this cannot be conciliated. Another possible non-radiative path would be photodegradation, however no fragmentation was found during the studies presented in this thesis. Additionally this would lead to a TA signal rising with τ_1 in [1], which is not observed.
In the context of the fact that the BCC fluorescence is not observed in the BCC cation [134] and that fluorophores inserted into tetrazolium salts may only fluoresce when the corresponding formazan is generated, a quenching supposedly linked to a cationic state of the tetrazolium [135][136] might takes place. This would leave the emissive state to be radical in nature. However, the PTC radical is non-fluorescent in benzene solution [132], therefore it seems more plausible that the cerulean emission of PTC originates from a cationic excited state.
The exact assignment of the dynamics occurring after photoexcitation of PTC remain unsettled at this point. It can be stated that the emissive state is likely cationic in nature and that the fluorescence decay proceeds with τ_1, however from the quantum yields it is known that the radiative path has a minor contribution to the overall relaxation dynamics. The majority of the excited molecules take a non-radiative path back to the ground state, which might involve formation of a intermediate radical, since the non-radiative

rate is highly solvent dependent. However, observation of the PTC radical has not yet been reported in literature for alcoholic solvents.
In summary, the studies presented in this chapter investigated on the photoinduced dynamics of PTC, which is one of the few known fluorescent tetrazolium salts, using steady-state spectroscopy, TCSPC, and femtosecond fluorescence upconversion. Ultrafast time-resolved fluorescence measurements performed with different excitation energies disclose a biphasic solvation and vibrational relaxation character. The fluorescence quantum yields were determined in different alcoholic solvents and found to be on the order of several tens of percent. TCSPC revealed a fluorescence lifetime of several 100 picoseconds in all solvents, that, together with the quantum yields, lead to a solvent independent radiative rate and a most likely solvent polarity dependent non-radiative rate. A possible photoreaction scheme is discussed, whose exact details remain to be illuminated by future experiments and theoretical studies.

CHAPTER 5

PULSESHAPING OF FS-LAGUERRE-GAUSSIAN LASER MODES

This chapter will give an overview of the performed experiments involving femtosecond Laguerre-Gaussian laser pulses. A detailed explanation of the laser system used can be found in section 3.2.1. Sections 3.2.2, 3.2.3, and 3.2.4 give further insight into the experimental apparatus. This chapter is ordered as follows: section 5.1 contains a more in-depth characterization of the whole setup, where the spatial and temporal properties of the beam paths for mode conversion and pulse shaping will be discussed, alongside the orbital angular momentum of the generated LG modes and their second harmonic. This section will be topped off by demonstrating spatially resolved crosscorrelations of shaped and unshaped pulses. Section 5.2 will show that the temporal shape of a LG pulse can be manipulated by means of a $4f$-pulseshaper, subsequent measurement of the temporal and spatial profile will provide a characterization of the exact shape. Lastly section 5.3 will demonstrate that a gated SHG of the LG-HG interference does change its spatial intensity distribution on the time scale of the pulse in the calculation and an experimental approach of its measurement will be given.

5.1 Setup characterization

This section provides a characterization of the Laguerre-Gaussian and the Hermite-Gaussian laser pulses that are used in the subsequent experiments. The calibration and characterization of the $4f$-pulseshaper is already given in section 3.2.3 and no further information on the temporal shape of the HG pulses will be given here. However, the spatial shape of the HG pulses will be discussed in section 5.1.1, alongside the spatial and temporal shape of the generated LG pulses. The OAM of the Laguerre-Gaussian mode will be investigated via its interference with a HG mode for the fundamental and the second harmonic in section 5.1.2. Section 5.1.3 will demonstrate spatially resolved crosscorrelations of the chirped LG pulses with a compressed HG and an oppositely chirped HG pulse.

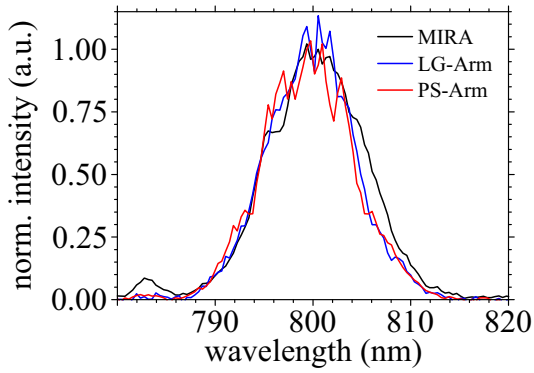

Figure 5.1.1: Normalized spectra at the laser output (black), at the end of the mode conversion beam path (blue), and after the telescope T2 behind the pulse shaper (red). Each dataset was normalized to the intensity at its respective central frequency.

5.1.1 Pulse characterization of the LG and HG Arm

This section will establish a understanding of the spatial and temporal shape of the pulses that are generated by the setup displayed in figure 3.2.10. The temporal shaping of the Hermite-Gaussian (HG) pulses that are traveling the second beampath of the interferometer-like setup has been demonstrated via the $4f$-pulseshaper in section 3.2.3. It was established that the pulses are temporally compressed at the output of the shaper. The experiments shown in sections 5.1.2 and 5.3 rely on the interference of the LG mode with the HG mode. This however is only possible if both beams have spectral overlap, which was not demonstrated up to this point. Figure 5.1.1 shows the spectra of the laser system (black), at the end of the mode converting beam path (blue), and after the telescope behind the $4f$-pulseshaper (red). Each spectrum is normalized with respect to the intensity of its central frequency, which has been determined via a Gaussian fit of the respective spectrum. The results of all three fits show that the central frequency of all three spectra is the same within one nanometer. Also the spectral FWHM is not significantly altered by the setup. The laser system provided pulses with a spectral width of $\Delta\lambda \approx 11.6\,\text{nm}$, whereas the HG and LG pulses have a spectral width of $\Delta\lambda \approx 11.0\,\text{nm}$ and $\Delta\lambda \approx 10.5\,\text{nm}$, respectively. Therefore, it can be assumed that the mode conversion via the SPP does not alter the spectrum and that the $4f$-pulseshaper does not introduce a major spatial chirp.
All the beamprofiles were measured with the CCD camera according to figure 3.2.10 and section 3.2.4. To elaborate further on the transverse laser mode, a vertical and a horizontal cut through the center of the measured profiles were taken and fitted. The model $F(x)$ for the fit contains the intensity profiles of the first four Laguerre-Gaussian laser modes LG_{00}, LG_{01}, LG_{02}, and LG_{03}, which all possess an orbital angular momentum and a doughnut-like intensity shape (see figure 2.1.11). An offset with the form $m \cdot x + n$ was assumed, since the background of the takes images was not always flat, due to stray light. The combined model $F(x)$ takes the form:

$$F(x) = A_{00} \cdot I_{LG00} + A_{01} \cdot I_{LG01} + A_{02} \cdot I_{LG02} + A_{03} \cdot I_{LG03} + m \cdot x + n \tag{5.1.1}$$

with the amplitudes A_{pl} of the respective LG mode. The beamprofile of the beam path

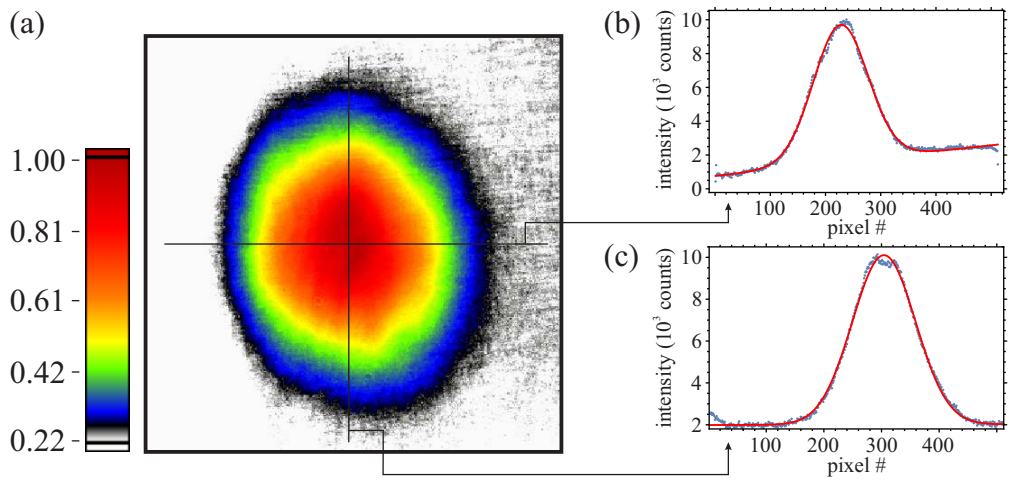

Figure 5.1.2: (a) Beamprofile of the arm containing the $4f$-pulseshaper, measured with the other beam paths blocked and no BBO crystal inserted. (b) Horizontal cut through the beamprofile (blue dots) and fit (red line) with a model described by equation 5.1.1. (c) Same as (b) for a vertical cut through the beamprofile.

containing the $4f$-pulseshaper is displayed in figure 5.1.2a. It was found that the beamprofile at the output of the shaper was distorted with respect to the input, and that the telescope T2 has an astigmatism. Reducing the astigmatism, using the second lens in T2, at the position of the CCD camera led to the displayed beamprofile. A horizontal and vertical cut through the mode is illustrated in figure 5.1.2b and 5.1.2c, respectively, as blue dots. A fit with the model $F(x)$ was performed and is included in the plots as a red line. The results of the fit show that the amplitude A_{00} is dominant for both cuts, amplitudes $A_{01}, A_{02}, A_{03} << 1\%$. The determined FWHMs of both datasets do differ by about 10% ($\Delta_H = 99$ pixel vs. $\Delta_V = 110$ pixel), which results in an elliptic beamprofile with an eccentricity of $e = 0.44$.

A typical transverse mode of the LG beam path is depicted in figure 5.1.3a. The typical doughnut shaped intensity distribution can clearly be seen. The quantification of the beamprofile was performed analogue to the HG mode. The horizontal and vertical cut through the center and the respective fit with the model $F(x)$ is displayed in figure 5.1.3b and 5.1.3c, respectively. The results show that the most dominant mode in the measured beamprofile is LG_{01} with an amplitude of $A_{01} \approx 97\%$ for both cuts. As in the case of the HG mode, the FWHM of the LG mode is sightly different for both directions, in the horizontal direction the width is estimated to be $\Delta_H = 106$ pixel and in the vertical direction $\Delta_V = 98$ pixel, which leads to an eccentricity of the LG mode of $e = 0.38$.
The temporal shape of the HG pulses can be controlled via th $4f$-pulseshaper and is already characterized in section 3.2.3. The LG pulses were also characterized by means of a FROG measurement. The experimental trace is illustrated in the top left inset of figure 5.1.4. The reconstructive algorithm retrieved a trace that is depicted in the top right of the same figure. The main plot in figure 5.1.4 shows the reconstructed field intensity (black dots) and a Gaussian fit (red line) with a FWHM of $\Delta t \approx 91$ fs. This result is consistent with data shown in section 3.2.1 within the margin of error, that is given by the day to day fluctuations of the laser performance. Another observation, that can be made from the FROG data is that the LG pulse does not have any detectable phase front

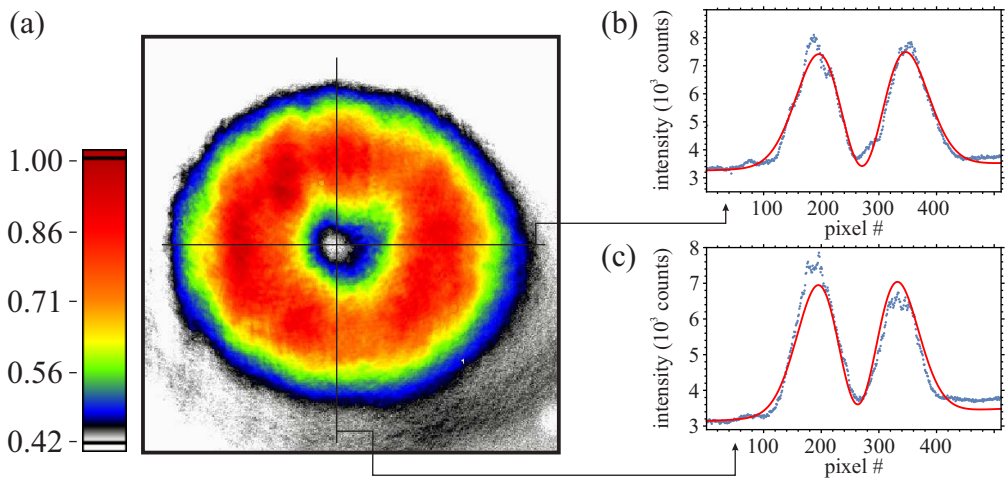

Figure 5.1.3: (a) Beamprofile of the arm containing the SPP, measured with the other beam paths blocked and no BBO crystal inserted. (b) Horizontal cut through the beamprofile (blue dots) and fit (red line) with a model described by equation 5.1.1. (c) Same as (b) for a vertical cut through the beamprofile.

tilt. The GRENOUILLE method is sensitive to this by displaying the FROG trace of a pulse with a tilted front shifted to the edge of the detecting CCD chip. All FROG traces recorded for LG and HG pulses were centered on the middle of the chip, therefore it can be assumed that no phase front tilt was present in either of the beam paths.

In summary, both beam paths display the same spectrum, which means that both beams should interfere in the experiments shown in the next section. Also the beamsprofile examination showed that the mode conversion to the LG mode is very efficient and the contrast of the mode is good. At this point no statement about the OAM of the mode can be made, since all measurements presented so far are insensitive to the spatial phase. Experiments shown in the next section will elaborate deeper into this topic. Lastly the mode conversion does not seem to have a major impact on the temporal shape of the generated LG mode, as the FROG shows almost no dispersion. The polymers used for the coating of the SPP do not seem to affect the spectral phase, only the substrate does introduce some dispersion.

5.1.2 Time integrated LG-HG interference in 1st and 2nd order

So far, the determination of the Laguerre-Gaussian beamprofile was made purely on the spatial intensity distribution of the beam. However, the more unique feature of LG beams is their orbital angular momentum, which is rooted in the spatial phase of the beam as explained in section 2.1.4. The presence and amount of OAM can be determined from the spatial interference pattern with a Hermite-Gaussian beam. The typical case of two slightly non-collinear HG beams overlapping and forming a grating like interference pattern is displayed in figure 5.1.5a. For its measurement the SPP was taken out of the beam path and both HG pulses were misaligned slightly in the horizontal direction to have a small angle in-between them, to visualize the interference grating on the CCD camera. Performing the same experiment with the SPP in place allows for the measurement of the interference grating of a LG with a HG pulse, that is illustrated in figure 5.1.5b. Using an

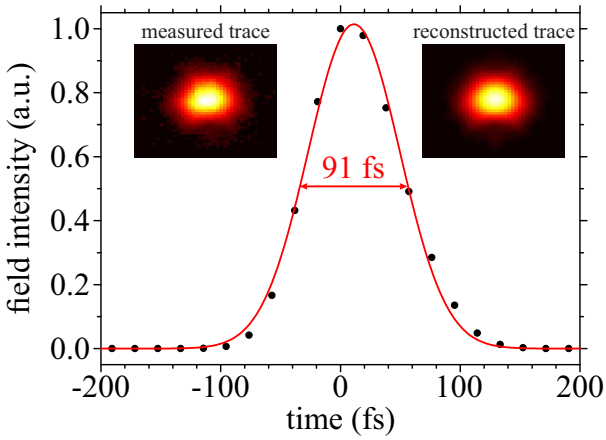

Figure 5.1.4: Reconstructed temporal field intensity of the pulse after the mode conversion by the SPP and Gaussian fit with a FWHM of $\Delta t \approx 91$ fs. The top left inset shows the measured FROG trace and the top right displays the result of the reconstruction.

LG beam gives rise to the characteristic forked-grating shape of the interference pattern, where on of the grating lines splits into two at the center of the beam. This pattern has been predicted theoretically [102] and measured routinely for the determination of the OAM of a beam [113]. Furthermore, the diffraction of a HG beam on a transmissive grating with a forked-like shape is an established way of generating LG beams [105]. From this experiment, it can be concluded that the SPP does not only generate the doughnut shaped intensity pattern of a LG beam, but also induces a spatial phase, which leads to an OAM with the absolute value of $|l| = 1$. The latter can be extracted from the number of lines the grating splits into at the optical singularity in the center of the beam. The sign of the OAM cannot be determined by this scheme, since it is not sensitive to it, similar to a polarizer that can register the presence of circular polarization, but not the direction of rotation. The interference pattern of two non-planar HG beams with different curvature leads to the common ring-shaped patterns, that are well known. An optical element with such a ringed-shaped transmission pattern is known as a Fresnel lens and can be used to focus light. This effect is based on a two dimensional Fourier transform of the diffracted

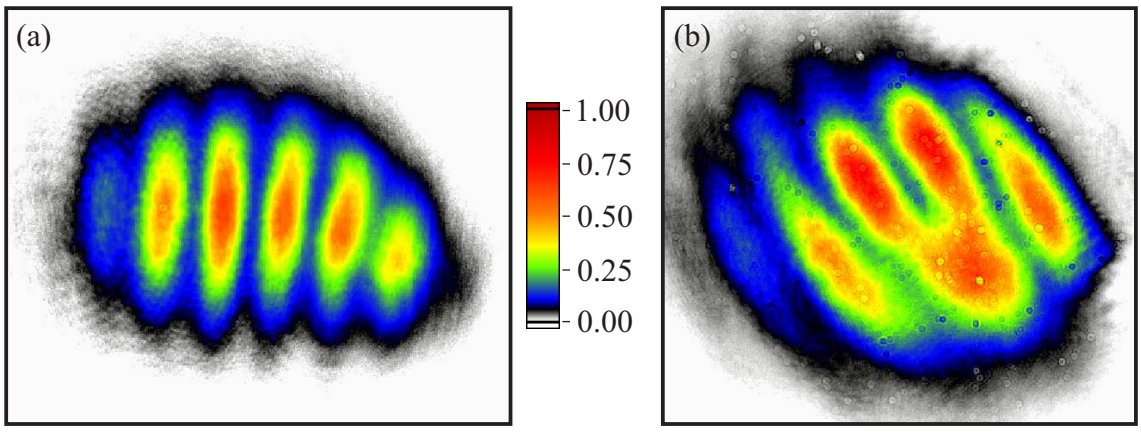

Figure 5.1.5: Measurement of the spatial interference patterns of (a) two noncollinear Gaussian beams and (b) one Gaussian and one Laguerre-Gaussian beam.

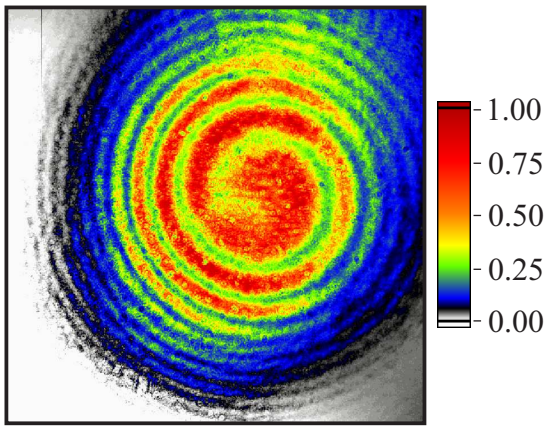

Figure 5.1.6: Measurement of the spatial interference pattern of a planar Laguerre-Gaussian and a non-planar Gaussian beam.

beam, which projects the input beam into the focus of the lens. A similar optical element known as a zone plate can be used to transform a HG input beam into a converging LG beam [102, 109, 137]. The shape of the transmission pattern of this plate is a spiral, with the number of arms representing the value of $|l|$ that is introduced into the beam. For the same reason as for the Fresnel lenses, the spiral shape of the zone plates, or vortex producing lenses, can be measured from the spatial interference patterns of non-planar waves. To this end, a lens with $f = -150\,\mathrm{mm}$ was introduced into the beam path of the $4f$-pulseshaper behind the telescope T2. The spiral wavefronts of the LG beam interfered with the spherical fronts of the HG beam to form the interference pattern shown in figure 5.1.6. The one-armed spiral pattern indicates that the OAM of the beam has a value of $|l| = 1$.

Momentum conservation requires the orbital spin of the pulse to double after second harmonic generation. To corroborate this prediction, different BBO crystals were introduced into the beam path alongside two lenses, as it is indicated in figure 3.2.10. First the type I BBO was used. To ensure type I phasematching a polarizer behind the recombining beamsplitter BS3 of the LG and HG path was used to ensure the same polarization of

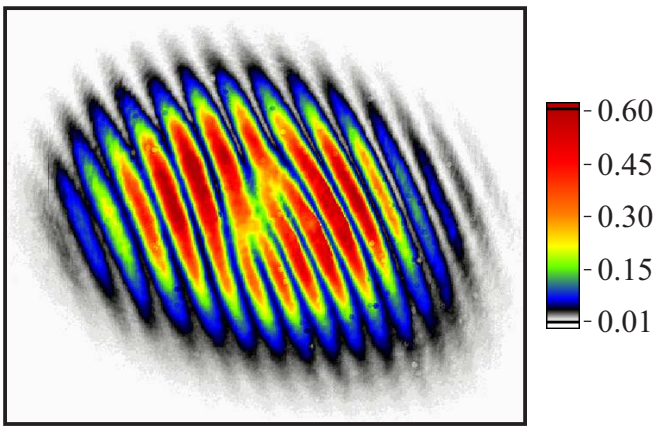

Figure 5.1.7: Measurement of the spatial interference pattern of a Laguerre-Gaussian and a Gaussian beam after frequency doubling in a type I BBO.

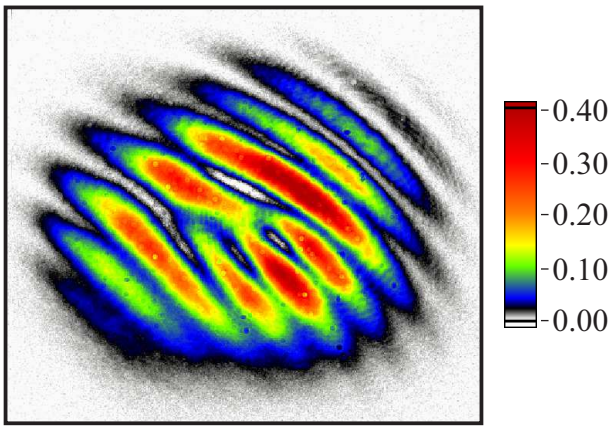

Figure 5.1.8: Spatial interference pattern of a Laguerre-Gaussian and a Gaussian beam after frequency doubling in a type II BBO.

both pulses. The BBO crystal was optimized in position and angle for the HG beam, the SHG signal was filtered from the remaining fundamental by a bandpass filter. For type I phasematching, three signal contributions are expected, two for the SHG fields of both individual fundamental fields and one for a mixing of both the LG and HG field. The first two SHG contributions should interfere to form a forked grating shaped intensity pattern with three lines converging into one, to indicate that the OAM of the LG SHG had doubled. First, the SHG of both beams was measured, while the other was blocked. It was found, that the HG beam showed an identical intensity pattern as the fundamental, the LG beam, however, displayed a beamprofile with two optical singularities. The observed SHG of the interference of the LG and HG pulse is displayed in figure 5.1.7, where an interference pattern with two forked gratings next to each other can be seen. Apparently the dominant term in the measured distribution is the third SHG contribution of both fields mixing together to form the SHG field. The reason that two optical vortices seem to appear can be linked to the SHG of the LG beam, which also showed two vortices next to each other. This could originate from the birefringence of the crystal itself, which could result in a diffraction into two beams, due to the two refractive indices the ordinary and extraordinary waves may be diffracted differently and thus gaining two different wave vectors. To investigate on the SHG of the LG field and observe a doubling of the OAM, the cooperative signal contribution of the LG-HG interference to the overall SHG signal has to be minimized.
To achieve this, the experiment was repeated using a type II BBO with slightly modified beam paths. A HWP was placed in the HG beam and polarizers were used to achieve orthogonal polarization of the HG and LG beam. The type II BBO was inserted in such a way, that the SHG signal generated by the HG beam was minimized, while the LG path was blocked. Then the polarizer in the LG beam was optimized for minimal SHG without altering the BBO angle and position, while the HG path was blocked. This ensured that both beams are orthogonal polarized and aligned to the crystal axis. Turning the BBO around the beam axis slightly enabled both beams to generate a type I SHG signal, in which no cooperative contributions were possible, since the fundamental fields were polarized perpendicular to each other. The SHG of both beams were parallel polarized along the crystal axis and thus could interfere. The intensity pattern of this interference

is illustrated in figure 5.1.8, where the single beam signals were subtracted after multiplying them by a factor of 0.4 and 0.8 for the LG and HG beam, respectively. A distinct forked-grating with three lines converging int one can be observed. This proves, that the SHG of the LG beam, which only had one optical singularity in this experiment, did carry an OAM of $|l| = 2$.

5.1.3 Spatially-resolved crosscorrelation of the shaped and unshaped pulses

In the last step of the setup assembly the SF-66 glass rod was inserted into the LG beam path. The chirped LG pulse was characterized by crosscorrelation with the HG pulse. The $4f$-pulseshaper was used as a programmable delay stage. This has also been demonstrated in common path geometry with a dual-layer SLM with very high precision [138]. To achieve this, a linear phase with varying slope was applied. As explained in section 2.1.2 a linear spectral phase delays the pulse in time by the value of the slope. This was performed using the type II BBO and monitoring the spatial beamprofile for 51 delays in 50 fs steps. Nine selected beamprofiles spanning the whole measured delay from −1200 fs to +1200 fs are depicted in figure 5.1.9a. The spatial intensity distributions show an increase in amplitude as the delay of both pulses becomes smaller. The shape remained unchanged, with only minor fluctuations from shot to shot. Each beamprofile was integrated and the amplitude was plotted against the delay in figure 5.1.9b. A Gaussian fit revealed a FWHM of the crosscorrelation of 582 fs. The compressed HG pulse has a pulse length of $\Delta t \approx 100$ fs, as had been shown in section 3.2.3. This results in a pulse length of the chirped LG pulse of $\Delta t_{LG} = \sqrt{\tau_{CC}^2 - \Delta t_{HG}^2} \approx 573$ fs. The glass rod has a length of 74.5 mm and thus introduces a quadratic spectral phase of $+20000\,\mathrm{fs}^2$. The bandwidth limited LG pulse has a temporal FWHM of $\Delta t \approx 91$ fs, as had been established in section 5.1.1. From equation 2.1.16 the dispersed LG pulse should have a length of $\Delta t \approx 616$ fs, which is consistent with the experimental result for Δt_{LG} within the error of the crosscorrelation, the day to day fluctuations in laser performance, and the statistical error of the detection.

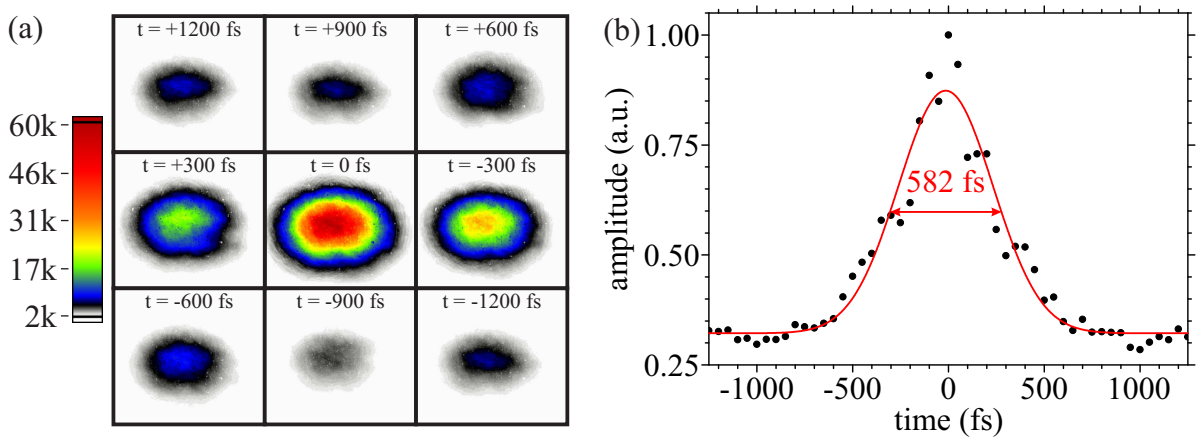

Figure 5.1.9: (a) Beamprofiles of the crosscorrelation measurement for nine delays of the compressed HG pulse relative to the chirped LG pulse. (b) Normalized integrated beamprofile versus delay and Gaussian fit with a FWHM of 582 fs.

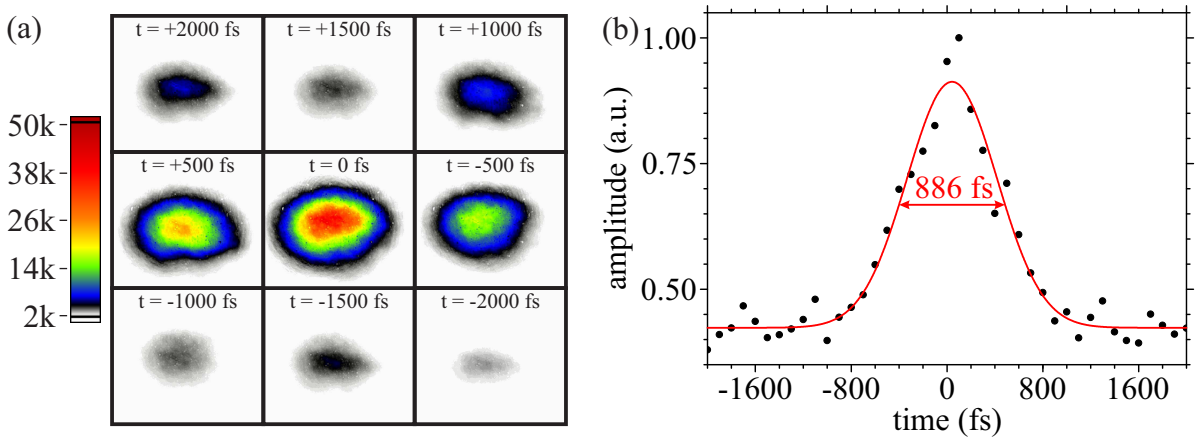

Figure 5.1.10: (a) Beamprofiles of the crosscorrelation measurement for nine delays of the inversely chirped HG pulse relative to the chirped LG pulse. (b) Normalized integrated beamprofile versus delay and Gaussian fit with a FWHM of 886 fs.

In the next step, the $4f$-pulseshaper was used to apply a quadratic spectral phase of $b_2 = -20000\,\mathrm{fs}^2$ to the HG pulse. Another crosscorrelation was measured to check for consistency in the pulse durations. The beamprofiles of the type II SHG signals were measured for 41 delays with a step size of 100 fs. Nine intensity distributions for selected delays are displayed in figure 5.1.10a. Again no significant change in the shape of the profile was recognized upon variation of the delay. Each distribution was integrated and then plotted against the delay in figure 5.1.10b. A Gaussian fit of the dataset revealed a FWHM of the crosscorrelation of 886 fs. With the previous result for the length of the chirped LG pulse, the inversely chirped HG pulse has a duration of $\Delta t_{HG} \approx 676\,\mathrm{fs}$. Both pulses share the same spectrum, therefore they should ultimately have the same band limited pulse length and since their quadratic spectral phase only differs in sign, they should have the same chirped pulse length of $\Delta t \approx 616\,\mathrm{fs}$. Considering that this indirect determination has several steps, each with an uncertainty, the results for the pulse lengths are consistent. It is also demonstrated that both pulses have a comparable pulse length, only the sign of the chirp is different.
Crosscorrelation was chosen for pulse characterization here, since the GRENOUILLE device does not deliver reliable results for pulse length larger than 500 fs and the intensity of the chirped pulses were not sufficient for a measurement via the autocorrelator.

5.2 Temporally shaped LG pulses

The experiments on fs-LG pulses presented so far did only elaborate on the spatial shape, OAM, bandwidth limited temporal shape, and dispersed temporal shape. To the best of the authors knowledge pulseshaping of fs-LG pulses has not been demonstrated yet in literature. A setup for achieving this, however, is rather straight-forward, since a temporally shaped HG pulse should also be converted into a temporally shaped LG pulse by the SPP. In the experiments shown in this section the $4f$-pulseshaper arm of the interferometer-like setup, illustrated in figure 3.2.10, was exclusively used and the SPP for mode conversion was placed in the beam path succeeding beamsplitter BS3. No

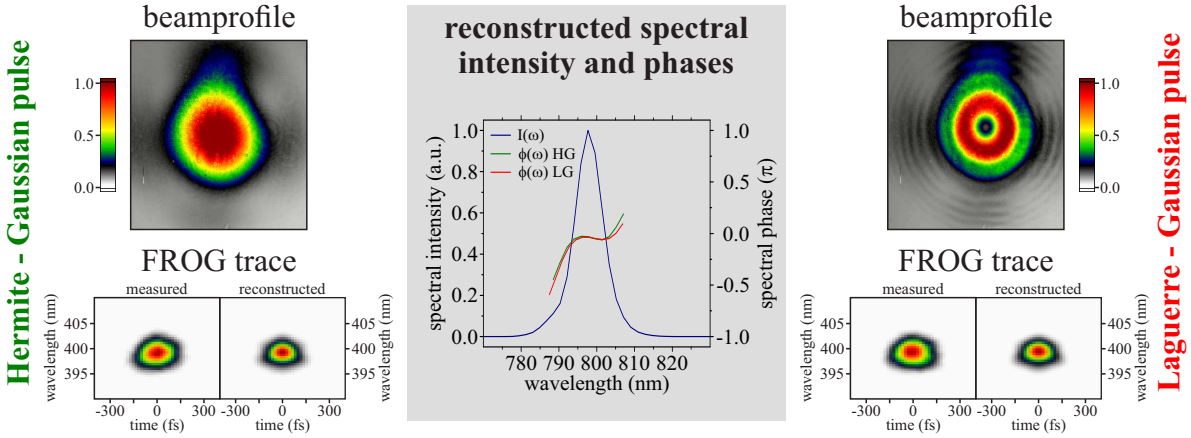

Figure 5.2.1: Spatial and temporal shape of the Hermite-Gaussian (left) and Laguerre-Gaussian (right) pulse for their respective compensation phase. The beamprofiles, measured and retrieved FROG trace are shown for both laser modes. The reconstructed spectral intensity of the HG pulse and the spectral phases for both modes are shown in the middle.

focusing optics or BBOs were used, the beamprofile was directly measured by the CCD camera after an additional beamsplitter redirected half of the beams intensity into the FROG device for a simultaneous measurement of the temporal structure of the pulse. Four different spectral phases were imprinted by the pulseshaper, the same approach was repeated without the SPP for a HG pulse for comparison. The first phase tested was the compensation phase for each of the pulses, which was found iteratively with the FROG trace of the GRENOUILLE as a live feedback. It was found, that the compensation phases for the HG and LG mode did differ only slightly, compensating for the additional glass of the SPP. The Taylor coefficients for both modes are:

HG-pulse	LG-pulse
$b_0 = -1$	$b_0 = -1$
$b_1 = 65\,\mathrm{fs}$	$b_1 = 65\,\mathrm{fs}$
$b_2 = -4800\,\mathrm{fs}^2$	$b_2 = -4900\,\mathrm{fs}^2$
$b_3 = -15000\,\mathrm{fs}^3$	$b_3 = -18000\,\mathrm{fs}^3$.

No significant difference in the compensation phases arises due to the presence of the SPP. The beamprofiles, measured, and retrieved FROG trace for the HG and LG mode are shown in figure 5.2.1 left and right, respectively. The middle illustrates the reconstructed spectral intensity of the HG pulse and the spectral phases of the HG and the LG pulse. The spectral intensity profile of the doughnut shaped beam was identical to the one of the HG pulse and is not shown here. The spectral phases of both modes are flat over the course of the spectrum, only deviating at the edges, where the lower intensity impedes an exact determination. Nevertheless, the compensation phase provided good results for both modes as the measured FROG trace in both cases is highly similar and almost perfectly symmetric. The reconstruction yields pulses with a duration of $\approx 100\,\mathrm{fs}$ for both modes and spectra with a FWHM of $\approx 9\,\mathrm{nm}$, which according to equation 2.1.14 represents a bandwidth limited Gaussian shaped pulse.
In the next step, a quadratic phase term of $b_2 = -15000\,\mathrm{fs}^2$ was added to the respective

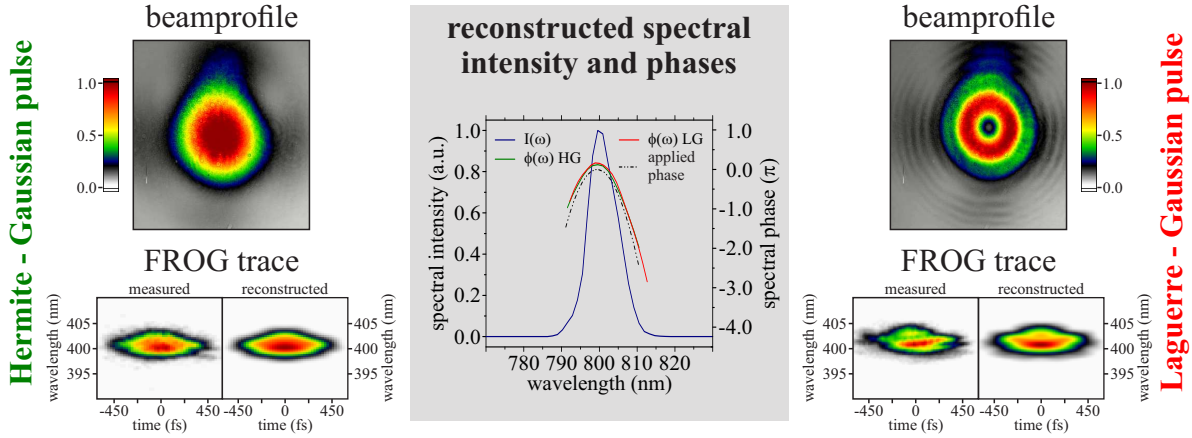

Figure 5.2.2: Spatial and temporal shape of the Hermite-Gaussian (left) and Laguerre-Gaussian (right) pulse for their respective compensation phase plus a quadratic phase term of $b_2 = -15000\,\mathrm{fs}^2$. The beamprofiles, measured and retrieved FROG trace are shown for both laser modes. The reconstructed spectral intensity of the HG pulse and the spectral phases for both modes are shown in the middle.

compensation phase of each mode. It was not possible to apply a larger chirp due to limitations in the maximum pulse length the GRENOUIILE device is able to determine. Applying the additional phase did not alter the beamprofile of either the HG nor the LG mode, as can be seen from figure 5.2.2. The measured FROG trace for the HG mode showed a significant stretch in time, note that the time axis of the trace did change in comparison to figure 5.2.1. The FROG of the LG pulse yields a slightly asymmetric trace, which is attributed to a non-ideal incoupling into the device. In both cases, however, did the retrieval algorithm reconstruct the measured traces well. The spectral intensity of the results for the HG pulse is shown in the center, alongside the spectral phases for both modes, and the calculated applied phase (dashed line). The retrieved phases match the theoretical one very well. The reconstructed spectral and temporal FWHM is $\approx 9.2\,\mathrm{nm}$ and $414\,\mathrm{fs}$, respectively, for the HG and $\approx 9.9\,\mathrm{nm}$ and $445\,\mathrm{fs}$, respectively, for the LG pulse. According to equation 2.1.16 a $100\,\mathrm{fs}$ input pulse is elongated in time by a dispersion of $b_2 = 15000\,\mathrm{fs}^2$ to $428\,\mathrm{fs}$. It becomes apparent that the non-ideal incoupling for the LG pulse led to some deviation from the previous results in terms of spectral width and from the theoretical calculation in the case of the temporal duration. However, assuming a bandwidth limited Gaussian pulse with a spectral FWHM of $9.9\,\mathrm{nm}$ and applying a chirp of $b_2 = 15000\,\mathrm{fs}^2$ would result in a pulse duration of $448\,\mathrm{fs}$. The experimental outcome for the LG pulse, therefore, is self consistent and the minor deviations (¡10%) with the previous results can thus be attributed to the incoupling into the device. For the HG mode, the results match the previous ones and the theoretical calculation quite well.

For the third applied phase, a cubic phase term of $b_3 = 10^6\,\mathrm{fs}^3$ was added to the respective compensation phase for each pulse. As explained in section 2.1.2 this kind of dispersion leads to sub-pulses in time, where the temporal phase between each sub-structure jumps by a value of π. The results for both modes are displayed in figre 5.2.3, from which it can again be concluded that the spectral phase does not have an influence on the spatial beamprofile for either mode. The measured FROG traces showed slight asymmetries for the HG as well as the LG pulse, which are attributed to the incoupling into the

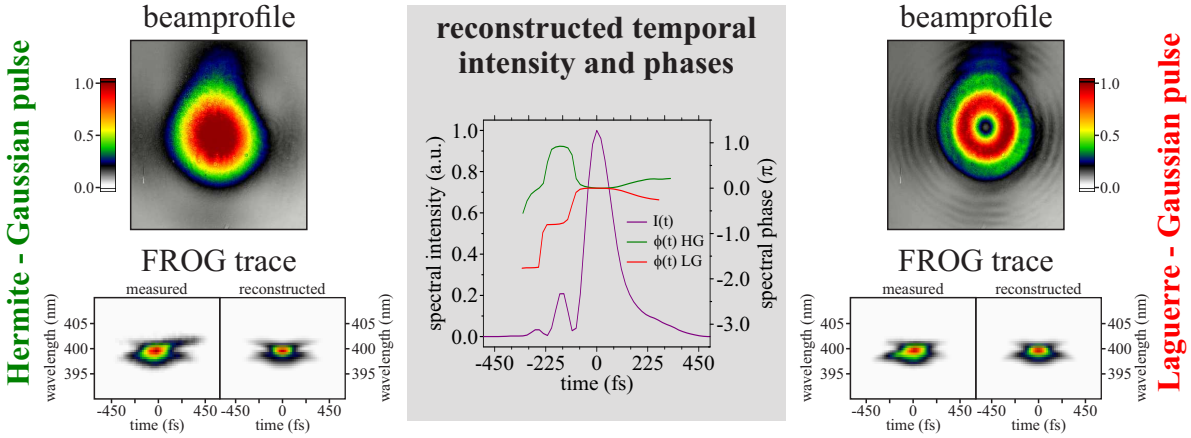

Figure 5.2.3: Spatial and temporal shape of the Hermite-Gaussian (left) and Laguerre-Gaussian (right) pulse for their respective compensation phase plus a qubic phase term of $b_3 = -10^6\,\mathrm{fs}^3$. The beamprofiles, measured and retrieved FROG trace are shown for both laser modes. The reconstructed spectral intensity of the HG pulse and the spectral phases for both modes are shown in the middle.

device. Especially small temporal structures in the characterized pulses are susceptible towards non-ideal execution of the FROG. However, the typical star-like shape of the FROG traces of pulses with a cubic spectral phase can be seen. The reconstruction elucidates this further, as for both modes the retrieved trace looks remarkably similar. The reconstructed temporal intensity of the HG pulse is shown in the center of figure 5.2.3 confirms the occurrence of sub-pulses in time. The temporal phase for both modes is plotted alongside the intensity and shows jumps with an amplitude of approximately π between the sub-structures. The sign of the change, however, cannot be determined by this SHG-FROG scheme, similar to the sign of the b_2 component above. The temporal intensity of the LG pulse is in accordance to the illustrated one, however, the temporal duration cannot be converged into a single number, as done before, and compared. The reconstructed spectra, that are not shown here, are almost identical and have a width of $\approx 7\,\mathrm{nm}$. This seems to contradict the results for the compensation phase shown above, however, note that the spectral components further away from the central frequency are combined into sub-pulses further delayed from the main pulse. These small temporal features, as already stated, are susceptible towards imperfection in the implementation of the FROG. Therefore, they might not be accounted for, since they do not show up in the trace with a significant amplitude.

The last phase tested was a linear phase of $b_1 = -210\,\mathrm{fs}$ for $\omega < \omega_0$ and $b_1 = 210\,\mathrm{fs}$ for $\omega > \omega_0$ added to the compensation phase of each mode. This V-shaped phase results in two pulses with different spectra, since one half of the spectrum witnesses a linear phase with a negative slope, while the other half is delayed by a linear phase with a positive slope of the same magnitude. This leads to a so-called colored double-pulse [139, 140]. The FROG trace of the double-pulse is more complicated and structured as the ones shown above. As two copies of the double-pulse are delayed with respect to one another, at some point temporal overlap of two out of the overall four pulses is achieved. Since the double-pulse is only copied and not inverted in time, the first two pulses overlapping upon changing the delay do always have a different spectrum. This leads to a peak in

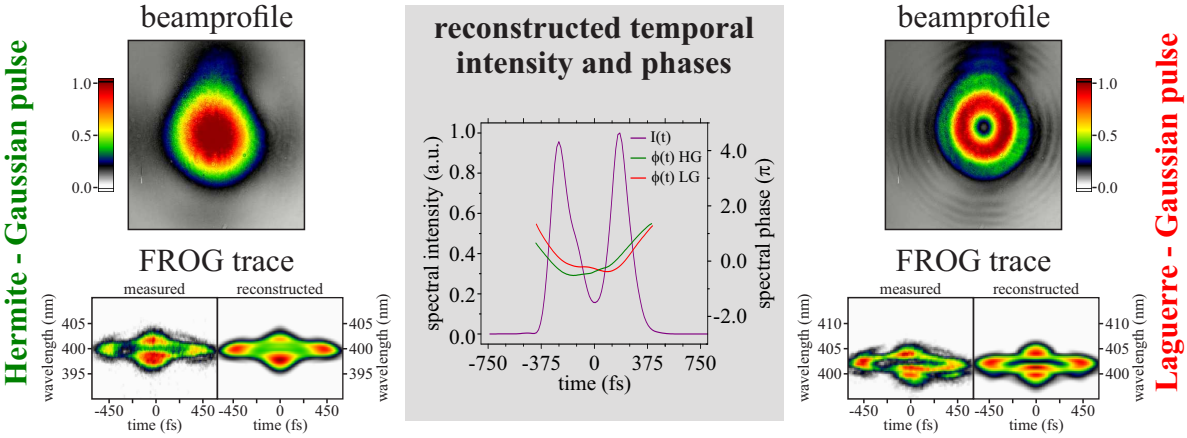

Figure 5.2.4: Spatial and temporal shape of the Hermite-Gaussian (left) and Laguerre-Gaussian (right) pulse for their respective compensation phase plus a linear phase term of $b_1 = 210\,\text{fs} \times sgn(\omega - \omega_0)$, resulting in a v-shaped phase. The beamprofiles, measured and retrieved FROG trace are shown for both laser modes. The reconstructed spectral intensity of the HG pulse and the spectral phases for both modes are shown in the middle.

the FROG trace at the center frequency of the original pulse, since the spectra of both involved pulses do add up to the original spectrum. As the delay is decreased further, those two pulses do no longer overlap and the feature of the trace vanishes. However, as the delay approaches zero, complete overlap of the double-pulse sequence is achieved. In this scenario the sub-pulses overlapping do have the same spectral components. This leads to two peaks in the FROG trace, that are displaced from the center frequency, but occurring at the same delay. As the pulse sequences are delayed further the same events play out in reversed order, as a SHG FROG trace always has to be symmetrical with respect to the zero delay. In the experiment, FROG traces with the described shape can be observed for the HG as well as the LG mode, as can be seen in figure 5.2.4. Imperfections in the traces originate from the incoupling into the device. The temporal intensity of the reconstructed LG pulse is shown in the center of figure 5.2.4 and displays a distinct double-pulse shape. The reconstructed temporal intensity of the HG mode, that is not shown, displays the same behavior, however both sub-pulses did not have the same amplitude. This is linked to the trace, in which an asymmetry between two central peaks can be observed, the retrieval remodels this behavior, that is most likely linked to the alignment. The temporal distance between the two maxima of the reconstructed temporal intensity is $\approx 430\,\text{fs}$. Considering each part of the spectrum is delayed 210 fs away from time zero, the retrieval does confirm the expectation of the temporal locations of the sub-pulses. The beamprofiles of both modes remain unchanged by temporal shaping of the pulses.

In summary, it has been demonstrated that shaping fs-pulses in time does not alter the conversion of a HG mode into a LG mode by a SPP in any significant way. The doughnut-shaped beamprofile remained unchanged, even after temporally splitting the spectrum of the pulse into two separate pulses. Furthermore, characterization of LG pulses using a commercial FROG device has been shown to deliver reliable results with the same accuracy as for a comparable HG pulse.

At this point it should be noted, that $4f$-pulseshapers are known to have a certain cross-

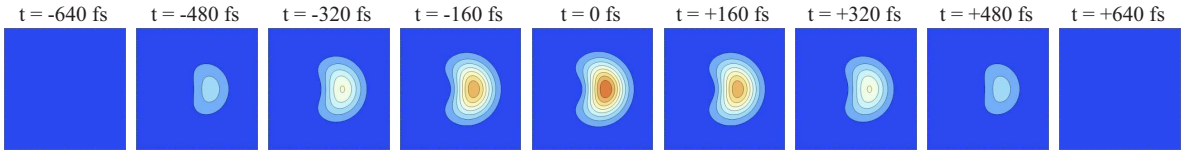

Figure 5.2.5: Simulation of the time resolved spatial interference of a HG pulse with $b_2 = +20000\,\mathrm{fs}^2$ and a LG pulse with $b_2 = +20000\,\mathrm{fs}^2$ for a time scale from $-640\,\mathrm{fs}$ to $+640\,\mathrm{fs}$.

talk between the temporal and spatial profile of a pulse. This is known a space-time coupling (STC) and originates from diffraction effects at the SLM [141–143]. Especially modulators with few pixels and spectral phases, which have a lot of phase jumps, are known to cause STC. However, in the performed studies no indications for additional problems with STC after introducing the SPP was found. Furthermore, the telescope behind the $4f$-shaper also included a pinhole, which should reduce STC to a minimum.

5.3 Time evolution of the spatially resolved LG-HG interference

The spatial interference of the HG and LG mode displayed in figure 5.1.5b in section 5.1.2 shows the time integrated interference of both pulses. The time resolved spatial intensity of the interference of a HG and LG pulse, both with a quadratic spectral phase term of $b_2 = +20000\,\mathrm{fs}^2$, are displayed in figure 5.2.5 for 160 fs steps covering an interval of $t = -640\,\mathrm{fs}$ to $t = +640\,\mathrm{fs}$, which was already outlined in ref. [144]. The pulses used for the calculation have a central wavelength of 799 nm, a spectral FWHM of $\Delta\lambda = 12\,\mathrm{nm}$, which corresponds to a bandwidth limited pulse with a duration of $\Delta t \approx 78\,\mathrm{fs}$, and no other spectral phase components other than the mentioned one. No dynamics can be seen in the simulation, the amplitude of the interference follows the envelope of the square of

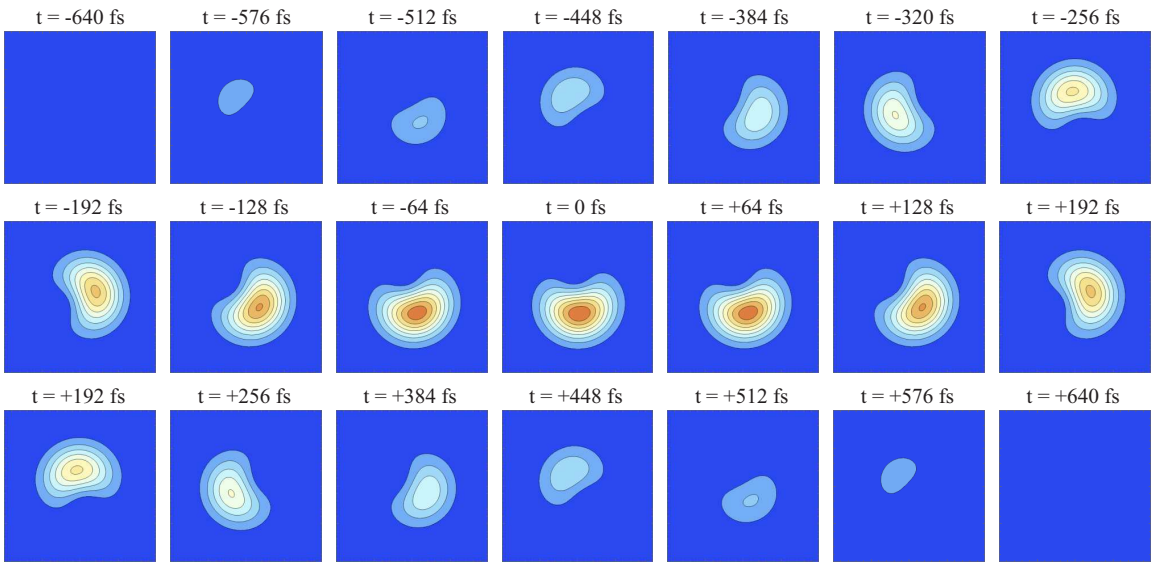

Figure 5.3.1: Simulation of the time resolved spatial interference of a HG pulse with $b_2 = -20000\,\mathrm{fs}^2$ and a LG pulse with $b_2 = +20000\,\mathrm{fs}^2$ for a time scale from $-640\,\mathrm{fs}$ to $+640\,\mathrm{fs}$.

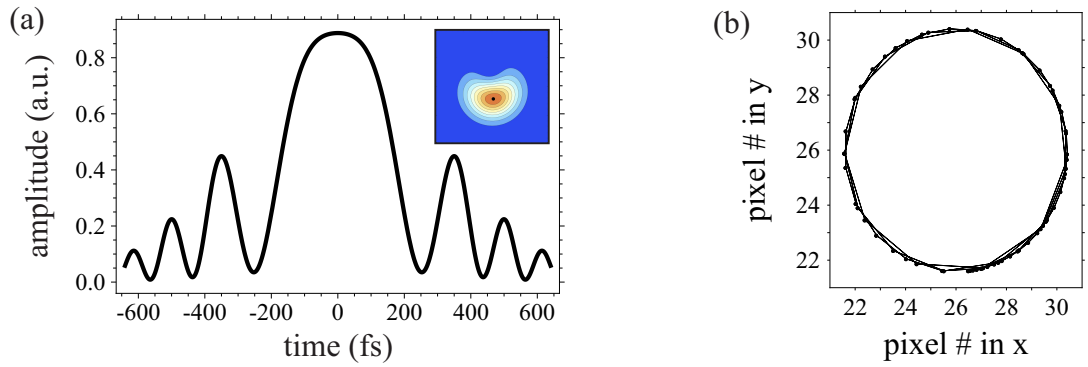

Figure 5.3.2: (a) Amplitude versus delay for the point in space, at which the intensity is maximal for $\tau = 0$, which is indicated by the inset by a black dot. (b) Coordinates of the center of mass for delays in 10 fs steps. The connecting lines show the previous and the subsequent delay.

the combined electric fields. The intensity shows a bean-like shape and is located right of the propagation axis. This is expected, since the LG pulse has a helical wavefront, which allows constructive interference of the fields on one half of the spatial distribution, while the other half will always have the opposite sign in its phase and therefore destructively interfere. The situation, however, changes when the sign of one of the spectral phases is inverted. The results of a simulation incorporating this is shown in figure 5.3.1. The HG pulse used for this calculation has a spectral phase of $b_2 = -20000\,\mathrm{fs}^2$, while the LG pulse remains positively chirped. As a result, it can be seen that the spatial intensity distribution at each time has the aforementioned bean-like shape, but with a changing orientation in space as time progresses. The reason for this rotation dynamics is the varying point in space, at which constructive interference occurs, when the pulses are oppositely chirped. The motion was investigated further by plotting the intensity variation at one point in space with time, which is illustrated in figure 5.3.2a. The location in space, that was chosen for the calculation was the maximum of the intensity distribution at time zero, as indicated in the inset of figure 5.3.2a by a black dot. Around time zero, the motion is slow and no significant variation can be seen until 100 fs. After that, however, almost three full rotations can be seen within 350 fs with an angular frequency, that remains almost constant. The rotation is symmetric with respect to time zero, thus changes direction at time zero, as can be seen from figure 5.3.1. Additionally, the center of mass for each time between −640 fs and +640 fs was calculated in 10 fs steps. The center of mass x_i of a function $I(x)$ can be derived according to

$$x_i = \frac{\sum x \cdot I(x)}{\sum I(x)}, \tag{5.3.1}$$

whereas for 2D arrays, a center of mass can be calculated by integrating over one dimension and calculating x_i over the remaining one and then repeating the process, while integrating over the other dimension to compute y_i. For this purpose, the spatial intensity distributions were calculated on a 51×51 pixel grid, since the analytic computation was not feasible for the results of the next section, but consistency of the methods was a keynote. The coordinates of the center of mass of the HG-LG interference evolve with time according to figure 5.3.2b, where the connecting lines illustrate the previous and

subsequent delay. From the calculations it is clear that the interference moves on a circle. The presented dynamics are, however, not measurable with time-integrated detectors like CCD cameras. The setup is designed to determine the time-resolved interference by gating it with an orthogonal polarized HG pulse in a type II SHG process. The results of the experiment will be shown in section 5.3.2 after its simulation is presented in the following section 5.3.1.

5.3.1 Simulation

The calculations of the time resolved dynamics of the LG-HG interference presented above are performed using two space and time dependent fields and deriving the spatial intensity at each time that is shown. The experimental setup, however, does detect the spatial SHG intensity distribution as a function of the time delay of the third pulse, that acts as a gate in the type II SHG process. If the gate pulse would be infinitely short, the result of the gating would be the same as depicted in figure 5.3.1 multiplied by the spatial intensity distribution of the gate pulse. For an infinitely long gate pulse no rotation would be observable at all, since all rotations will be averaged over and a Gaussian shaped intensity distributions centered on the beam axis would be obtained. This section will provide a simulation of the experimental data with a gate pulse of finite duration. For this purpose, three electric fields were assumed, that take the form of $\mathcal{E}_{pl}(r,\theta,z)$ from equation 2.1.28. Calculations were performed in Cartesian coordinates, so r is replaced by $\sqrt{x^2+y^2}$ and θ by the argument of $x+iy$. The constants A, w_0, k, and z_0 were set constant and the same for all fields and all calculations were performed for $z=0$. The spatial field was complemented by a temporal field to achieve a full space and time dependent description that takes the form:

$$\mathcal{E}(p,l,x,y,z,t) = \mathcal{E}_{pl}(\sqrt{x^2+y^2}, Arg[x+iy], z)\cdot\mathcal{E}(t) \tag{5.3.2}$$

with

$$\mathcal{E}(t) = \mathcal{F}^{-1}\left[e^{-4\cdot\mathrm{Log}(2)\left(\frac{\omega-\omega_0}{\sqrt{2}\Delta\omega}\right)^2} e^{-i\phi(\omega)}\right], \tag{5.3.3}$$

where $\mathcal{F}^{-1}$ denotes the inverse Fourier transformation. The central frequency ω_0 and spectral FWHM $\Delta\omega$ were chosen to be 799 nm and 12 nm, respectively, for all three pulses. The spectral phase $\phi(\omega)$ was zero for the gate pulse, for the LG and HG pulses a quadratic spectral phase with $b_2 = \pm 20000\,\mathrm{fs}^2$ was assumed. The mode indices for the Gaussian beams were set to $p=l=0$ and to $p=0$ and $l=1$ for the Laguerre-Gaussian beam. For the gate pulse, a delay τ was added to the time dependence, to enable shifting the pulse with respect to the other two, that stay fixed in time. The space- and time-dependent fields of the chirped Gaussian pulse $\mathcal{E}_{HG}$, the inversely chirped Laguerre-Gaussian pulse $\mathcal{E}_{LG}$ and the bandwidth limited gate pulse $\mathcal{E}_G$ were then used to calculate the SHG field $\mathcal{E}_{SHG}$ of the desired interaction. First, the results for gating either $\mathcal{E}_{HG}$ or $\mathcal{E}_{LG}$ by $\mathcal{E}_G$, while the other chirped field is not present, was calculated. The SHG intensity for these two-field interactions takes the form of:

$$I_{SHG} = |\mathcal{E}_{SHG}|^2 = |(\mathcal{E}_G+\mathcal{E}_{LG})^2|^2 = |\mathcal{E}_G^2+\mathcal{E}_{LG}^2+2\mathcal{E}_G\mathcal{E}_{LG}|^2 \tag{5.3.4}$$

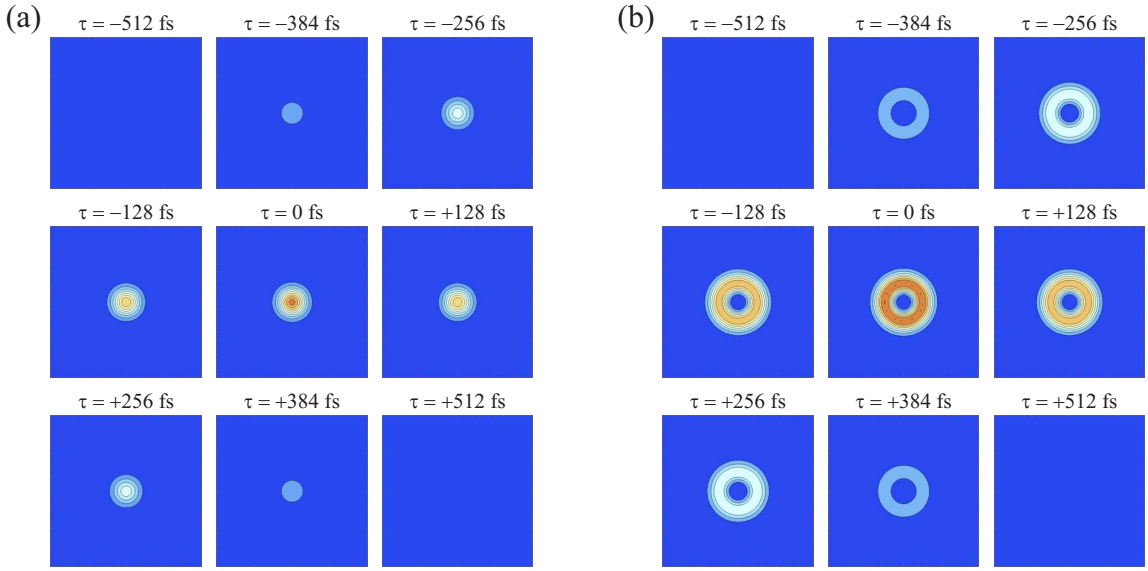

Figure 5.3.3: (a) Simulation of the spatial intensity of the SHG signal of the gated HG pulse following a type II SHG process for delays of the gate between −512 fs and +512 fs. (b) Same as (a) for the gating of the LG pulse.

in the example of a gating of the Laguerre-Gaussian pulse. Considering type II phase-matching in the SHG process, the first two terms on the right side of the above equation vanish and only the third describes the SHG intensity. The results for the simulation of the gating of the HG and LG pulses are displayed in figure 5.3.3a and b, respectively, the time-dependent intensity of the SHG was integrated and then illustrated for fifteen different delays in the interval of −512 fs to +512 fs.
This simulation basically represents a type II intensity crosscorrelation with spatial resolution. From figure 5.3.3a and b, it is observed that no dynamics are supposed to appear, apart from amplitude changes of the intensity following the envelope of the crosscorrelation. This was also expected and reproduced by the calculation.
For the interaction of all three pulses the SHG field is more complicated and the intensity takes the form:

$$I_{SHG} = |\mathcal{E}_{SHG}|^2 = |\mathcal{E}_G^2 + \mathcal{E}_{LG}^2 + \mathcal{E}_{HG}^2 + 2\mathcal{E}_G\mathcal{E}_{LG} + 2\mathcal{E}_G\mathcal{E}_{HG} + 2\mathcal{E}_{LG}\mathcal{E}_{HG}|^2. \tag{5.3.5}$$

The general solution for the SHG intensity of a three field interaction has thus fifteen different terms. However, for type II phasematching only the fourth and fifth term on the right side of the above equation contribute to the signal. That leads to a SHG intensity of

$$I_{SHG} = |4\mathcal{E}_G^2\mathcal{E}_{LG}^2 + 4\mathcal{E}_G^2\mathcal{E}_{HG}^2 + 8\mathcal{E}_G^2\mathcal{E}_{LG}\mathcal{E}_{HG}|. \tag{5.3.6}$$

Comparing this to the time-resolved intensity of the HG-LG interference displayed in figure 5.3.1, that has the form

$$I = |\mathcal{E}_{LG} + \mathcal{E}_{HG}|^2 = |\mathcal{E}_{LG}^2 + \mathcal{E}_{HG}^2 + 2\mathcal{E}_{LG}\mathcal{E}_{HG}|, \tag{5.3.7}$$

it becomes apparent that I_{SHG} is the same as I multiplied by $4\mathcal{E}_G^2$. Therefore, the rota-

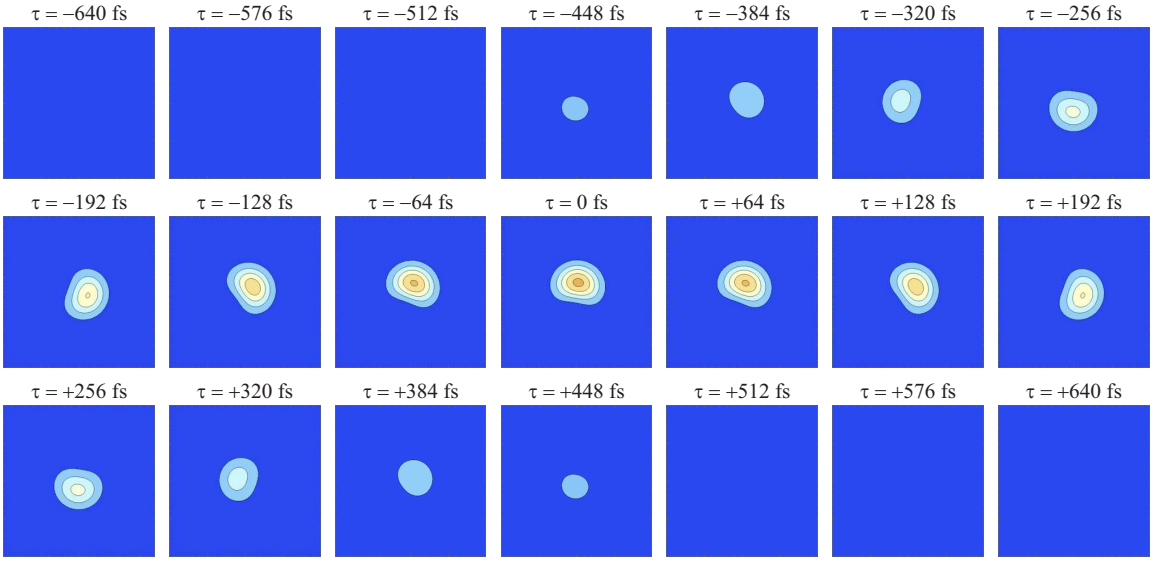

Figure 5.3.4: Simulation of the spatially resolved SHG intensity of the HG-LG interference for 21 different gate delays in the interval between −640 fs to +640 fs.

tion behavior should remain the same in the gated second-order detection with type II phasematching. The results of the calculation of the SHG intensity for 21 different delays τ of the gate pulse is illustrated in figure 5.3.4. It can be seen that the SHG intensity does indeed rotate around the beam axis in the same way as the time-resolved intensity of the interference in figure 5.3.1 does.

The point in space with the highest intensity for $\tau = 0$ fs shows a varying amplitude with the delay of the gate, this is illustrated in figure 5.3.5a. It can be seen, that the amplitude for this point in space is highest for a delay of ±100 fs around time zero. The dynamics are similar to the ones of the interference without gating, depicted in figure 5.3.2a, however not as pronounced, especially for time delays > 400 fs. Also the center of mass of the intensity distributions were calculated for delays between 0 fs and 590 fs in 10 fs steps in the same way as for figure 5.3.2b. Since the dynamics are symmetric with respect to time zero, it is sufficient for its description to use only positive delays. The calculations were done numerically, due to limitations in computational power. To this end, the analytical intensities for each delay and time were converted into 2D-arrays with 51×51 numerical values and integrated in time. The center of mass for every delay was calculated according to equation 5.3.1.

The results that were derived are depicted in figure 5.3.5b, where the coordinates of the center of mass are illustrated as a dot and the connecting lines show the center of mass of the previous and subsequent delays. The center of mass coordinates are arranged in a spiral shape with time zero being the outer most point, at which the spiral starts turning inwards. Within the first 100 fs the center of mass of the intensity distribution does rotate less than an eighth around its beam axis, whereas in the next 100 fs it rotates by about a fourth. After about 200 fs the angular velocity of the rotation seems to be more or less constant as the center of mass spirals inwards. The first full rotation within the simulation starting at time zero takes about 370 fs, the second 150 fs, and the third is not completed within the time frame of the calculation. The spiral shape itself arises from the circular motion of the interference (see fig 5.3.2) and from the fact that the gate pulse has a finite

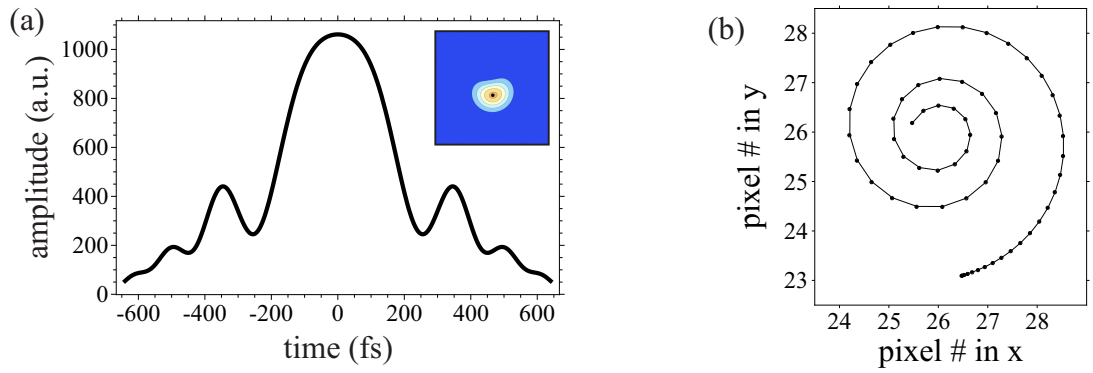

Figure 5.3.5: (a) Amplitude versus delay for the point in space, at which the intensity is maximal for $\tau = 0$, which is indicated by the inset. (b) Coordinates of the center of mass for delays in 10 fs steps. The connecting lines show the previous and the subsequent delay.

duration. Around time zero, where the rotation of the interference is slow, the gating works perfectly fine, however, as the rotation becomes faster towards larger delays, more angular rotation of the beamprofile happens within the duration of the gate. Therefore, the upconverted signal for larger delays averages the rotation over a larger arch and results in a signal closer to the center pixel of the whole image.

5.3.2 Measurement

The experiments were performed with the setup exactly arranged as depicted in figure 3.2.10. The BBO type II crystal was inserted in front of the camera. All beamprofiles presented in this section were taken with an exposure time of 500 ms and averaged over 240 images, thus a total of 2 min beam exposure of the camera produced one final image for each delay. First the HG and LG pulse alone were gated and the spatially resolved SHG signal was detected. The results for the HG beam are illustrated in figure 5.3.6a for nine delays between −512 fs and +512 fs. Notice that the overall amplitude follows the envelope of the crosscorrelation, as also observed in the simulation in figure 5.3.3a. For the gated LG pulse the results are illustrated in figure 5.3.6b, a clear deviation from the simulated data in figure 5.3.3b is obvious. First, the intensity of the signal persists much longer than expected with significant amplitude and second, the beamprofile does only take the doughnut shape expected from the calculation for a delay of +256 fs and +384 fs. For all other measured delays a bean-like shape of the spatial intensity distribution is observed. A reason for this behavior could be a smaller beam size of the gate pulse, the result would be that not the whole beamprofile of the LG pulse can contribute to the SHG signal. However, that for two delays a doughnut shape is observed points towards another issue, namely that either the gate, the LG pulse, or both show a noticeable beam pointing. Averaging over a total exposure of 2 min was thought to eliminate this source of error, but the problem might still be present. The fact that the SHG signal in both cases persists for longer delays is over-exaggerated in the presented illustrations of the experiments, since the color code used was the same as for the results in sections 5.1, 5.1.2, 5.1.3, and 5.2, which is not linear as the color code used for the simulated data in section 5.3.1. The nonlinear code was chosen to reinforce the visibility of smaller changes in the measured beamprofiles. Nevertheless, the issue of a certain spatial instability of

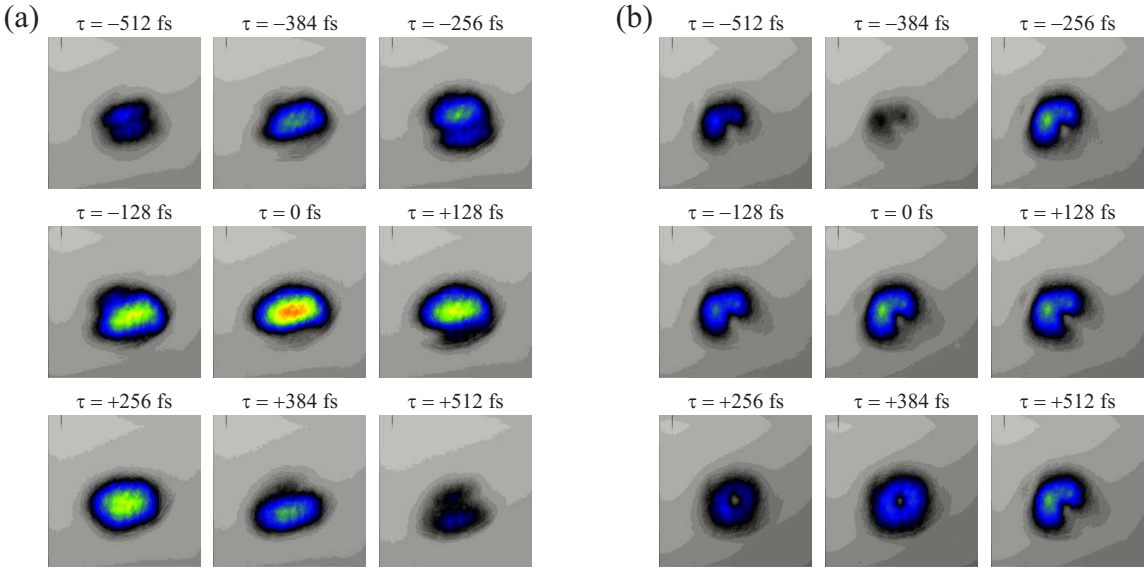

Figure 5.3.6: (a) Measurement of the spatial intensity of the SHG signal of the gated HG pulse following a type II SHG process for delays of the gate between −512 fs and +512 fs. (b) Same as (a) for the gating of the LG pulse.

beam with respect to one another remains.

The spatial intensity of the gated LG-HG interference is depicted in figure 5.3.7 for 21 delays between −640 fs and +640 fs. The results also indicate a slightly longer persisting SHG signal compared to the simulation (see figure 5.3.4). In accordance to the simulation, the intensity distribution takes a bean-like shape, whose alignment also changes with the delay. There seem to be two artifacts, however, for delays of −320 fs and +512 fs. Both do not seem to follow the envelope of the space integrated crosscorrelation, that is expected for this experiment, with the first delay having a too low amplitude, while the second seems to be too intense. The latter is even comparable to the beamprofile at time zero. Apart from these artifacts, the overall dynamics in the measurement do not fully resemble the simulated rotation of the spatial intensity distribution around the beam axis. There might be some signals remaining that superimpose with the desired three-field signal, contributions of only one field can be excluded, as they were practically zero, but the gate produced some noticeable two-field signals with the HG and LG pulses. Calculating the center of mass for the measured data could give some insight into the dynamics of the data, as well as elaborate on the beam stability issue. The centers of mass of the SHG beamprofiles for all delays of the gated HG pulse, LG pulse, and HG-LG interference are plotted in figure 5.3.8a, b, and c, respectively. The centers of mass for all datasets are located on a 20 × 20 pixel section of the CCD camera. For the HG pulse a seemingly random motion of the center of mass is observed, while the LG signal seems to move preferably in the horizontal and less in the vertical direction. The center of mass of the HG-LG interference does move horizontally and vertically roughly by the same amount and remotely follows a circular behavior, however no clear indication of the spiraling motion, that is expected from simulation in figure 5.3.5b, can be observed. The fact that the HG signal does move approximately the same amount in vertical and horizontal direction as the HG-LG interference suggests that beam pointing is an issue, that might prevent a clear determination of the rotation dynamics in the recorded data altogether.

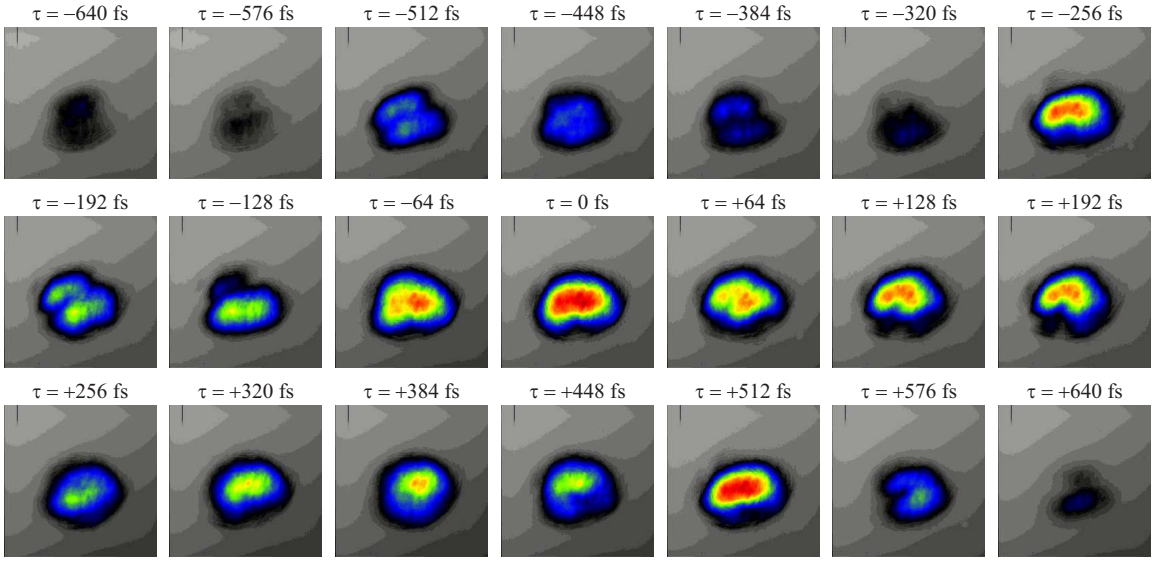

Figure 5.3.7: Measurement of the spatially resolved SHG intensity of the HG-LG interference for 21 different gate delays in the interval between −640 fs to +640 fs.

A mechanical perturbation of the setup by the shutter of the camera was excluded by placing the camera of a separate table next to the laser table. Also the air conditioning in the lab itself and the neighboring labs along with all expendable chillers were shut down during the measurement to ensure no disruption from nearby mechanical motions arise. In addition the measurements presented were taken over night at a weekend, which led to slight improvements compared to data recorded on weekday afternoons, so disturbances should have been reduced to the minimum. However, one source of perturbation remained in the lab, namely the experimenter. All measurements presented in this section were taken in the same session parallel to each other, which required blocking the beam paths of certain arms of the interferometer-like setup manually, since no mechanical shutters were installed. The experimenter, however, is not the lone source of the beam pointing on the camera, this was checked by a test measurement controlled via remote excess to the

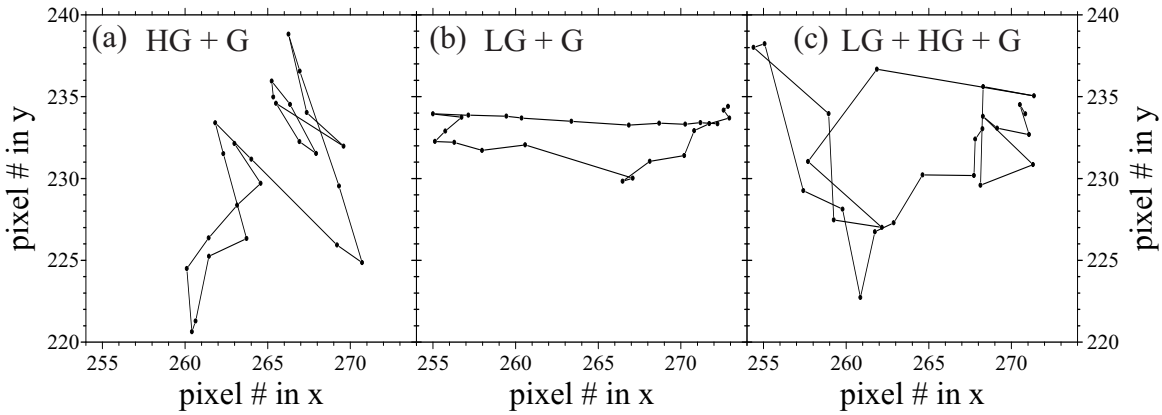

Figure 5.3.8: Coordinates of the center of mass for each delay (dots), the connecting lines indicate the previous and subsequent delay. For gated signal of the (a) HG pulse, (b) LG pulse, and (c) the LG-HG interference.

controls of the experiment. Despite all these sources of error the center of mass of the LG-HG interference signal in figure 5.3.8c does move on a course that somewhat resembles a circle. This may indicate the rotation movement derived in the simulations. However, at this point the identification of the observed motion of the center of mass as the calculated motion of the interference is at best only qualitative. Interferometric stability is crucial and was not sufficient for a more pronounced demonstration of the spiraling motion.

CHAPTER 6

SUMMARY AND OUTLOOK

This thesis focused on the application of ultrafast time-resolved techniques using femtosecond laser pulses to light-matter interaction and the generation of fs pulses bearing orbital angular momentum (OAM). In the first part of the presented work the interaction of light with matter was exploited to shed new light on the photo-dynamics of phenyl-benzo[c]tetrazolo-cinnolium chloride (PTC), that is one of the few known tetrazolium salts that displays fluorescence. The first step involves a photo-reaction to form PTC from the precursor 2,3,5-triphenyl-tetrazolium chloride (TTC) after irradiation with UV light. The fs light pulses can be used to excite PTC, the dynamics afterward can then be monitored using sophisticated experimental techniques. These molecular processes are unique for every compound, but have certain systematic for one class of molecules. Therefore, learning about the excited state dynamics of one tetrazolium salt could help understanding the observations of another closely related compound. The techniques applied in this thesis focused on monitoring the fluorescence decay in time. These emission processes usually take place on time scales between several hundred femtoseconds to several nanoseconds, whereas phosphorescence can even take up to several microseconds. The slow contributions to the fluorescence were investigated using TCSPC and the faster dynamics using femtosecond fluorescence upconversion. The second part investigated the properties of light fields with non-planar wavefronts, namely fs Laguerre-Gaussian pulses. These modes have helical wave fronts, due to a helical spatial phase, and a doughnut shaped spatial intensity distribution. Visualization of the spatial phase is desirable, however not easily achievable. For example the interference of a Laguerre-Gaussian (LG) and Hermite-Gaussian (HG) pulse, that are chirped oppositely to each other, does rotate in space on the time scale of the chirped pulses. In this thesis, LG pulses were investigated with respect to their temporal and spatial properties and an approach to measure the rotation of the interference was explored, that utilizes a type II SHG process with a gate pulse.

The results of the performed PTC studies are presented in chapter 4. After the steady-state spectroscopic characteristics of PTC and the related compounds TTC and benco-[c]-cinnoline (BCC) were investigated, it became clear that PTC has only one fluorescent state. The fluorescence quantum yield was determined in the alcoholic solvents methanol,

ethanol, and ethylene glycol suggesting a dependence of either the viscosity or polarity of the solvent. Time-resolved spectroscopy on the picosecond time scale revealed fluorescence lifetimes that depend on the solvation environment of the chromophore. Whereas a long nanosecond time constant is present, but neglectably low in amplitude in methanol and ethanol, a second main emission constant was determined, that is attributed to the main fluorescence of PTC. The amplitude of the nanosecond time constant not only increases in the more viscous solvents ethylene glycol and glycerol, also a third contribution arises, which is very fast on the time scale of the instrument and is attributed to solvation effects. It was found that the main emission time constant does increase with the solvent viscosity. However, a correlation of the radiative and non-radiative rate with solvent parameters revealed an independence of the emissive relaxation path on the viscosity and the polarity, whereas the non-radiative relaxation is polarity dependent. Further studies of PTC using fs fluorescence upconversion offered an insight into the biphasic solvation dynamics, that describe the complex relaxation dynamics of the system between excitation and emission. This study also revealed an excitation energy independence of the main fluorescence lifetime, whereas the duration of the relaxation prior to the luminescence increase to account for the additional relaxation of the higher lying electronic state. The conducted experiments led to a conceivable photoreaction scheme that involves one relaxed excited state to which every excited states eventually relaxes. This luminescent state can either relax radiatively or non-radiatively. At this point it is not clear whether the latter has an intermediate transition state or not. Furthermore, the strong solvent dependency of the non-radiative rate suggests that a transition radical might also be conceivable, which, however, had not yet been reported in literature. The findings could help in understanding the photodynamics of other fluorescent tetrazolium compounds. Although fluorescent formazans are highly interesting for cytotoxicity assays [136], since they offer the possibility to add microscopy and flow cytometry techniques to the assay, a fluorescent tetrazolium salt would offer the complementary advantage of being able to monitor the different metabolic activities within different locations of the cell. Prior to any such application an understanding of the photodynamics of the fluorescent tetrazolium has to be established, the groundwork of which had partly been laid out in chapter 4.

The properties of Laguerre-Gaussian laser beams have been subject of investigation since their discovery. The studies presented in chapter 5 corroborate further into these laser modes with their unique helical wavefronts. First, the spatial intensity distributions of a LG and a HG pulse were investigated and compared quantitatively. The mode conversion via a spiral phase plate (SPP) displayed a beamprofile with a doughnut shaped spatial intensity distribution with no amplitude on the propagation axis of the beam. Furthermore, temporal characterization showed that the conversion into a LG mode does not alter the temporal shape of the used pulse. The non-collinear interference of a LG with a HG beam was used to determine the orbital angular momentum (OAM) of the beam, that describes the amount of 2π changes that the spatial phase performs for one revolution around the beam axis. It was found that the SPP produces exclusively the LG_{01} mode. After frequency doubling it has been shown that OAM of the SHG is doubled due to momentum conservation. Both pulses were then chirped inversely to each other and characterized for their temporal shape. Changing the spectral phase of an LG does not alter the spatial intensity distribution of the pulse, as was shown with three non-zero spectral phases. Also the same characterization techniques as for HG pulses were deployed

and no considerable difference was noted in terms quality and reliability of the results. The main goal of this project was the investigation of the temporal evolution of the interference of a LG pulse with a HG pulse, when both are inversely chirped. These dynamics were first explored theoretically via calculations of the expected behavior. On the one hand it was found that, if both pulses have the same sign in their respective quadratic spectral phase term, no dynamics in the spatial interference of both is expected. On the other hand, if both pulses are inversely chirped the spatial intensity distribution does move in a spiraling motion around the beam axis on the timescales of the pulses. This ultrafast intensity motion cannot be observed by any electronic device, as it is too fast. However, the simulation revealed that a type II SHG process, in which the LG-HG interference is gated by a third bandwidth limited pulse, should result in a signal that is experimentally attainable and displays the intensity distribution motion around the beam axis. It was found from the calculation that the spiraling motion is slow at time zero of the interference and does increase in angular velocity towards later and earlier times, thus the rotation does change direction at time zero. The experimental setup, that was designed, build up, and characterized to measure this rotation, however, only reproduced the calculations to a very limited extent. Measurements on the type II SHG signal of the LG and HG pulses alone with the gate pulse revealed a potential obstacle that could hinder the measurement of the rotation. Nevertheless, the LG-HG interference was also measured in a gated type II SHG process, however no rotation was observed from the beamprofiles. Also the center of mass of the images for each delay, that were used in the simulation to characterize the rotation motion, did not show a satisfying spiraling behavior. Although it should be noted that the LG-HG interference displayed a jittery circular motion, however it cannot be stated with certainty that this is due to the predicted behavior or to the beam pointing, that had been observed for the gated LG and HG SHG. At this point the experiment lags behind the simulation, a point of improvement would definitely be the use of some kind of beam stabilization unit to increase the interferometric stability. Efforts had been made to increase the stability, however the experiments results indicate that the interferometric stability of the setup was not sufficient. The beam profile behind the $4f$-pulseshaper remained an issue until the end, only minimizing the ellipticity was feasible. However, these laser modes are interesting and not fully explored yet, especially applications in quantum communication [145–149] and cryptography [38–40] are on the horizon and applications in microscopy see a lot of attention recently in literature [33]. Considering these advances a deeper understanding of fs Laguerre and Bessel beams are necessary to unlock the full potential of technologies involving these classes of laser modes.

List of Abbreviations

- **2D** - two-dimensional
- **AC** - autocorrelation
- **ADC** - analog-to-digital converter
- **a.u.** - arbitrary unit
- **BBO** β-barium borate
- **BCC** - benco[c]cinnoline
- **BP** - Brewster prism
- **BRF** - birefringent filter
- **BS** - beamsplitter
- **CCD** - charge coupled device
- **DFG** - difference frequency generation
- **e.g.** - exempli gratia
- **FROG** - frequency resolved optical gating
- **fs** - femtosecond
- **FWHM** - full width at half maximum
- **GRENOUILLE** - Grating-eliminated no-nonsense observation of ultrafast incident laser light e-fields
- **HG** - Hermite-Gaussian
- **HWP** - halfwave plate
- **IC** - internal conversion
- **i.e.** - id est
- **IR** - infrared
- **IRF** - instrument response function
- **ISC**- intersystem crossing
- **ITO** - indium tin oxide
- **IVR** - intramolecular vibrational redistribution
- **laser** - light amplification by stimulated emission of radiation

- **LC** - liquid crystal
- **LD** - laser diode
- **LED** - light emitting diode
- **LG** - Laguerre-Gaussian
- **ND** - neutral density
- **NIR** - near infrared
- **OAM** - orbital angular momentum
- **PMT** - photo multiplier tube
- **ps** - picosecond
- **PTC** - phenyl-benzo-[c]-tetrazolo-cinnolium chloride
- **SFG** - sum frequency generation
- **SHG** - second harmonic generation
- **SLM** - spatial light modulator
- **SPP** - spiral phase plate
- **STC** - space-time coupling
- **STED** - stimulated emission depletion
- **TA** - transient absorption
- **TAC** - time-to-amplitude converter
- **TCSPC** - time correlated single photon counting
- **THG** - third harmonic generation
- **Ti:sapphire** - titanium-doped aluminium oxide (Al_2O_3)
- **TOD** - third order dispersion
- **TPF** - 1,3,5-triphenyiltetrazium formazan
- **TTC** - 2,3,5-triphenyltetrazolium chloride
- **UV** - ultraviolet
- **VC** - vibrational cooling
- **ZDC** - zero dispersion compressor

BIBLIOGRAPHY

[1] T. Bolze, J.-L. Wree, F. Kanal, D. Schleier, and P. Nuernberger, *Ultrafast dynamics of a fluorescent tetrazolium compound in solution*, ChemPhysChem **19**, 138–147 (2018).

[2] J. Hecht, *Short history of laser development*, Opt. Eng. **49**, 49–23 (2010).

[3] D. J. Tannor and S. A. Rice, *Control of selectivity of chemical reaction via control of wave packet evolution*, J. Chem. Phys. **83**, 5013–5018 (1985).

[4] P. Brumer and M. Shapiro, *Control of unimolecular reactions using coherent light*, Chem. Phys. Lett. **126**, 541 – 546 (1986).

[5] A. P. Peirce, M. A. Dahleh, and H. Rabitz, *Optimal control of quantum-mechanical systems: Existence, numerical approximation, and applications*, Phys. Rev. A **37**, 4950–4964 (1988).

[6] R. Unanyan, M. Fleischhauer, B. Shore, and K. Bergmann, *Robust creation and phase-sensitive probing of superposition states via stimulated raman adiabatic passage (stirap) with degenerate dark states*, Opt. Commun. **155**, 144 – 154 (1998).

[7] A. Assion, T. Baumert, M. Bergt, T. Brixner, B. Kiefer, V. Seyfried, M. Strehle, and G. Gerber, *Control of chemical reactions by feedback-optimized phase-shaped femtosecond laser pulses*, Science **282**, 919–922 (1998).

[8] Y. J. Yan and S. Mukamel, *Femtosecond pump-probe spectroscopy of polyatomic molecules in condensed phases*, Phys. Rev. A **41**, 6485–6504 (1990).

[9] W. T. Pollard, S. Lee, and R. A. Mathies, *Wave packet theory of dynamic absorption spectra in femtosecond pump–probe experiments*, J. Chem. Phys. **92**, 4012–4029 (1990).

[10] H. Umeda, M. Takagi, S. Yamada, S. Koseki, and Y. Fujimura, *Quantum control of molecular chirality: Optical isomerization of difluorobenzo[c]phenanthrene*, J. Am. Chem. Soc. **124**, 9265–9271 (2002).

[11] G. Vogt, G. Krampert, P. Niklaus, P. Nuernberger, and G. Gerber, *Optimal control of photoisomerization*, Phys. Rev. Lett. **94**, 068305 (2005).

[12] P. Nuernberger, G. Vogt, T. Brixner, and G. Gerber, *Femtosecond quantum control of molecular dynamics in the condensed phase*, Phys. Chem. Chem. Phys. **9**, 2470–2497 (2007).

[13] T. Kumpulainen, B. Lang, A. Rosspeintner, and E. Vauthey, *Ultrafast elementary photochemical processes of organic molecules in liquid solution*, Chem. Rev. **117**, 10826–10939 (2017).

[14] J. Knorr, P. Sokkar, S. Schott, P. Costa, W. Thiel, W. Sander, E. Sanchez-Garcia, and P. Nuernberger, *Competitive solvent-molecule interactions govern primary processes of diphenylcarbene in solvent mixtures*, Nat. Commun. 12968 (2016).

[15] A. J. Orr-Ewing, *Taking the plunge: chemical reaction dynamics in liquids*, Chem. Soc. Rev. (2017), doi:10.1039/c7cs00331e.

[16] H. v. Pechmann and P. Runge, *Oxydation der Formazylverbindungen. II. Mittheilung*, Ber. Dtsch. Chem. Ges. **27**, 2920–2930 (1894).

[17] G. Lakon, *The topographical tetrazolium method for determining the germinating capacity of seeds*, Plant Physiol. **24**, 389–394 (1949).

[18] R. P. Moore, *Tetrazolium seed testing developments in North America*, J. Seed Technol. **1**, 17–30 (1976).

[19] T. Mosmann, *Rapid colorimetric assay for cellular growth and survival: Application to proliferation and cytotoxicity assays*, J. Immunol. Methods **65**, 55–63 (1983).

[20] M. V. Berridge, P. M. Herst, and A. S. Tan, *Tetrazolium dyes as tools in cell biology: New insights into their cellular reduction*, Biotechnol. Annu. Rev. **11**, 127–152 (2005).

[21] J. Carmichael, W. G. DeGraff, A. F. Gazdar, J. D. Minna, and J. B. Mitchell, *Evaluation of a tetrazolium-based semiautomated colorimetric assay: Assessment of chemosensitivity testing*, Cancer Res. **47**, 936–942 (1987).

[22] M. C. Alley, D. A. Scudiero, A. Monks, M. L. Hursey, M. J. Czerwinski, D. L. Fine, B. J. Abbott, J. G. Mayo, R. H. Shoemaker, and M. R. Boyd, *Feasibility of drug screening with panels of human tumor cell lines using a microculture tetrazolium assay*, Cancer Res. **48**, 589–601 (1988).

[23] C. Pannecouque, D. Daelemans, and E. D. Clercq, *Tetrazolium-based colorimetric assay for the detection of hiv replication inhibitors: revisited 20 years later*, Nat. Prot. **3**, 427–434 (2008).

[24] C.-X. Wei, M. Bian, and G.-H. Gong, *Tetrazolium compounds: synthesis and applications in medicine*, Molecules **20**, 5528–5553 (2015).

[25] A. W. Nineham, *The chemistry of formazans and tetrazolium salts*, Chem. Rev. **55**, 355–483 (1955).

[26] N. D. Cheronis and H. Stein, *Tetrazolium salts as chemical reagents*, J. Chem. Edu. **33**, 120 (1956).

[27] D. D. Zorn, J. A. Boatz, and M. S. Gordon, *Electronic structure studies of tetrazolium-based ionic liquids*, J. Phys. Chem. B **110**, 11110–11119 (2006).

[28] A. Chowdhury, S. T. Thynell, and P. Lin, *Confined rapid thermolysis/ftir/tof studies of tetrazolium-based energetic ionic liquids*, Thermochim. Acta **485**, 1 – 13 (2009).

[29] S. Ebraheem, A. Abdel-Fattah, F. Said, and Z. Ali, *Polymer-based triphenyl tetrazolium chloride films for ultraviolet radiation monitoring*, Rad. Phys. Chem. **57**, 195 – 202 (2000).

[30] A. Mills, P. Grosshans, and M. McFarlane, *UV dosimeters based on neotetrazolium chloride*, J. Photochem. Photobiol. A **201**, 136–141 (2009).

[31] I. Hausser, D. Jerchel, and R. Kuhn, *Ein blau fluorescierendes Bestrahlungsprodukt von Triphenyl-tetrazolium-chlorid*, Chem. Ber. **82**, 195–199 (1949).

[32] K. I. Willig, S. O. Rizzoli, V. Westphal, R. Jahn, and S. W. Hell, *STED microscopy reveals that synaptotagmin remains clustered after synaptic vesicle exocytosis*, Nature **440**, 935–939 (2006).

[33] F. Balzarotti, Y. Eilers, K. C. Gwosch, A. H. Gynnå, V. Westphal, F. D. Stefani, J. Elf, and S. W. Hell, *Nanometer resolution imaging and tracking of fluorescent molecules with minimal photon fluxes*, Science **355**, 606–612 (2017).

[34] L. Allen, M. W. Beijersbergen, R. J. C. Spreeuw, and J. P. Woerdman, *Orbital angular momentum of light and the transformation of laguerre-gaussian laser modes*, Phys. Rev. A **45**, 8185–8189 (1992).

[35] C. Paterson, *Atmospheric turbulence and orbital angular momentum of single photons for optical communication*, Phys. Rev. Lett. **94**, 153901 (2005).

[36] J. Wang, J.-Y. Yang, I. M. Fazal, N. Ahmed, Y. Yan, H. Huang, Y. Ren, Y. Yue, S. Dolinar, M. Tur, and A. E. Willner, *Terabit free-space data transmission employing orbital angular momentum multiplexing*, Nat. Photonics **6** (2012).

[37] N. Bozinovic, Y. Yue, Y. Ren, M. Tur, P. Kristensen, H. Huang, A. E. Willner, and S. Ramachandran, *Terabit-Scale Orbital Angular Momentum Mode Division Multiplexing in Fibers*, Science **340**, 1545 (2013).

[38] S. Gröblacher, T. Jennewein, A. Vaziri, G. Weihs, and A. Zeilinger, *Experimental quantum cryptography with qutrits*, New J. Phys. **8**, 75 (2006).

[39] J. Leach, B. Jack, J. Romero, A. K. Jha, A. M. Yao, S. Franke-Arnold, D. G. Ireland, R. W. Boyd, S. M. Barnett, and M. J. Padgett, *Quantum correlations in optical angle–orbital angular momentum variables*, Science **329**, 662–665 (2010).

[40] M. Mafu, A. Dudley, S. Goyal, D. Giovannini, M. McLaren, M. J. Padgett, T. Konrad, F. Petruccione, N. Lütkenhaus, and A. Forbes, *Higher-dimensional orbital-angular-momentum-based quantum key distribution with mutually unbiased bases*, Phys. Rev. A **88**, 032305 (2013).

[41] J. C. Maxwell, *On physical lines of force*, Philosophical Magazine **XXI**, 161–175 (1861).

[42] J. C. Maxwell, *A dynamical theory of the electromagnetic field*, Philos. Trans. Roy. Soc. London **155**, 459–512 (1865).

[43] P. W. Milonni and J. H. Eberly, *Lasers*, Wiley, New York, NY (USA) (1988).

[44] L. E. Kinsler, A. R. Frey, A. B. Coppens, and J. V. Sanders, *Fundamentals of Acoustics*, Wiley, New York, NY (USA) (1999).

[45] R. H. Randall, *An Introduction to Acoustics*, Dover Publications, Mineola, NY (USA) (2005).

[46] D. J. Jones, S. A. Diddams, J. K. Ranka, A. Stentz, R. S. Windeler, J. L. Hall, and S. T. Cundiff, *Carrier-envelope phase control of femtosecond mode-locked lasers and direct optical frequency synthesis*, Science **288**, 635–639 (2000).

[47] F. Träger, *Springer Handbook of Lasers and Optics*, Springer, New York, NY (USA) (2007).

[48] C. G. Durfee, A. R. Rundquist, S. Backus, C. Herne, M. M. Murnane, and H. C. Kapteyn, *Phase matching of high-order harmonics in hollow waveguides*, Phys. Rev. Lett. **83**, 2187–2190 (1999).

[49] P. Dietrich, F. Krausz, and P. B. Corkum, *Determining the absolute carrier phase of a few-cycle laser pulse*, Opt. Lett. **25**, 16–18 (2000).

[50] A. M. Weiner, *Ultrafast Optics*, Wiley, Hoboken, NJ (USA) (2009).

[51] J.-C. Diels and W. Rudolf, *Ultrashort Laser Pulses Phenomena*, Elsevier, Amsterdam (NL) (2006).

[52] SCHOTT AG, *Optical Glass - Collection Datasheets*, Homepage: http://www.us.schott.com/advanced_optics/english/products/optical-materials/optical-glass/optical-glass/index.html (2017).

[53] E. Hecht, *Optik*, Addison-Wesley, Bonn (GER) (1994).

[54] A. M. Weiner, J. P. Heritage, and E. M. Kirschner, *High-resolution femtosecond pulse shaping*, J. Opt. Soc. Am. B **5**, 1563–1572 (1988).

[55] A. M. Weiner, D. E. Leaird, J. S. Patel, and J. R. Wullert, *Programmable femtosecond pulse shaping by use of a multielement liquid-crystal phase modulator*, Opt. Lett. **15**, 326–328 (1990).

[56] A. M. Weiner, D. E. Leaird, J. S. Patel, and J. R. Wullert, *Programmable shaping of femtosecond optical pulses by use of 128-element liquid crystal phase modulator*, IEEE J. Quantum Electron. **28**, 908–920 (1992).

[57] A. M. Weiner, *Ultrafast optical pulse shaping: A tutorial review*, Opt. Commun. **284**, 3669 – 3692 (2011).

[58] O. Masihzadeh, P. Schlup, and R. A. Bartels, *Complete polarization state control of ultrafast laser pulses with a single linear spatial light modulator*, Opt. Express **15**, 18025–18032 (2007).

[59] M. Ninck, A. Galler, T. Feurer, and T. Brixner, *Programmable common-path vector field synthesizer for femtosecond pulses*, Opt. Lett. **32**, 3379–3381 (2007).

[60] T. Brixner and G. Gerber, *Femtosecond polarization pulse shaping*, Opt. Lett. **26**, 557–559 (2001).

[61] M. M. Wefers and K. A. Nelson, *Generation of high-fidelity programmable ultrafast optical waveforms*, Opt. Lett. **20**, 1047–1049 (1995).

[62] M. M. Wefers and K. A. Nelson, *Analysis of programmable ultrashort waveform generation using liquid-crystal spatial light modulators*, J. Opt. Soc. Am. B **12**, 1343–1362 (1995).

[63] F. Weise and A. Lindinger, *Full control over the electric field using four liquid crystal arrays*, Opt. Lett. **34**, 1258–1260 (2009).

[64] S. Hassani, *Classical Orthogonal Polynomials*, 241–263, Springer International Publishing, Cham (2013).

[65] J. J. Foncannon, *Classical and quantum orthogonal polynomials in one variable*, Math. Intelligencer **30**, 54–60 (2008).

[66] D. J. Tannor, *Introduction to quantum Mechanics – A Time-Dependent Perspective*, University Science Books, Sausalito, CA (USA) (2007).

[67] H. Haken and H. C. Wolf, *Molekülphysik und Quantenchemie*, Springer, Berlin (GER) (2005).

[68] G. C. Schatz and M. A. Ratner, *Quantum Mechanics in Chemistry*, Dover Publications, Mineola, NY (USA) (2002).

[69] M. L. Horng, J. A. Gardecki, A. Papazyan, and M. Maroncelli, *Subpicosecond measurements of polar solvation dynamics: Coumarin 153 revisited*, J. Phys. Chem. **99**, 17311–37 (1995).

[70] A. A. Lamola and G. S. Hammond, *Mechanisms of photochemical reactions in solution. XXXIII. intersystem crossing efficiencies*, J. Chem. Phys. **43**, 2129–2135 (1965).

[71] C. C. Lo and B. Leskovar, *Performance studies of high gain photomultiplier having z–configuration of microchannel plates*, IEEE Trans. Nucl. Sci. **28**, 698–704 (1981).

[72] M. Ito, H. Kume, and K. Oba, *Computer analysis of the timing properties in micro channel plate photomultiplier tubes*, IEEE Trans. Nucl. Sci. **31**, 408–412 (1984).

[73] I. Yamazaki, N. Tamai, H. Kume, H. Tsuchiya, and K. Oba, *Microchannel–plate photomultiplier applicability to the time–correlated photon–counting method*, Rev. Sci. Instrum. **56**, 1187–1194 (1985).

[74] J. R. Lakowicz, *Principles of Fluorescence Spectroscopy*, Springer, New York, NY (USA) (2010).

[75] G. Fleming, *Chemical applications of ultrafast spectroscopy*, Oxford University Press, Incorporated, Oxford (UK) (1986).

[76] B. Jámbor, *Tetrazoliumsalze in der Biologie*, VEB Gustav Fischer, Jena (1960, and references therein).

[77] N. Greenham, I. Samuel, G. Hayes, R. Phillips, Y. Kessener, S. Moratti, A. Holmes, and R. Friend, *Measurement of absolute photoluminescence quantum efficiencies in conjugated polymers*, Chem. Phys. Lett. **241**, 89 – 96 (1995).

[78] C. Würth, M. G. González, R. Niessner, U. Panne, C. Haisch, and U. R. Genger, *Determination of the absolute fluorescence quantum yield of rhodamine 6G with optical and photoacoustic methods – providing the basis for fluorescence quantum yield standards*, Talanta **90**, 30 – 37 (2012).

[79] C. V. Bindhu, S. S. Harilal, G. K. Varier, R. C. Issac, and V. P. N. N. C. P. G. Vallabhan, *Measurement of the absolute fluorescence quantum yield of rhodamine b solution using a dual-beam thermal lens technique*, J. Phys. D **29**, 1074 (1996).

[80] M. J. Adams, J. G. Highfield, and G. F. Kirkbright, *Determination of the absolute quantum efficiency of luminescence of solid materials employing photoacoustic spectroscopy*, Anal. Chem. **52**, 1260–64 (1980).

[81] T. R. Williams, Alun, S. A. Winfield, and J. N. Miller, *Relative fluorescence quantum yields using a computer-controlled luminescence spectrometer*, Analyst **108**, 1067–71 (1983).

[82] G. A. Crosby and J. N. Demas, *Measurement of photoluminescence quantum yields. review*, J. Phys. Chem. **75**, 991–1024 (1971).

[83] A. Pardo, D. Reyman, J. M. L. Poyato, and F. Medina, *Some β-carboline derivatives as fluorescence standards*, J. Lumin. **51**, 269–74 (1992).

[84] W. H. Melhuish, *Quantum efficiencies of fluorescence of organic substances: Effect of solvent and concentration of the fluorescent solute*, J. Phys. Chem. **65**, 229–3 (1961).

[85] S. D'Souza, E. Antunes, C. Litwinski, and T. Nyokong, *Photophysical behavior of zinc monoaminophthalocyanines linked to mercaptopropionic acid-capped cdte quantum dots*, J. Photochem. Photobiol. **220**, 11 – 19 (2011).

[86] A. Martinez-Peragon, D. Miguel, A. Orte, A. J. Mota, M. J. Ruedas-Rama, J. Justicia, J. M. Alvarez-Pez, J. M. Cuerva, and L. Crovetto, *Rational design of a new fluorescent 'on/off' xanthene dye for phosphate detection in live cells*, Org. Biomol. Chem. **12**, 6432–6439 (2014).

[87] H. E. Lessing and A. Von Jena, *Separation of Rotational Diffusion and Level Kinetics in Transient Absorption Spectroscopy*, Chem. Phys. Lett. **42**, 213–217 (1976).

[88] S. Schott, A. Steinbacher, J. Buback, P. Nuernberger, and T. Brixner, *Generalized magic angle for time-resolved spectroscopy with laser pulses of arbitrary ellipticity*, J. Phys. B: At. Mol. Opt. Phys. **47**, 124014 (2014).

[89] R. Luchowski, Z. Gryczynski, P. Sarkar, J. Borejdo, M. Szabelski, P. Kapusta, and I. Gryczynski, *Instrument response standard in time-resolved fluorescence*, Rev. Sci. Instrum. **80**, 033109 (2009).

[90] L. Grimmelsmann, A. Marefat Khah, C. Spies, C. Hättig, and P. Nuernberger, *Ultrafast dynamics of a triazene: Excited-state pathways and the impact of binding to the minor groove of dna and further biomolecular systems*, J. Phys. Chem. Lett. **8**, 1986–1992 (2017).

[91] C. Inc., *Operator's Manual: The Coherent Mira Model 900-B Laser*, COHERENT Inc., Santa Clara (CA) (1993).

[92] J.-C. M. Diels, J. J. Fontaine, I. C. McMichael, and F. Simoni, *Control and measurement of ultrashort pulse shapes (in amplitude and phase) with femtosecond accuracy*, Appl. Opt. **24**, 1270–1282 (1985).

[93] D. J. Kane and R. Trebino, *Characterization of arbitrary femtosecond pulses using frequency-resolved optical gating*, IEEE J. Quantum Electron. **29**, 571–579 (1993).

[94] R. Barakat and G. Newsam, *Necessary conditions for a unique solution to two–dimensional phase recovery*, J. Math. Phys. **25**, 3190–3193 (1984).

[95] J. R. Fienup, *Reconstruction of a complex-valued object from the modulus of its fourier transform using a support constraint*, J. Opt. Soc. Am. A **4**, 118–123 (1987).

[96] H. Stark, *Image Recovery: Theory and Application*, Elsevier, Amsterdam (NL) (1987).

[97] D. J. Kane and R. Trebino, *Single-shot measurement of the intensity and phase of an arbitrary ultrashort pulse by using frequency-resolved optical gating*, Opt. Lett. **18**, 823–825 (1993).

[98] K. W. DeLong and R. Trebino, *Improved ultrashort pulse-retrieval algorithm for frequency-resolved optical gating*, J. Opt. Soc. Am. A **11**, 2429–2437 (1994).

[99] K. W. DeLong, D. N. Fittinghoff, R. Trebino, B. Kohler, and K. Wilson, *Pulse retrieval in frequency-resolved optical gating based on the method of generalized projections*, Opt. Lett. **19**, 2152–2154 (1994).

[100] D. J. Kane, G. Rodriguez, A. J. Taylor, and T. S. Clement, *Simultaneous measurement of two ultrashort laser pulses from a single spectrogram in a single shot*, J. Opt. Soc. Am. B **14**, 935–943 (1997).

[101] P. O'Shea, M. Kimmel, X. Gu, and R. Trebino, *Highly simplified device for ultrashort-pulse measurement*, Opt. Lett. **26**, 932–934 (2001).

[102] N. R. Heckenberg, R. McDuff, C. P. Smith, and A. G. White, *Generation of optical phase singularities by computer-generated holograms*, Opt. Lett. **17**, 221–223 (1992).

[103] M. Beijersbergen, R. Coerwinkel, M. Kristensen, and J. Woerdman, *Helical-wavefront laser beams produced with a spiral phaseplate*, Opt. Commun. **112**, 321 – 327 (1994).

[104] T. Watanabe, M. Fujii, Y. Watanabe, N. Toyama, and Y. Iketaki, *Generation of a doughnut-shaped beam using a spiral phase plate*, Rev. Sci. Instrum. **75**, 5131–5135 (2004).

[105] K. Bezuhanov, A. Dreischuh, G. G. Paulus, M. G. Schätzel, and H. Walther, *Vortices in femtosecond laser fields*, Opt. Lett. **29**, 1942–1944 (2004).

[106] K. Sueda, G. Miyaji, N. Miyanaga, and M. Nakatsuka, *Laguerre-gaussian beam generated with a multilevel spiral phase plate for high intensity laser pulses*, Opt. Express **12**, 3548–3553 (2004).

[107] K. J. Moh, X.-C. Yuan, D. Y. Tang, W. C. Cheong, L. S. Zhang, D. K. Y. Low, X. Peng, H. B. Niu, and Z. Y. Lin, *Generation of femtosecond optical vortices using a single refractive optical element*, Appl. Phys. Lett. **88**, 091103 (2006).

[108] K. Yamane, Y. Toda, and R. Morita, *Ultrashort optical-vortex pulse generation in few-cycle regime*, Opt. Express **20**, 18986–18993 (2012).

[109] M. Bock, J. Jahns, and R. Grunwald, *Few-cycle high-contrast vortex pulses*, Opt. Lett. **37**, 3804–3806 (2012).

[110] Ó. Martínez-Matos, J. A. Rodrigo, M. P. Hernández-Garay, J. G. Izquierdo, R. Weigand, M. L. Calvo, P. Cheben, P. Vaveliuk, and L. Bañares, *Generation of femtosecond paraxial beams with arbitrary spatial distribution*, Opt. Lett. **35**, 652–654 (2010).

[111] A. S. Ostrovsky, C. Rickenstorff-Parrao, and V. Arrizón, *Generation of the perfect optical vortex using a liquid-crystal spatial light modulator*, Opt. Lett. **38**, 534–536 (2013).

[112] O. Martínez-Matos, P. Vaveliuk, J. G. Izquierdo, and V. Loriot, *Femtosecond spatial pulse shaping at the focal plane*, Opt. Express **21**, 25010–25025 (2013).

[113] M. Padgett and L. Allen, *Light with a twist in its tail*, Contemp. Phys. **41**, 275–285 (2000).

[114] S. Franke-Arnold, L. Allen, and M. Padgett, *Advances in optical angular momentum*, Laser Photon. Rev. **2**, 299–313 (2008).

[115] T. Brixner, *Kohärente Kontrolle von Photodissoziationsreaktionen mit optimal geformten ultrakurzen Laserpulsen*, Diplomarbeit, Julius-Maximulians-Universität, Würzburg (GER) (1998).

[116] F. Weygand and I. Frank, *Über die Einwirkung von Licht auf Tetrazolium-Verbindungen: Tetrazolium-Typie. I. Mitt.*, Z. Naturforsch. B **3**, 377–379 (1948).

[117] F. Kanal, D. Schleier, and P. Nuernberger, *Ultrafast photogeneration of a tetrazolinyl radical*, ChemPhysChem **16**, 3143–3146 (2015).

[118] M. Předota, V. Petříček, Z. Žák, T. Głowiak, and J. Novotný, *Structure du perrhenate de triphényl-2,3,5 tétrazolium*, Acta Cryst. C **47**, 738–740 (1991).

[119] M. Gjikaj, T. Xie, and W. Brockner, *Uncommon compounds in antimony pentachloride – ionic liquid systems: synthesis, crystal structure and vibrational spectra of the complexes [TPT][SbCl$_6$] and [Cl-EMIm][SbCl$_6$]*, Z. Anorg. Allg. Chem. **635**, 1036–1040 (2009).

[120] M. Takezaki, N. Hirota, and M. Terazima, *Excited state dynamics of 9,10-diazaphenanthrene studied by the time-resolved transient grating method*, J Phys. Chem. **100**, 10015–10020 (1996).

[121] F. A. Neugebauer, *Substituted 5-t-butyl tetrazolinyl and phototetrazolinyl radicals*, Tetrahedron **26**, 4843 – 4851 (1970).

[122] D. R. Lide, *CRC Handbook of Chemistry and Physics*, CRC Press, Boca Raton, FL, 79 edition (1998).

[123] C. Reichardt and T. Welton, *Solvents and Solvent Effects in Organic Chemistry*, Wiley-VCH, Weinheim, 4 edition (2011).

[124] P. G. Jessop, D. A. Jessop, D. Fu, and L. Phan, *Solvatochromic parameters for solvents of interest in green chemistry*, Green Chem. **14**, 1245–1259 (2012).

[125] O. Braem, T. J. Penfold, A. Cannizzo, and M. Chergui, *A femtosecond fluorescence study of vibrational relaxation and cooling dynamics of uv dyes*, Phys. Chem. Chem. Phys. **14**, 3513–3519 (2012).

[126] D. K. Das, K. Makhal, S. N. Bandyopadhyay, and D. Goswami, *Direct observation of coherent oscillations in solution due to microheterogeneous environment*, Sci. Rep. **4**, 6097 (2014).

[127] R. A. Nome, *Ultrafast dynamics of solvation: The story so far*, J. Braz. Chem. Soc. **21**, 2189–2204 (2010).

[128] P. van der Meulen, H. Zhang, A. M. Jonkman, and M. Glasbeek, *Subpicosecond solvation relaxation of 4-(dicyanomethylene)-2-methyl-6-(p-(dimethylamino)styryl)-4h-pyran in polar liquids*, J. Phys. Chem. **100**, 5367–5373 (1996).

[129] R. Adhikary, P. Mukherjee, T. W. Kee, and J. W. Petrich, *Excited-state intramolecular hydrogen atom transfer and solvation dynamics of the medicinal pigment curcumin*, J. Phys. Chem. B **113**, 5255–5261 (2009).

[130] A. Chakraborty, D. Seth, P. Setua, and N. Sarkar, *Dynamics of solvent and rotational relaxation of glycerol in the nanocavity of reverse micelles*, J. Phys. Chem. B **110**, 5359–5366 (2006).

[131] H. Kaur, S. Koley, and S. Ghosh, *Probe dependent solvation dynamics study in a microscopically immiscible dimethyl sulfoxide–glycerol binary solvent*, J. Phys. Chem. B **118**, 7577–7585 (2014).

[132] R. Kuhn and D. Jerchel, *Kristallisiertes 2,3-diphenylen-5-phenyl-tetrazolium-radikal*, Liebigs Ann. Chem. **578**, 1–5 (1952).

[133] D. Jerchel and H. Fischer, *2,3-Diphenylen-tetrazoliumsalze und daraus entstehende Radikale*, Liebigs Ann. Chem. **590**, 216–231 (1954).

[134] F. Dörr, G. Hohlneicher, and S. Schneider, *Die Elektronenspektren 2,2'-verknüpfter Diphenyle; Polarisationsgradspektren und Modellrechnungen. Teil I: Phenanthren, 9,10-Diazaphenanthren-Base und -Kation*, Ber. Bunsenges. Phys. Chem. **70**, 803–817 (1966).

[135] E. Seidler, *The tetrazolium-formazan system: Design and histochemistry*, Prog. Histochem. Cytochem. **24**, 1–79 (1991).

[136] M. K. Ladyman, J. G. Walton, A. Lilienkampf, and M. Bradley, *Fluorescent formazans and tetrazolium salts – towards fluorescent cytotoxicity assays*, Comb. Chem. High Throughput Screen. **19**, 384–391 (2016).

[137] E. Rueda, D. Muñetón, J. A. Gómez, and A. Lencina, *High-quality optical vortex-beam generation by using a multilevel vortex-producing lens*, Opt. Lett. **38**, 3941–3944 (2013).

[138] J. Köhler, M. Wollenhaupt, T. Bayer, C. Sarpe, and T. Baumert, *Zeptosecond precision pulse shaping*, Opt. Express **19**, 11638–11653 (2011).

[139] G. Vogt, P. Nuernberger, R. Selle, F. Dimler, T. Brixner, and G. Gerber, *Analysis of femtosecond quantum control mechanisms with colored double pulses*, Phys. Rev. A **74**, 033413 (2006).

[140] M. Renard, R. Chaux, B. Lavorel, and O. Faucher, *Pulse trains produced by phase-modulation of ultrashort optical pulses: tailoring and characterization*, Opt. Express **12**, 473–482 (2004).

[141] M. M. Wefers and K. A. Nelson, *Space-time profiles of shaped ultrafast optical waveforms*, IEEE J. Quantum Electron. **32**, 161–172 (1996).

[142] B. J. Sussman, R. Lausten, and A. Stolow, *Focusing of light following a 4-f pulse shaper: Considerations for quantum control*, Phys. Rev. A **77**, 043416 (2008).

[143] F. Frei, A. Galler, and T. Feurer, *Space-time coupling in femtosecond pulse shaping and its effects on coherent control*, J. Chem. Phys. **130**, 034302 (2009).

[144] P. Nürnberger, *Adaptive Control of Quantum Systems with Femtosecond Laser Pulses*, Dissertation, Julius-Maximulians-Universität, Würzburg (BY) (2007).

[145] A. Vaziri, G. Weihs, and A. Zeilinger, *Superpositions of the orbital angular momentum for applications in quantum experiments*, J. Opt. B **4**, S47 (2002).

[146] G. Gibson, J. Courtial, M. J. Padgett, M. Vasnetsov, V. Pas'ko, S. M. Barnett, and S. Franke-Arnold, *Free-space information transfer using light beams carrying orbital angular momentum*, Opt. Express **12**, 5448–5456 (2004).

[147] G. Molina-Terriza, J. P. Torres, and L. Torner, *Twisted photons*, Nat. Phys. **3**, 305–310 (2007).

[148] E. Nagali, F. Sciarrino, F. De Martini, L. Marrucci, B. Piccirillo, E. Karimi, and E. Santamato, *Quantum information transfer from spin to orbital angular momentum of photons*, Phys. Rev. Lett. **103**, 013601 (2009).

[149] R. Brüning, B. Ndagano, M. McLaren, S. Schröter, J. Kobelke, M. Duparré, and A. Forbes, *Data transmission with twisted light through a free-space to fiber optical communication link*, J. Opt. **18**, 03LT01 (2016).

PERMISSIONS

Reuse of Reference [1]

Dear Tom Bolze,

We hereby grant permission for the requested use expected that due credit is given to the original source.

If material appears within our work with credit to another source, authorisation from that source must be obtained.

Credit must include the following components:

- Journals: Author(s) Name(s): Title of the Article. Name of the Journal. Publication year. Volume. Page(s).(not yet published) Copyright Wiley-VCH Verlag GmbH & Co. KGaA. Reproduced with permission.

If you also wish to publish your thesis in electronic format, you may use the article according to the Copyright transfer agreement:

3. Final Published Version.

Wiley-VCH hereby licenses back to the Contributor the following rights with respect to the final published version of the Contribution:

a. [...]

b. Re-use in other publications. The right to re-use the final Contribution or parts thereof for any publication authored or edited by the Contributor (excluding journal articles) where such re-used material constitutes less than half of the total material in such publication. In such case, any modifications should be accurately noted. [This applies to each article, not the three articles in total].

Kind regards

Heike Weller
Rights Manager
Rights & Licenses

Wiley-VCH Verlag GmbH & Co. KGaA
Boschstraße 12
69469 Weinheim
Germany
www.wiley-vch.de
T +(49) 6201 606-585
F +(49) 6201 606-332
rightsDE@wiley.com

ACKNOWLEDGEMENTS

The dissertation at hand was partly conducted at the Institute for Physical and Theoretical Chemistry at the university of Würzburg and partly at the Institute for Chemistry and Biochemistry in Bochum. Many people have contributed over past five years to the success of this work. At this point, I would like to express my gratitude to:

- **Prof. Dr. Patrick Nürnberger** for supervising my dissertation and giving me the opportunity to work in this interesting and exciting field of science. Whenever I needed guidance, help, or motivation he never hesitated to share his vast knowledge and inspiring enthusiasm. The friendly and cooperative working atmosphere he created in both laboratories I worked together with him were beneficial for all members or the group. I am also thankful for the trust I was met with in the quest of moving from Würzburg to Bochum and building up the new lab. Thank you very much!

- **Prof. Dr. Tobias Brixner**, as the second member of my GSST supervisory board, for his support and advice regarding every question that ever arose. I am thankful for the opportunity to work his laboratory and group for the first part of my PhD project.

- **Prof. Dr. Tobias Hertel** for his support as the third member of my GSST supervisory board.

- **Dr. Christian Spies** for his insight into his chemical view and knowledge about steady-state spectroscopy and TCSPC.

- **Dr Johannes Knorr** for his help in understanding the transient absorption data within the PTC project and the friendly work atmosphere.

- **Dr. Christoph Schwarz** and **Dr. Christian Kramer** for their help and advice regarding the calibration and use of the $4f$-pulseshaper.

- **Dr. Florian Kanal** and **Dominik Schleier** for inspiring the PTC project and contributing their transient absorption data to the publication.

- **Dr. Andreas Steinbacher** for his LabView support and mostly welcomed advice every scientific or personal matter.

- **Jan-Lucas Wree** for his outstanding contributions to the PTC project, with his relentless and independent work ethic he made the project run as smoothly as possible.
- **Lena Grimmelsmann** for her commendable work ethic, friendly and helpful personality, as well as proof reading and fun in the lab.
- **Bastian Geissler** for his support with the TCSPC, for allocating his Matlab script for global data analysis of time resolved spectroscopy data, and for always being a helpful colleague.
- **Kevin Artmann** for his LabView support and help in the project on shaped fs Laguerre-Gaussian pulses.
- And all other colleagues I had the pleasure to work with in my time as a doctoral student in Würzbug and Bochum: **Dr. Christina Consani, Dr. Federico Koch, Dr. Stefan Rützel, Dr. Martin Kullmann, Dr. Philipp Rudolf, Dr. Monika Pawłowska, Dr. Christian Rewitz, Sebastian Schott, Sebastian Götz, Sebastian Röding, Marco Schmid, Simon Draeger, Bernhard Huber, Heiko Hildenbrand, Niklas Gessner** and **Svenja Wortmann**
- **Andrea Gehring** and **Christel Tönnissen** for their help with every organizational and bureaucratic problem.
- **Dr. Ole Riemann** and **Dr. Stephan Schröder-Köhne** for organizing the GSST study program.
- The **Deutsche Forschungsgemeinschaft** for their research support in the framework of the Emmy-Noether program and the Cluster of Excellence RESOLV (EXC1069).
- The **Wilhelm and Else Heraeus-Stiftung** for financial support of various annual DPG spring meetings.

Finally I would like to thank my friends and family for their ongoing support, especially my beloved mother, whose never ending support and trust in my abilities over the past decade made this whole work possible and me who I am now. Thank you!

"If I'm sad, I stop being sad
and be awesome instead."
- Barnie Stinson

Affidavit

I hereby confirm that my thesis entitled

Photodynamics of a fluorescent tetrazolium salt and shaping of femtosecond Laguerre-Gaussian laser modes in time and space

is the result of my own work. I did not receive any help or support from commercial consultants. All sources and / or materials applied are listed and specified in the thesis.

Furthermore, I confirm that this thesis has not yet been submitted as part of another examination process neither in identical nor in similar form.

Bochum, 16. November 2017

Signature

Eidesstattliche Erklärung

Hiermit erkläre ich an Eides statt, die Dissertation

Photodynamik eines fluoreszierenden Tetrazoliumsalzes und Formung von Femtosekunden Laguerre-Gauss Lasermoden in Raum und Zeit

eigenständig, d.h. insbesondere selbständig und ohne Hilfe eines kommerziellen Promotionsberaters, angefertigt und keine anderen als die von mir angegebenen Quellen und Hilfsmittel verwendet zu haben.

Ich erkläre außerdem, dass die Dissertation weder in gleicher noch in ähnlicher Form bereits in einem anderen Prüfungsverfahren vorgelegen hat.

Bochum, 16. November 2017

Unterschrift